University of West Bohemia
Faculty of Applied Sciences

LOW-TEMPERATURE DEPOSITION OF HIGH-PERFORMANCE THERMOCHROMIC VO_2-BASED COATINGS USING PULSED REACTIVE MAGNETRON SPUTTERING

Ing. David Kolenatý

A thesis submitted for the degree of Doctor of Philosophy
in the field of Plasma Physics and Physics of Thin Films

Supervisor: prof. RNDr. Jaroslav Vlček, CSc.
Department of Physics

Pilsen 2018

Západočeská univerzita v Plzni
Fakulta aplikovaných věd

NÍZKOTEPLOTNÍ DEPOZICE VYSOCE FUNKČNÍCH TERMOCHROMICKÝCH POVLAKŮ NA BÁZI VO_2 POUŽITÍM PULZNÍHO REAKTIVNÍHO MAGNETRONOVÉHO NAPRAŠOVÁNÍ

Ing. David Kolenatý

Disertační práce k získání akademického titulu doktor
v oboru Fyzika plazmatu a tenkých vrstev

Školitel: prof. RNDr. Jaroslav Vlček, CSc.
Katedra fyziky

Plzeň 2018

Preface

This thesis is submitted for the degree of Doctor of Philosophy at the University of West Bohemia. The work herein is to the best of my knowledge original, except where references are made to previous works. The thesis is submitted in a form of six scientific publications and one draft of scientific publication.

The research described herein was conducted under the supervision of prof. RNDr. Jaroslav Vlček, CSc. at the Department of Physics and NTIS, European Centre of Excellence, University of West Bohemia, since September 2014. This thesis has been carried out within the framework of the projects SGS−2013−045 (2013−2015): New thin-film materials and plasma deposition systems, SGS−2016−056 (2016−2018): New nanostructured thin-film materials formed by plasma technologies, and GA ČR−17−08944S (2017−2019): Nanostructured coatings synthetized using highly reactive pulsed plasmas.

Pilsen, November 2018 …….…… Ing. David Kolenatý

Acknowledgements

Firstly, I would like to express my special appreciation and thanks to my supervisor prof. RNDr. Jaroslav Vlček, CSc. who has been a tremendous mentor for me. I would like to thank him for conducting and encouraging my research and for allowing me to grow as a research scientist. His advice on both research as well as on my career have been invaluable.

Besides my supervisor, I would like to thank doc. Ing. Jiří Houška, Ph.D., Ing. Jiří Rezek, Ph.D., and Mgr. Tomáš Bárta for frequent help and cooperation on research. My sincere thanks also go to doc. Ing. Pavel Baroch, Ph.D. and doc. Ing. Petr Zeman, Ph.D. for organization, valuable advice and provided information. Many thanks go to people who were providing technical support in laboratories. I am very grateful to all of the colleagues for their feedback, cooperation and, of course, friendship. Discussions of various subject matters related not just to our scientific work were a great asset to me as well.

Contents

I Introduction

1 Thermochromism

Materials exhibiting changes in their optical properties due to some external stimulus are called chromogenic materials. The most common of these are photochromic, thermochromic and electrochromic materials, where the stimuli are irradiation by light (photons), change in temperature, and an applied electric field, respectively. Thus, thermochromism is a temperature-dependent change in the optical properties of the material [1].

2 Semiconductor-to-metal transition

Boer and Verway in 1937 [2] found out existence of transition-metal oxides as insulators or semiconductors despite exhibiting partially filled $3d$ bands. This confirmed the inadequacy of simple band theory due to the neglect of electron repulsion. In the same year, Peierls [3] pointed out that strong Coulombic repulsion between the electrons could be the origin of the insulating behavior. Mott suggested that electrons become localized by the Coulombic repulsion between two $3d$ electrons of opposite spin on the same ion. As the lattice constant becomes smaller, the activation energy required to form a pair of electron and positive hole decreases. At large values of lattice constant, the material would be insulating, and at small values it would be metallic. In 1961, Mott suggested further that the transition between an insulating and the conducting state occurs sharply at critical value of the lattice constant for each material, which is known as the "Mott transition" [4]. Another phenomenon was observed in NiS by Sparks et al. in 1967 [5], where splitting of the d-band at the Néel temperature allowed all bands to be full or empty. Transition-metal oxides such as Ti_2O_3, V_2O_3, VO_2, and VO are all semi-conducting at low temperatures and show a transition into a metallic state at the Néel temperature. The electrical properties of these oxides were studied using thermo-conductive studies by Morin in 1959 (see figure 1) [6]. The transition was originally named a metal-to-insulator transition due to the changes in conductive properties of the materials. Other properties of these materials became soon apparent and it was therefore renamed as a semiconductor-to-metal transition.

Not all semiconductor-to-metal transitions are the result of electron-electron interactions, since changes in crystal structure may also lead to the formation of a band gap. Adler and Brooks [7] in 1967 presented two general models for a semiconductor-to-metal transition, in which the energy gap between the valence and conduction bands decreases linearly with the number of electrons excited across the gap. In one model the energy gap results from the splitting of the first Brillouin zone by an antiferromagnetic exchange interaction (second-order transition), and in the other it results from a crystalline-structure distortion to lower symmetry and creation of ion pairs (first-order transition).

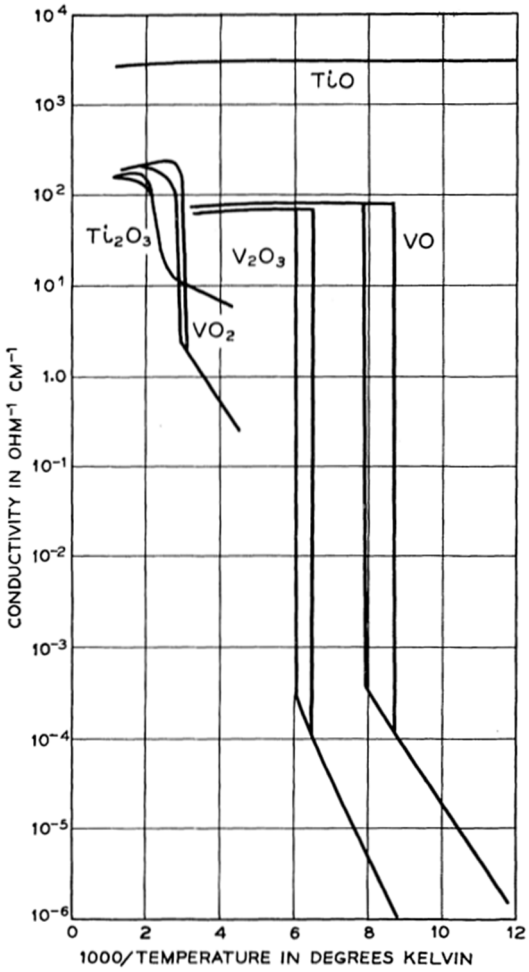

Figure 1. Conductivity as a function of reciprocal temperature for the lower oxides of titanium and vanadium [6].

The order of a phase transition is classified by considering the thermodynamic potential (e.g., the Gibbs free energy, G), and its derivatives at the transition (e.g., discontinuous first derivative of G corresponds to first-order transition). First-order transition results, when the entropy of the metallic phase brings the free energy down to the value of the semiconductor phase. In general, a first-order phase transition is accompanied by hysteresis and by the release or absorption of energy in the form of latent heat. The order of the transition can be clearly determined directly from Morin's electrical conductivity data. The presence of hysteresis indicates that V_2O_3, VO and VO_2 undergo first-order transitions, while Ti_2O_3 exhibits a second-order transition.

2.1 Semiconductor-to-metal transition in VO_2

Many of the vanadium oxides exhibit temperature-induced semiconductor-to-metal transition, e.g., VO, V_2O_3, VO_2 and the Magnéli phases V_nO_{2n-1} ($4 \leq n \leq 8$). Among them VO_2, with a $3d^1$ configuration, differs from others, as exhibits the nonmagnetic ground state without an antiferromagnetic phase. The semiconductor-to-metal transition in VO_2 takes place at the transition temperature, T_{tr}, around 340 K (68 °C). This transition can be highly repeatable in a thin film, whereas single crystals of VO_2 tend to

disintegrate during structural transformations. Figure 2 shows the lattice structural transition from a high-temperature tetragonal ($P4_2/mnm$) rutile structure (R phase) to a low-temperature monoclinic ($P2_1/c$) structure (M1 phase) [8]. High-temperature rutile structure is metallic due to the partial occupation of the lowest vanadium *d*-bands by the one outer electron not engaged in the V–O bonds. Low-temperature monoclinic structure is a distortion of high-temperature rutile structure. The structure involves V–V pairing with alternate shorter (0.265 nm) and longer (0.312 nm) V–V distances along the monoclinic a-axis, and tilting with respect to the rutile c-axis [9].

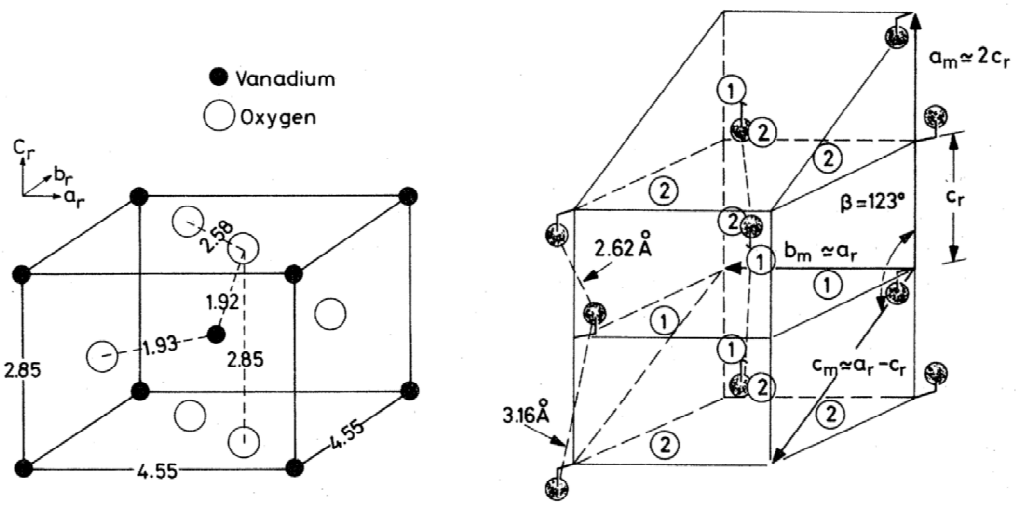

Figure 2. Left-hand side: high-temperature VO_2 tetragonal, rutile structure, space group $P4_2/mnm$. Right-hand side: low-temperature VO_2 monoclinic structure, space group $P2_1/c$. Open circles O^{2-}, closed circles V^{4+} [9].

Figure 3a shows schematically the one-electron band structure for tetragonal VO_2 with 3d, 4s, 4p energy levels for ionic V^{4+} on the left and the 2s, 2p energy levels for ionic 0^{2-} on the right. Electrostatic Madelung energy E_M for the effective charges on the ions is able to stabilize the 0^{2-}:2*p* orbitals relative to the V^{4+}:3*d* orbitals, even after the ionization energy of the cation and electron affinity of the anion are taken into account to reduce the stabilization energy to ($E_M - E_I$).

Below the transition temperature, T_{tr}, normal metallic band electrons become trapped in homo-polar V–V bonds. The displacement of a cation from the center of its interstice toward one or more anions is characteristic of a ferroelectric-type distortion. Goodenough in 1971 [10] proposed that the driving mechanism responsible for the transition may be an antiferroelectric transition. The absence of antiferromagnetic order and the structure of the monoclinic phase indicate that an antiferroelectric distortion is accompanied by V–V homo-polar bonding in low-temperature VO_2. Transition from metallic to semiconducting state requires two changes in the band structure. First, rising of the π^* bands above the Fermi energy E_F (leaving the d_{II} band half-filled). Second, splitting of d_{II} band. This change is illustrated in figure 3b. Cooperative displacement of each vanadium ion (dimerization in each V chain along the c axis) destabilizes the two π^* bands and shifts electrons to d_{II} states. Consequently, the twisting of V–V pairs due to an antiferroelectric shift of neighboring V atoms towards the apex oxygens (lying at the

axis perpendicular to the crystal c axis) increases the V-apex O hybridization and moves the π^* band above E_F so that only the d_{II} band is occupied. The new antiferroelectric component of the crystallographic distortion causes the doubling of the c-axis of the unit cell. Later, the translational symmetry of the dimerized V chains along the c axis splits the d_{II} band in two [10].

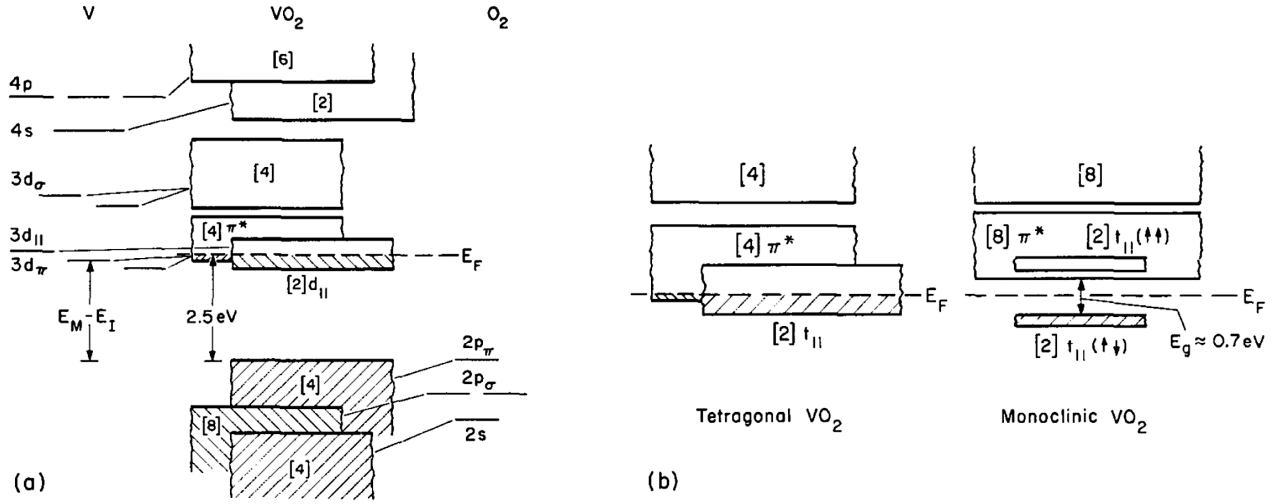

Figure 3. Schematic diagram of (a) one-electron band structure for tetragonal VO_2 and (b) *d*-band structure for tetragonal (metallic) and monoclinic (semiconducting) phase of VO_2 [10].

3 Vanadium oxides and difficult fabrication of thermochromic VO_2

Figure 4 shows the vanadium-oxygen phase diagram made by Wriedt [11]. The equilibrium solid phases of the V–O system at 0.1 MPa hydrostatic pressure are single-valence phases V, VO, V_2O_3, VO_2 and V_2O_5 and the mixed valence phases known as the Magnéli and Wadsley series, which can be written as V_nO_{2n-1} (n = 4 – 9) and V_nO_{2n+1} (n = 3, 4, 6), respectively. The phases V_9O_{17} and V_4O_9 might be marginally stable. The ranges in VO_2 and V_2O_5 are very narrow. Thin films of stoichiometric VO_2 are not easily fabricated because other vanadium oxides, such as V_3O_5, and V_2O_5, have stable structures in similar conditions as those used during VO_2 growth [12]. Among the binary transition metal oxides, vanadium dioxide shows a rich phase diagram with numerous non-hydrate polymorphs like VO_2 (M1), VO_2 (R), VO_2 (B), VO_2 (A), VO_2 (D), VO_2 (BCC) and VO_2 (N), which introduce a series of difficulties to fabricate pure VO_2 films with thermochromic properties [13,14]. VO_2 (B) is a metastable phase of vanadium dioxide, defined as an intermediate phase between V_2O_5 and V_2O_3. The phase transformation of VO_2 (B) phase into stable VO_2 (R) phase or into other intermediate VO_2 (A) phase often takes place during high-temperature annealing process [15].

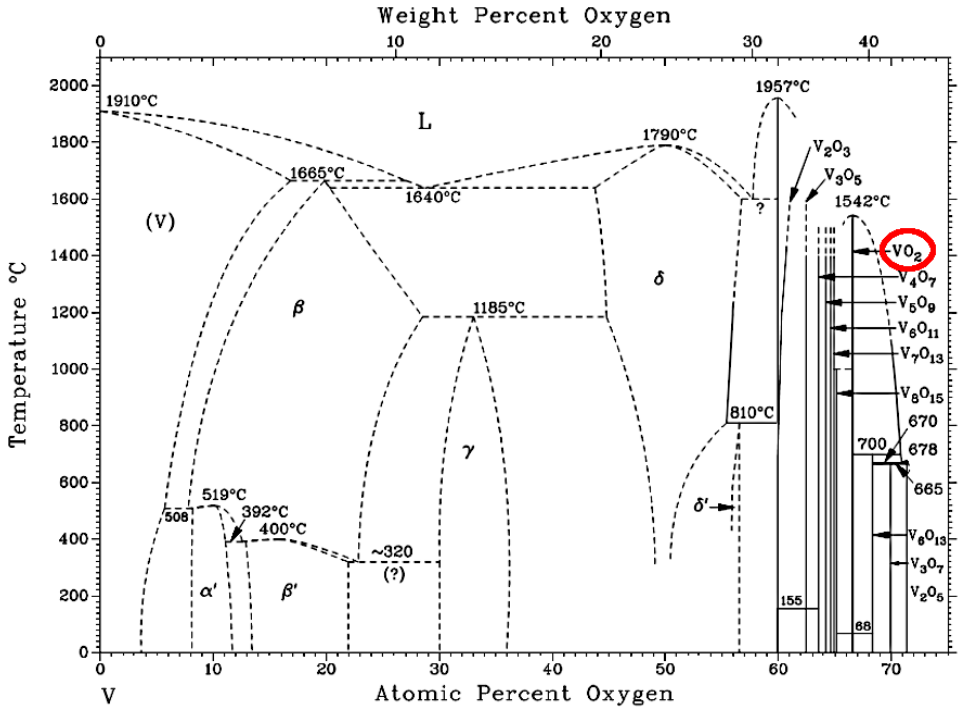

Figure 4. The vanadium-oxygen phase diagram (Condensed System, 0.1 MPa) as constructed by Wriedt [11].

4 High-power impulse magnetron sputtering with reactive gas flow control

Magnetron sputtering is a widely used deposition technology for thin films. Sputtering is the process of removing surface atoms from a target by particle (usually ion) bombardment. As the name suggests, the magnetron uses a magnet to effectively trap and utilize energetic electrons for ionization processes. This makes it possible to run glow discharge at lower pressures resulting in a higher quality of the growing films due to lower energy losses of sputtered particles on the path to the substrate [16].

Conventional direct current (DC) magnetron sputtering does not allow the generation of high-density plasma with a high degree of ionization, since the target power density is limited by thermal load of the target to several Wcm^{-2}. The combination of magnetron sputtering with ion assistance to film growth was the long standing goal. The first pulsed high-power magnetron discharges were demonstrated in Russia in the 1990s [17,18]. Consequently, Kouznetsov and coworkers [19] in 1999 published an important paper on the high-power impulse magnetron sputtering (HiPIMS) technique itself. The HiPIMS utilizes short impulses of 10s of microseconds at a low duty cycle (usually less than 10%) in order to achieve extremely high power densities (several $kWcm^{-2}$) with a high currents (usually 10s to 100s of amperes) at the comparable thermal loads of the target with conventional DC magnetron sputtering. The HiPIMS technique is characterized by highly ionized fluxes of particles with high fractions of ionized sputtered metal atoms onto the substrate and by enhanced energies of the ions bombarding the growing

films, allowing one to achieve film densification and crystallinity at a low substrate temperature and without a substrate bias voltage [20].

However, in spite of several successful applications of reactive HiPIMS to depositions of oxide films, there are still substantial problems with arcing on target surfaces during the reactive deposition processes at high target power densities (up to several kW cm^{-2}) in a pulse and with low deposition rates achieved. To avoid these problems, a feed-back pulsed reactive gas flow control (RGFC) of the reactive HiPIMS processes was proposed by team of Prof. Jaroslav Vlček from the Department of Physics at the University of West Bohemia in the frame of collaboration with the TRUMPF Hüttinger Company [21].

This feed-back process control makes it possible to maintain a sputter deposition of stoichiometric films in a region close to the metallic mode and thus to deliver a high power into discharge pulses without arcing on the target [20] which allows one to utilize the following exclusive benefits of the HiPIMS discharges: (i) intense sputtering of atoms from the target resulting in a substantially increased deposition rate, (ii) very high degrees of dissociation of RG molecules in the flux onto the substrate resulting in a higher incorporation of RG atoms into materials, (iii) a strong "sputtering wind" of the sputtered atoms resulting in a reduced flux of the RG particles onto the target and their enlarged flux onto the substrate, and (iv) highly ionized fluxes of particles onto the substrate and enhanced energies of the ions bombarding the growing films resulting in their structural changes and densification without a substrate bias.

The possibility of target oxidation (which would make using such high powers impossible) was suppressed not only by RGFC in itself, but also by the (i) O_2 inlet orientation towards the substrate and (ii) O_2 inlet location in the dense plasma in front of the target (which increases the degree of dissociation and subsequently the reactivity of oxygen, allowing one to achieve the desired film stoichiometry at a very low reactive gas partial pressure). The advantage of the proposed pulsed RGFC method is that it does not require any additional measurement or monitoring devices, such as, for example, plasma emission monitoring system, mass spectrometer or Lambda sensor [22,23], and that it is applicable to all magnetron sputtering discharges.

Previously, the combination of HiPIMS with RGFC used by Vlček et al. allowed to design pathways for high-rate deposition of stoichiometric oxides (ZrO_2 [20,21,24], Ta_2O_5 [21], HfO_2 [25]) and oxynitrides (Ta-O-N [26], Hf-O-N [27]), based on oscillating in the transition mode with a low compound fraction on the target surface. The combination of HiPIMS with RGFC is even more valuable for a reproducible deposition of defined O-poor (subsaturated) phases, such as VO_2 (at the first place allowing one to avoid V_2O_5 formation), and to promote crystallization and film densification at the low substrate temperature and without a substrate bias voltage.

5 Smart windows

5.1 Motivation for smart windows

People in industrialized countries currently spend 90% of their daily lives indoors, in buildings and in vehicles. The building sector is considered as the biggest single contributor to world energy consumption, and is responsible for one third of global greenhouse gas emissions leading to global warming. Considering the top three building energy consumers in the year 2010, U.S. and E.U. used for commercial and residential buildings more than 40% of their total energy consumption, and China, as the largest consumer of world energy, used 27% of their total energy consumption. Most of this energy was for the provision of lighting, heating, cooling, and air conditioning [28-30]. Windows are known as one of the most energy-inefficient components of buildings. Intelligent energy-saving windows (so called smart windows) based on thermochromic materials are able to selectively modulate infrared radiation in response to environmental temperature, thus to reduce air conditioning load to save energy or increase indoor environmental quality for higher comfort perceived by occupants or both.

5.2 Thermochromic glazing behavior

Thermochromic glazing behavior is visualized in figure 5. At the temperatures below the transition temperature, T_{tr}, the solar radiation and associated heat will reach the interior of the building, as it will not be reflected owing to a low reflectance of the material. On the contrary, the infrared reflectance of the material is much higher at the temperatures above T_{tr}, thus the part of the energy from the sun will be reflected. In this way, the heat gain from the solar radiation will be high in winter and much lower in summer [31].

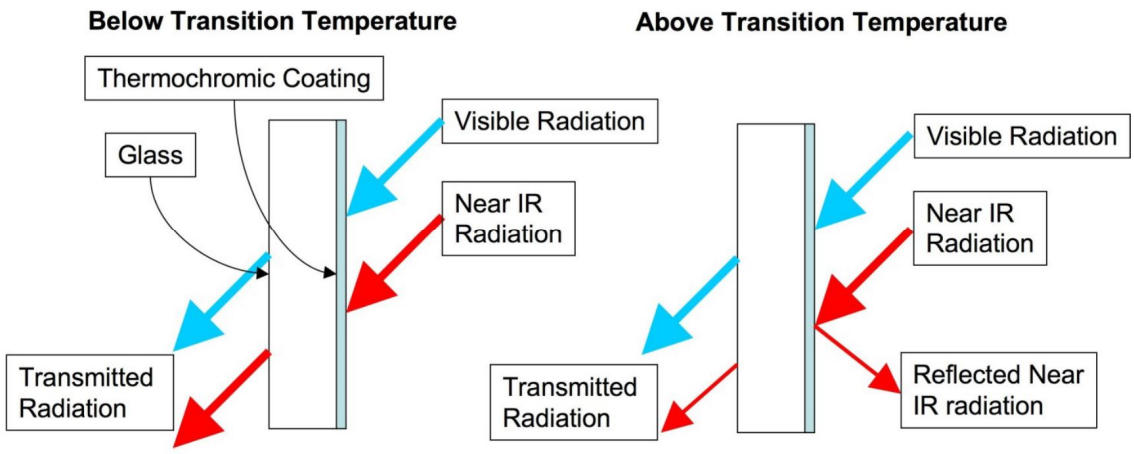

Figure 5. Schematic illustration of thermochromic glazing behavior [31].

The optical performance for smart-window application is represented by integral quantities, the luminous transmittance, T_{lum}, the solar transmittance, T_{sol}, and the modulation of the solar transmittance, ΔT_{sol}, respectively, given by equations (1), (2), and (3):

$$T_{\mathrm{lum}}(T_{\mathrm{m}}) = \int_{380}^{780} \varphi_{\mathrm{lum}}(\lambda)\varphi_{\mathrm{sol}}(\lambda)T(\lambda, T_{\mathrm{m}})d\lambda \,/ \int_{380}^{780} \varphi_{\mathrm{lum}}(\lambda)\varphi_{\mathrm{sol}}(\lambda)d\lambda\,, \tag{1}$$

$$T_{\mathrm{sol}}(T_{\mathrm{m}}) = \int_{300}^{2500} \varphi_{\mathrm{sol}}(\lambda)T(\lambda, T_{\mathrm{m}})d\lambda \,/ \int_{300}^{2500} \varphi_{\mathrm{sol}}(\lambda)d\lambda\,, \tag{2}$$

$$\Delta T_{\mathrm{sol}} = T_{\mathrm{sol}}(T_{\mathrm{m}} < T_{\mathrm{tr}}) - T_{\mathrm{sol}}(T_{\mathrm{m}} > T_{\mathrm{tr}})\,. \tag{3}$$

Here, T_{m} is measured temperature, φ_{lum} is the luminous sensitivity of the human eye and φ_{sol} is the solar spectral irradiance at an air mass of 1.5 (sun at an elevation of 41.81° above the horizon): for a 37° tilted surface at the sea level (see figure 6). The integral quantities T_{lum} and T_{sol} exhibit a strong dependence on the VO_2 film thickness.

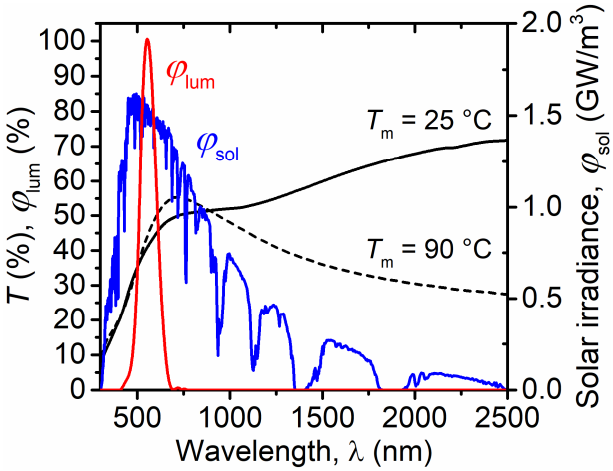

Figure 6. Spectral transmittance of the pure VO_2 layer (thickness 30 nm) measured below (25 °C) and above (90 °C) the transition temperature, together with the spectral dependence of the luminous sensitivity of the human eye (φ_{lum}, normalized to a maximum of 100%) and of the see-level solar irradiance at an air mass of 1.5 (φ_{sol}).

5.3 Limitations of pure VO_2 films for smart-window application

The research in the area of smart-window application is focused on removing of the following limitations:

1. The deposition temperature required for the formation of crystalline thermochromic VO_2 (typically over 400 °C) is high for industrial production.

2. The transition temperature $T_{tr} \approx 68$ °C (for bulk VO_2) is too high.

3. The modulation of the solar transmittance, ΔT_{sol}, of pure VO_2 films is less than 10%.

4. The luminous transmittance, T_{lum}, of pure VO_2 films with a noticeable magnitude of ΔT_{sol} is less than 40%, which is too low for most applications to windows in buildings [32].

Items (1) to (4) form the challenges that must be met for smart-window application. It is necessary to decrease the deposition temperature of crystalline VO_2 down to 300 °C, ideally without any substrate bias in order (i) to facilitate the large-scale production by reducing the energy consumption and minimizing problems with temperature uniformity over large substrate surfaces, (ii) to limit the diffusion of harmful elements from substrates, such as soda-lime glass, and (iii) to allow deposition on temperature-sensitive plastic substrates [33]. The change of T_{sol} should take place in the comfort temperature range 20 – 25 °C [31]. The reduction of the T_{tr} from 68 °C (bulk materials) or 50 – 70 °C (thin films) to the comfort temperature can be achieved by a doping of VO_2 by other metals [34]. The trade-off between a high T_{lum} and high ΔT_{sol} of thermochromic VO_2 films limits their applicability to energy efficient fenestration. The papers [35,36] report on the minimum required value of $T_{vis} = 60\%$ (maximum transmittance in the visible region) to avoid an extra energy spent on indoor lighting. The work [37] suggests that the T_{lum} should be higher than 50% at least for daily application. Most recently, the goal of T_{lum} higher than 60% was reported in [38]. Integral quantities T_{lum} and ΔT_{sol} representing optical properties can be improved, e.g. by antireflection (AR) layers.

6 References

[1] Kiria P, Hyett G and Binions R 2010 Solid state thermochromic materials *Adv. Mater. Lett.* **1** 86–105

[2] Boer J H de and Verwey E J W 1937 Semi-conductors with partially and with completely filled 3d -lattice bands *Proc. Phys. Soc.* **49** 59–71

[3] Mott N F and Peierls R 1937 Discussion of the paper by de Boer and Verwey *Proc. Phys. Soc.* **49** 72–3

[4] Mott N F 1968 Metal-Insulator Transition *Rev. Mod. Phys.* **40** 677–83

[5] Sparks J T and Komoto T 1967 Metal-to-semiconductor transition at the magnetic ordering temperature of NiS *Phys. Lett. A* **25** 398–9

[6] Morin F J 1959 Oxides which show a metal-to-insulator transition at the neel temperature *Phys. Rev. Lett.* **3** 34–6

[7] Adler D and Brooks H 1967 Theory of Semiconductor-To-Metal Transitions *Phys. Rev.* **155** 826-40

[8] Imada M, Fujimori A and Tokura Y 1998 Metal-insulator transitions *Rev. Mod. Phys.* **70** 1039-263

[9] Zylbersztejn A and Mott N F 1975 Metal-insulator transition in vanadium dioxide *Phys. Rev. B* **11** 4383–95

[10] Goodenough J B 1971 The two components of the crystallographic transition in VO_2 *J. Solid State Chem.* **3** 490–500

[11] Wriedt H A 1989 The O-V (Oxygen-Vanadium) System *Bull. Alloy Phase Diagrams* **10** 271–7

[12] Ningyi Y, Jinhua L and Chenglu L 2002 Valence reduction process from sol-gel V_2O_5 to VO_2 thin films *Appl. Surf. Sci.* **191** 176–80

[13] Leroux C, Nihoul G and Van Tendeloo G 1998 From VO_2 (B) to VO_2 (R): Theoretical structures of VO_2 polymorphs and in situ electron microscopy *Phys. Rev. B* **57** 5111–21

[14] Rao Popuri S, Artemenko A, Labrugere C, Miclau M, Villesuzanne A and Pollet M 2014 VO_2 (A): Reinvestigation of crystal structure, phase transition and crystal growth mechanisms *J. Solid State Chem.* **213** 79–86

[15] Wang X J, Li H D, Fei Y J, Wang X, Xiong Y Y, Nie Y X and Feng K A 2001 XRD and Raman study of vanadium oxide thin films deposited on fused silica substrates by RF magnetron sputtering *Appl. Surf. Sci.* **177** 8–14

[16] Anders A 2017 Tutorial : Reactive high power impulse magnetron sputtering (R-HiPIMS) *J. Appl. Phys.* **121** 171101

[17] Mozgrin D V., Fetisov I K and Khodachenko G V. 1995 High-Current Low-Pressure Quasi-Stationary Discharge in a Magnetic Field: Experimental Research *Plasma Phys. Reports* **21** 400-9

[18] Bugaev S P, Koval N N, Sochugov N S and Zakharov A N 1996 Investigation of a High-Current Pulsed Magnetron Discharge Initiated in the Low-Pressure Diffuse Arc Plasma *XVIIth Int. Symp. Discharges Electr. Insul. Vacuum-Berkeley-1996* 1074–6

[19] Kouznetsov V, Macák K, Schneider J M, Helmersson U and Petrov I 1999 A novel pulsed magnetron sputter technique utilizing very high target power densities *Surf. Coatings Technol.* **122** 290–3

[20] Vlček J, Rezek J, Houška J, Kozák T and Kohout J 2015 Benefits of the controlled reactive high-power impulse magnetron sputtering of stoichiometric ZrO_2 films *Vacuum* **114** 131–41

[21] Vlček J, Rezek J, Houška J, Čerstvý R and Bugyi R 2013 Process stabilization and a significant enhancement of the deposition rate in reactive high-power impulse magnetron sputtering of ZrO_2 and Ta_2O_5 films *Surf. Coatings Technol.* **236** 550–6

[22] Safi I 2000 Recent aspects concerning DC reactive magnetron sputtering of thin films: a review *Surf. Coatings Technol.* **127** 203–19

[23] Sproul W D, Christie D J and Carter D C 2005 Control of reactive sputtering processes *Thin Solid Films* **491** 1–17

[24] Belosludtsev A, Vlček J, Houška J and Čerstvý R 2017 Reactive high-power impulse magnetron sputtering of ZrO_2 films with gradient ZrO_x interlayers on pretreated steel substrates *J. Vac. Sci. Technol. A Vacuum, Surfaces, Film.* **35** 031503

[25] Vlček J, Belosludtsev A, Rezek J, Houška J, Čapek J, Čerstvý R and Haviar S 2016 High-rate reactive high-power impulse magnetron sputtering of hard and optically transparent HfO_2 film *Surf. Coatings Technol.* **290** 58–64

[26] Rezek J, Vlček J, Houška J and Čerstvý R 2014 High-rate reactive high-power impulse magnetron sputtering of Ta-O-N films with tunable composition and properties *Thin Solid Films* **566** 70–7

[27] Belosludtsev A, Houška J, Vlček J, Haviar S, Čerstvý R, Rezek J and Kettner M 2017 Structure and properties of Hf-O-N films prepared by high-rate reactive HiPIMS with smoothly controlled composition *Ceram. Int.* **43** 5661–7

[28] Cao X, Dai X and Liu J 2016 Building energy-consumption status worldwide and the state-of-the-art technologies for zero-energy buildings during the past decade *Energy Build.* **128** 198–213

[29] Allouhi A, El Fouih Y, Kousksou T, Jamil A, Zeraouli Y and Mourad Y 2015 Energy consumption and efficiency in buildings: current status and future trends *J. Clean. Prod.* **109** 118–30

[30] Omer A M 2008 Energy, environment and sustainable development *Renew. Sustain. Energy Rev.* **12** 2265–300

[31] Saeli M, Piccirllo C, Warwick M and Binions R 2013 Thermochromic Thin Films: Synthesis, Properties and Energy Consumption Modelling *Mater. Process. energy Commun. Curr. Res. Technol. Dev.* 736–46

[32] Li S-Y, Niklasson G a. and Granqvist C G 2012 Thermochromic fenestration with VO_2-based materials: Three challenges and how they can be met *Thin Solid Films* **520** 3823–8

[33] Choi Y, Jung Y and Kim H 2016 Low-temperature deposition of thermochromic VO_2 thin films on glass substrates *Thin Solid Films* **615** 437–45

[34] Sun C, Yan L, Yue B, Liu H and Gao Y 2014 The modulation of metal-insulator transition temperature of vanadium dioxide: a density functional theory study *J. Mater. Chem. C* **2** 9283-93

[35] Hu L, Tao H, Chen G, Pan R, Wan M, Xiong D and Zhao X 2016 Porous W-doped VO_2 films with simultaneously enhanced visible transparency and thermochromic properties *J. Sol-Gel Sci. Technol.* **77** 85–93

[36] Kamalisarvestani M, Saidur R, Mekhilef S and Javadi F S 2013 Performance , materials and coating technologies of thermochromic thin films on smart windows *Renew. Sustain. Energy Rev.* **26** 353–64

[37] Chang T C, Cao X, Bao S H, Ji S D, Luo H J and Jin P 2018 Review on thermochromic vanadium dioxide based smart coatings: from lab to commercial application *Adv. Manuf.* **6** 1–19

[38] Baloukas B, Loquai S and Martinu L 2018 VO_2-based thermally active low emissivity coatings *Sol. Energy Mater. Sol. Cells* **183** 25–33

II Aims of the thesis

This Ph.D. thesis deals with preparation and characterization of thermochromic VO_2-based coatings. They were deposited using a pulsed reactive magnetron sputtering onto floating substrates at low substrate temperatures (less than 330 °C). Particular aims of the thesis were formulated as follows:

1. To use reactive HiPIMS with a pulsed O_2 flow control for depositions of thermochromic VO_2 films onto floating Si substrates at low substrate surface temperatures (less than 300 °C).

2. To investigate the correlations between the ion-flux characteristics at a substrate position and the corresponding discharge parameters (particularly the voltage pulse duration and oxygen partial pressure) during controlled low-temperature (300 °C) reactive HiPIMS depositions of VO_2 films with a pronounced semiconductor-to-metal transition onto conventional soda-lime glass substrates without any substrate bias voltage and without any interlayer. To propose explanation of the pronounced semiconductor-to-metal transition.

3. To propose a magnetron sputtering method for deposition of antireflection SiO_2 layers on the top of thermochromic VO_2 layers, and to investigate the dependence of the luminous transmittance, T_{lum}, and the modulation of the solar transmittance, ΔT_{sol}, of the thermochromic VO_2/SiO_2 coatings, prepared on soda-lime glass, on the SiO_2 layer thickness.

4. To propose a magnetron sputtering method, used simultaneously with the controlled reactive HiPIMS, for atomic doping of VO_2 by W to reduce the semiconductor-to-metal transition temperature to room temperature without concessions in terms of coating optical properties.

5. To prepare and investigate a three-layer ZrO_2/VO_2-W/ZrO_2 system on soda-lime glass (the surface temperature less than 330 °C) with the aim to achieve the semiconductor-to-metal transition temperature close to 25 °C, the luminous transmittance $T_{lum} > 40\%$ and the modulation of the solar transmittance $\Delta T_{sol} > 10\%$ at a high mechanical and chemical protection of the coatings.

III Results

The results are presented in a form of six papers in prestigious international journals (A–F) and one draft of the paper intended for submission into a prestigious international journal (G). These papers include the most important results obtained during my Ph.D. study at the Faculty of Applied Science, University of West Bohemia in Pilsen since September 2014.

I carried out all depositions of the VO_2 and VO_2-W films presented (A–G), together with all discharge and deposition characteristics (B, E, and G). I participated in development of a new custom-designed heating cell for the measurement of spectroscopic transmittance at elevated temperatures and of the temperature dependence of infrared transmittance. Moreover, I upgraded our heating cell by a cooling element for the possibility to measure below room temperature and to increase the measurement rate.

I measured the data and interpreted the results obtained for the spectral transmittances at various temperatures (C, D, F, and G) and for the temperature dependence of infrared transmittance (B–G), and for electrical properties (B, C, and E) of the prepared films. The interpretation of the results includes also the calculations of the integral quantities T_{lum} and ΔT_{sol} which characterize the optical performance of the films. In addition, I actively participated in interpretation of the results obtained for the phase composition of the films (B–G). I wrote the first versions of the papers D, E and G, and I actively participated in writing the papers A, B, C and F.

A Characterization of thermochromic VO_2 (prepared at 250 °C) in a wide temperature range by spectroscopic ellipsometry

J. Houska, **D. Kolenaty**, J. Rezek, J. Vlcek

Appl. Surf. Sci. 421 (2017) 529–534

Applied Surface Science 421 (2017) 529–534

Contents lists available at ScienceDirect

Applied Surface Science

journal homepage: www.elsevier.com/locate/apsusc

Full Length Article

Characterization of thermochromic VO_2 (prepared at 250 °C) in a wide temperature range by spectroscopic ellipsometry

J. Houska*, D. Kolenaty, J. Rezek, J. Vlcek

Department of Physics and NTIS – European Centre of Excellence, University of West Bohemia, Univerzitni 8, 30614 Plzen, Czechia

ARTICLE INFO

Article history:
Received 14 June 2016
Received in revised form 14 October 2016
Accepted 16 October 2016
Available online 17 October 2016

Keywords:
VO_2
Thermochromic coatings
Ellipsometry
Raman spectroscopy
HiPIMS
Deposition temperature

ABSTRACT

The paper deals with thermochromic VO_2 prepared by reactive high-power impulse magnetron sputtering and characterized by spectroscopic ellipsometry. We focus on the dispersion of optical constants in a wide temperature range and on the transmittance predicted using the optical constants. While the thermochromic behavior of VO_2 in itself has been reported previously (particularly above the room temperature, RT), in this paper we present (i) optical properties achieved at a low deposition temperature of 250 °C and without any substrate bias voltage (which dramatically increases the application potential of the coating) and (ii) changes of these properties not only above but also below RT (down to −30 °C). The properties include very low (for VO_2) extinction coefficient at RT (0.10 at 550 nm), low transition temperature of around or even below 50 °C (compared to the frequently cited 68 °C) and high modulation of the predicted infrared transmittance (e.g. 39% at −30 °C, 30% at RT and 3.4% above the transition temperature at 2000 nm for a 100 nm thick coating on glass). The results are important for the design of thermochromic coatings, and pathways for their preparation under industry-friendly conditions, for various technological applications.

1. Introduction

Thermochromism is a phenomenon dealing with temperature-dependent changes of the electronic structure of a material. This leads to temperature-dependent optical properties (infrared transmittance at the first place), electrical properties, (electronic part of) thermal conductivity, etc. This opens numerous applications especially within the worldwide efforts to reduce the energy consumption [1,2] (control of the transmission of solar radiation through "smart" windows, control of heat fluxes in cars, etc.). Applications of thermochromic materials in optical switches, smart radiator devices or as a protection of sensitive infrared detectors from strong laser radiation are of interest as well [3,4]. In parallel to the efforts to maximize the temperature-dependent changes of the aforementioned properties, individual applications lead to specific requirements such as thermochromic transition temperature close to the room temperature (RT), high transmittance in the visible range, low preparation temperature in the case of temperature-sensitive substrates (e.g. flexible polymers) or simple preparation procedure (e.g. without any substrate bias voltage).

The vanadium oxide system exhibits thermochromic behavior for a wide range of compositions [5]. VO_2 is currently the most studied phase due to its thermochromic transition temperature (around 68 °C for the bulk material [6]) relatively close to RT. This compound exhibits a reversible transition between a low temperature monoclinic ("M1"; distorted rutile) semiconductive phase and a high-temperature tetragonal ("R"; perfect rutile) metallic phase. The transition temperature can be further altered by dopants such as Mo, W or Nb (this is however beyond the scope of the present paper), see e.g. Refs. [7,8] for an overview. In recent years, number of pathways for a deposition of crystalline thermochromic VO_2 in the form of thin films by magnetron sputtering have been reported [9–12]. However, an important thing to note is that the application potential of these state of the art VO_2 preparation techniques is frequently limited by the necessity to use rf substrate bias [9,11], dc substrate bias [12] (which requires a conductive substrate, e.g. indium tin oxide-coated glass in Ref. [12]) or post-deposition annealing [10].

Thus, on the one hand, the basic fact that VO_2 is a thermochromic material is well known. On the other hand, in the present paper we go beyond the state of the art in the following directions. First, we study the temperature dependence of VO_2 optical properties in a wide temperature range (with all applications, not "only" the smart windows, in mind), not only above but also well below RT. This kind

* Corresponding author.
E-mail address: jhouska@kfy.zcu.cz (J. Houska).

http://dx.doi.org/10.1016/j.apsusc.2016.10.084
0169-4332/

of information, despite its importance, is more difficult to measure and not common in the literature (for electrical resistivity – but not optical properties – of VO_2 below RT see Ref. [13]). Second, using high-power impulse magnetron sputtering (HiPIMS) with reactive gas flow control (RGFC; see Sec. 2.1 for details) allowed us to prepare VO_2 at a low substrate surface temperature of 250 °C and without any substrate bias voltage. This is contrary to the available literature (which does not include any information about VO_2 prepared without substrate bias below 400 °C) and it dramatically increases the application potential of the coating. Third, we show that the coating properties (e.g. low visible-range extinction coefficient and low transition temperature) which can be achieved under these industry-friendly deposition conditions are still superior.

While the present paper is (following the scope of this issue) focused on detailed ellipsometric characterization of a single coating prepared under the aforementioned conditions, the effect of deposition conditions and substrate choice (briefly summarized in Sec. 2.1) will be reported separately.

2. Methodology

2.1. VO_2 deposition

The VO_2 coating studied was deposited on a rotating (20 rpm) Si(100) substrate by reactive HiPIMS (ATC 2200-V AJA International Inc. sputter system with TruPlasma Highpulse 4002 Hüttinger Elektronik power supply) of V target (50 mm in diameter) in $Ar + O_2$ plasma. Pre-deposition substrate cleaning using rf discharge (50 W for 5 min) has been performed. The deposition time was 40 min and the room temperature coating thickness measured by ellipsometry (Sec. 2.2) was 82 nm, i.e. the deposition rate was 2 nm/min. The substrate, placed 150 mm from the target, was at a floating potential. The substrate surface temperature of 250 °C was maintained during the deposition by a built-in heating system calibrated using a thermocouple directly attached to the substrate surface. The voltage pulse duration was 80 μs, the duty cycle was 1% and the frequency was 125 Hz. The power density averaged over the deposition and the target area was approximately 13 Wcm^{-2} and the peak power density in a pulse was 5 kWcm^{-2}. The base pressure was $<10^{-4}$ Pa. The Ar partial pressure was 1 Pa at a fixed Ar flow rate of 60 sccm, and the O_2 partial pressure was 0.01-0.03 Pa.

The key part of the deposition procedure was reactive gas flow control (RGFC): the O_2 flow rate was not fixed but pulsing between 0 and 2 sccm, and the duration of the O_2 flow pulses was decided during the deposition by a programmable logical controller using pre-selected critical values of O_2 partial pressure. Previously the combination of HiPIMS with RGFC allowed us to perform high-rate deposition of stoichiometric ZrO_2 [14,15], Ta_2O_5 [15,16] or HfO_2 [17]. Note that while the ability to oscillate around an optimum O_2 partial pressure is valuable for O-rich (saturated) phases such as the aforementioned ones or V_2O_5 (allowing one to avoid both the understoichiometry and the target poisoning), it is even more valuable for a reproducible deposition of defined O-poor (subsaturated) phases such as VO_2 (at the first place allowing one to avoid V_2O_5 formation).

The most crucial process parameters include the voltage pulse duration and the critical value of O_2 partial pressure. The critical value of O_2 partial pressure leading to a composition close to VO_2 has to be chosen within a narrow window (±10%), identified separately for each voltage pulse duration and each system geometry (including e.g. the actual sputter target thickness). In parallel, the aforementioned procedure becomes even more difficult (the aforementioned window closes from ±10% to zero) at an improper voltage pulse duration, which affects the compound fraction on the sputtered target and the ion flux characteristics (energy distribution and composition) on the growing films. The optimum voltage pulse duration as well as the required deposition temperature are different for different substrate structures and conductivities: 80 μs and 250 °C for semiconductive crystalline Si, 50 μs and 300 °C (still well below the values achieved – without substrate bias – in the literature) for insulating amorphous glass (not shown).

2.2. VO_2 characterization

The thermochromic behavior of the VO_2 coating prepared was determined by variable angle spectroscopic ellipsometry (VASE; J.A. Woollam Co. Inc.) equipped with a temperature controlled stage. The stage was either ohmically heated or cooled by N_2, and the temperature was controlled by the Instec STC200 controller. In Sec. 3 we show and discuss (i) the raw data, namely the ellipsometric angles Ψ and Δ ($r_p/r_s = \tan\Psi . e^{i\Delta}$ where r_p and r_s is the reflectivity of p- and s-polarized light, respectively), (ii) dispersion of the refractive index (n) and the extinction coefficient (k) calculated from the raw data, (iii) dispersion of the transmittance (T) of the same coating on a 1 mm thick float glass substrate calculated from n and k, (iv) n, k and T at specific wavelengths (λ) such as 550 nm (n_{550}, k_{550} and T_{550}, respectively) and (v) integral quantities T_{lum} and T_{sol} defined by Eqs. (1) and (2)

$$T_{lum} = \int_{300}^{2500} \varphi_{lum}(\lambda)\varphi_{sol}(\lambda)T(\lambda, T_m)d\lambda \Big/ \int_{300}^{2500} \varphi_{lum}(\lambda)\varphi_{sol}(\lambda)d\lambda \quad (1)$$

$$T_{sol} = \int_{400}^{700} \varphi_{sol}(\lambda)T(\lambda, T_m)d\lambda \Big/ \int_{400}^{700} \varphi_{sol}(\lambda)d\lambda \quad (2)$$

where φ_{lum} is the luminous sensitivity of the human eye and φ_{sol} is the solar irradiance spectrum at the sea level ([18]). The measurement temperature (T_m) was controlled between −30 and 100 °C. Two types of data were obtained: (i) dependence of Ψ on T_m (hysteresis curve) between −30 and 100 °C at a selected wavelength of 2000 nm, and (ii) complete dispersion of Ψ and Δ (and consequently n and k) at nine selected temperatures of −30, −5, 10, 25, 40, 50, 60, 70 and 100 °C. The angle of incidence (in reflection) was 70° (all measurements) and 65 and 75° (cross-check at T_m = 25 and 100 °C). The heating/cooling rate was 3°/min., and the hold time used to collect the spectroscopic data (for the single angle of incidence and each of the selected temperatures) was 29 min.

The optical data were fitted using the WVASE software and an optical model consisting of a c-Si substrate, a bulk VO_2 layer and a surface roughness layer. Two different models were used to represent bulk VO_2. The main one (which the n and k below are based on) is based on a combination of the Cody-Lorentz dispersion formula (oscillator) with 2–3 Lorentz oscillators. The other one is based on a combination of the Cody-Lorentz formula, a Lorentz oscillator and a Drude oscillator, with the Drude oscillator being the only oscillator centered in the low-energy range (below 2.5 eV). The latter model (an attempt to explain the dispersion in the infrared range predominantly by the free charge carrier absorption) did not lead to a better fit, but allowed us to discuss the evolution of the parameters of the Drude oscillator (Sec. 3.3).

In addition to the ellipsometric measurements, the VO_2 phase composition was confirmed by Raman spectroscopy (Horiba Jobin Yvon LABRAM HR Evolution instrument using a 532 nm laser).

3. Results and discussion

This section is organized as follows. First, the phase structure of the coating (Fig. 1) is confirmed in Sec. 3.1. Second, the raw data measured (temperature dependence and dispersion of the ellipso-

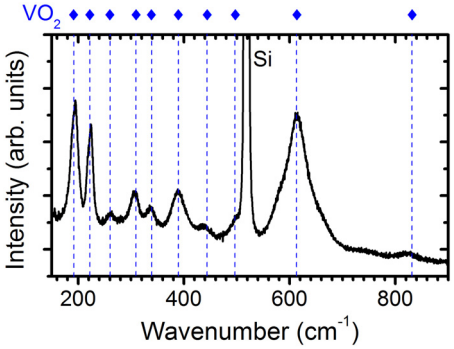

Fig. 1. Raman spectrum of the VO_2 material studied. The vertical dashed lines correspond to the VO_2 peak positions as identified in Ref. [19].

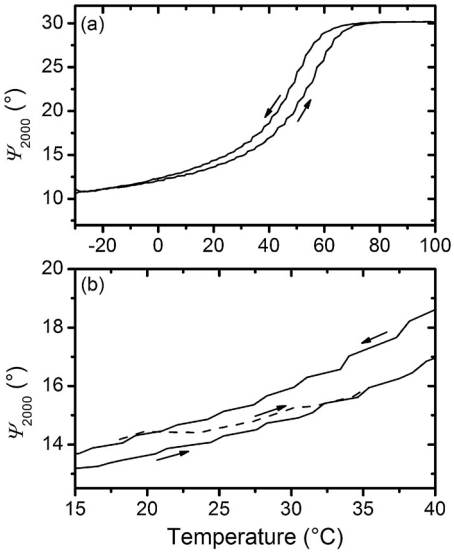

Fig. 2. Temperature (T_m) dependence of the ellipsometric angle Ψ at a wavelength of 2000 nm (Ψ_{2000}). Panel a shows the whole reproducible hysteresis curve. Panel b shows the hysteresis curve around RT (solid line) and the data obtained when the measurement started by heating from RT (dashed line).

metric quantities; Figs. 2–3) are presented in Sec. 3.2. Third, the materials properties (collected during the cooling part of the heating/cooling cycle; Figs. 4–6) are presented in Sec. 3.3. Fourth, the calculated transmittance which the materials properties (for various coating thicknesses) lead to (Figs. 7–9) is discussed in Sec. 3.4.

3.1. Materials structure

Fig. 1 shows the Raman spectrum of the coating studied. Indeed, it can be seen that all peak positions (195, 224, 264, 310, 339, 392, 442, 496, 615 and 833 cm^{-1}) very well correspond (within 3 cm^{-1}) to the VO_2 vibration modes as identified e.g. in Ref [19] or [11]. Let alone the substrate peak at 513–520 cm^{-1} (microcrystalline and crystalline Si, respectively). No peak(s) corresponding to any other vanadium oxide phase (including the most stable V_2O_5) have been identified. This demonstrates (consistently with the optical properties discussed below) two important facts. First, using RGFC allowed us to achieve (approximately) the required VO_2 elemental composition. Second, using HiPIMS (and avoiding target poisoning using RGFC) allowed us to deliver the aforementioned high power (5 $kWcm^{-2}$ in a pulse) into the plasma. This led to a high degree of ionization of arriving atoms and consequently to a high energy and momentum delivered into the growing film, which allowed

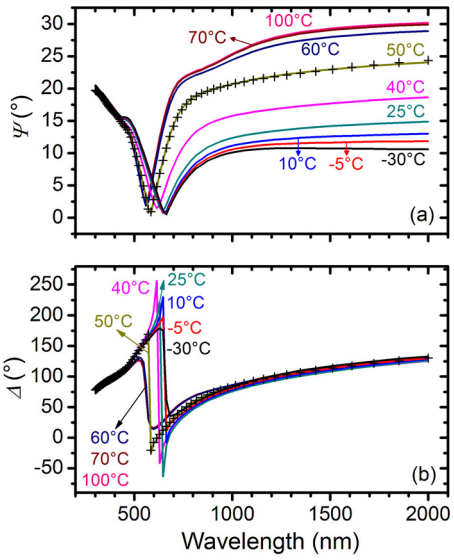

Fig. 3. Spectral dependence of the ellipsometric angles Ψ (panel a) and Δ (panel b) at nine selected T_m values. The lines show experimental data and the crosses show (an example of) fitted data at 50 °C.

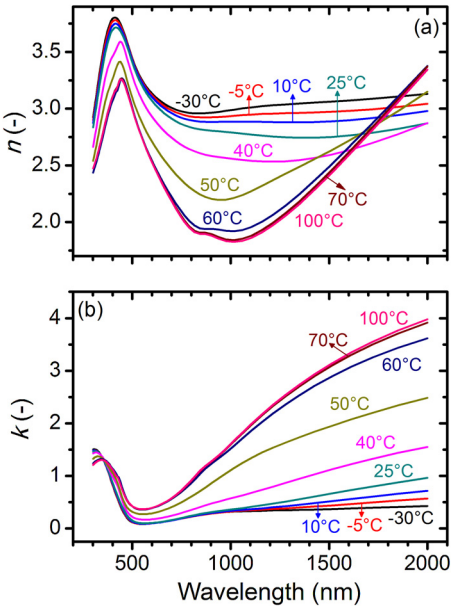

Fig. 4. Spectral dependence of the refractive index (n; panel a) and the extinction coefficient (k; panel b) of the VO_2 material studied at nine selected T_m values.

us to prepare crystalline VO_2 even at the low substrate surface temperature of 250 °C and without any substrate bias.

3.2. Temperature dependence of ellipsometric quantities

Fig. 2 shows the dependence of the ellipsometric angle Ψ_{2000} on T_m (-30 to 100 °C). Multiple heating/cooling cycles confirmed that the resulting hysteresis curve is fully reproducible. Note that two processes affecting the optical properties take place in parallel: (i) the aforementioned structural transition between the low temperature monoclinic semiconductor and the high temperature tetragonal metal, and (ii) (not always discussed, but equally important) temperature dependent concentration of free charge carriers in the narrow band gap (0.7 eV [20]) low temperature semiconductor. Consequently, the hysteresis curve is far from symmetrical: above the transition temperature (metal) the $\Psi_{2000}(T_m)$

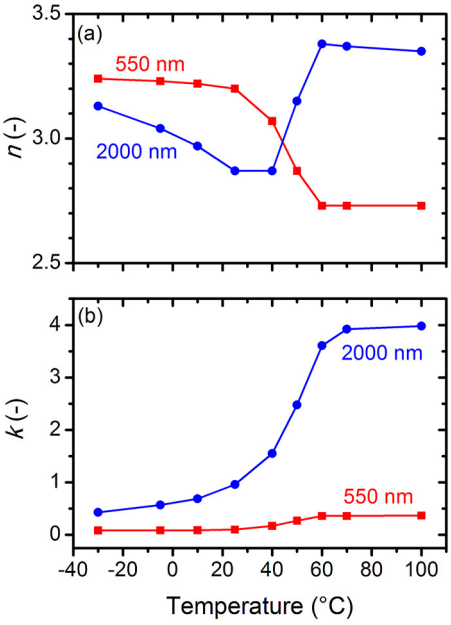

Fig. 5. Temperature (T_m) dependence of the refractive index (n; panel a) and the extinction coefficient (k; panel b) of the VO_2 material studied at a wavelength of 550 nm (squares) and 2000 nm (balls).

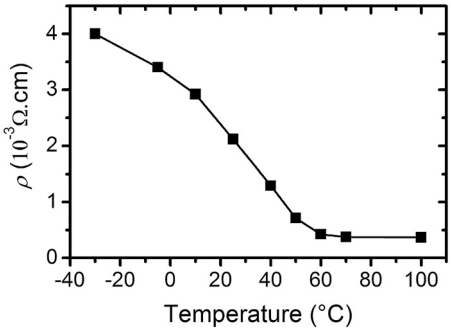

Fig. 6. Temperature (T_m) dependence of the parameter ρ of the Drude oscillator in the case when it was the only oscillator centered in the low-energy range.

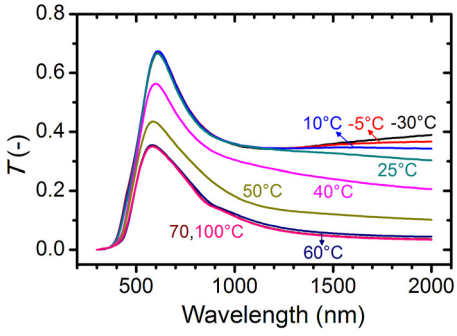

Fig. 7. Calculated spectral dependence of the transmittance (T) of 1 mm thick float glass coated by 100 nm thick VO_2 at nine selected T_m values.

dependence quickly becomes horizontal, while below the transition temperature (semiconductor) the Ψ_{2000} changes continue in a wide T_m range. This is in full agreement with the temperature dependence of the electrical resistivity of VO_2 reported in Ref. [13]. The dashed line in Fig. 2b shows how the hysteresis curve would look like in a case of measurement only above RT.

The transition temperature defined by half of the total Ψ_{2000} change is 45 °C (41 and 49 °C for the cooling and the heating part

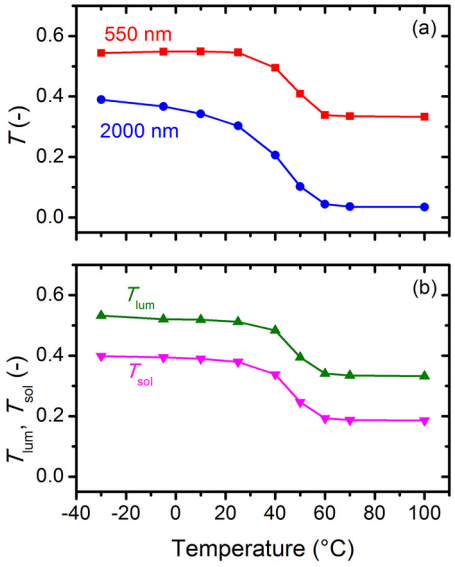

Fig. 8. Calculated temperature (T_m) dependence of the transmittance (T) at a wavelength of 550 nm (panel a, squares), T at 2000 nm (panel a, balls), T_{lum} (panel b, triangles up) and T_{sol} (panel b, triangles down) of 1 mm thick float glass coated by 100 nm thick VO_2.

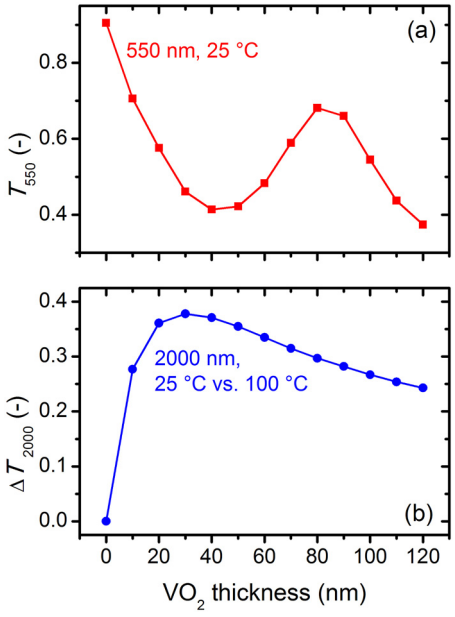

Fig. 9. Calculated dependence of the transmittance of 1 mm thick float glass coated by VO_2 on the coating thickness. Panel a shows T_{550} at T_m = 25 °C. Panel b shows the difference between T_{2000} at T_m = 25 °C and at T_m = 100 °C (ΔT_{2000}, T_{2000} modulation).

of the cycle, respectively) and the transition temperature defined by the inflection point of the temperature dependence (maximum temperature derivative) of Ψ_{2000} is 53 °C (50 and 56 °C for the cooling and the heating part of the cycle, respectively). Let us emphasize that while the transition temperature given by the aforementioned superposition of structural transition and changing concentration of free charge carriers may be slightly different from a temperature defining the structural transition alone, the former quantity is that one which matters from the application point of view. Note that the transition temperature is well below the aforementioned bulk value of 68 °C [6], indicating its dependence on the crystal size.

Fig. 3 shows the dispersion of Ψ and Δ at the nine selected temperatures between −30 and 100 °C. Again, a strong thermochromic effect with maximum derivative close to 50 °C can be observed. Fur-

thermore, for T_m = 50 °C the figure confirms that the optical model used (Sec. 2.2) leads to almost perfect fit in the whole measurement range. The fact that a good fit could be obtained without including any thickness gradient (resulting from a presence of voids) in the optical model indicates high VO_2 densification resulting from using HiPIMS (often contrary to other deposition techniques, see e.g. the discussion in Ref. [11]).

3.3. Temperature dependence of materials properties

Temperature dependence of the VO_2 optical constants n and k is shown in complementary Figs. 4 (dispersion in a wide range) and 5 (dependence on T_m at 550 and 2000 nm). Fig. 4a shows a clear $n(T_m)$ dependence in the whole wavelength range, in particular decreasing in the visible, strongly decreasing around 1000 nm and non-monotonous above approximately 1400 nm. Fig. 4b shows that the rate of the $k(T_m)$ dependence increases with increasing wavelength (decreasing photon energy), i.e. with increasing photon absorption by free charge carriers. Indeed, the main part of the thermochromic effect is due to the temperature-dependent concentration of free charge carriers (resulting from both the temperature-dependent band gap and the temperature-dependent occupation of electronic states [smearing around the Fermi level] even at a given band gap, see also Sec. 3.2).

Quantitatively, Fig. 5a shows that n_{550} changes from 3.24 (T_m = -30 °C) through 3.20 (25 °C) to 2.73 (100 °C), while n_{2000} changes non-monotonously from 3.13 (T_m = –30 °C) through 2.87 (25 °C) to 3.35 (100 °C). Fig. 5b shows that k_{550} changes from 0.085 (T_m = -30 °C) through 0.10 (25 °C) to 0.37 (100 °C), while k_{2000} changes from 0.43 (T_m = -30 °C) through 0.96 (25 °C) to 3.98 (100 °C). Collectively, these values also constitute another confirmation that the materials composition achieved using RGFC is very close to the required one: too low O content (contribution of metallic V_2O_3) would lead especially to higher low-temperature k in the visible, while too high O content (contribution of wide band gap V_2O_5) would lead especially to lower high-temperature k in the infrared). The transition temperature defined by half of the total k_{550} and k_{2000} change (n does not change monotonously) is well below 50 °C in both cases, and the transition temperature defined by the inflection point of the temperature dependence (maximum absolute value of the temperature derivative) of n_{550}, n_{2000}, k_{550} and k_{2000} is close to 50 °C in all cases.

Note that for VO_2 this kind of information (thickness-independent materials properties, not only the thickness-dependent raw data such as the transmittance) is still relatively rare in the literature. For the nevertheless available information see e.g. Refs. [11,21]. While the overall shapes of the n and k dispersion in these Refs. and in this work are consistent with each other, it is worth to mention at least two quantitative differences. First, while the local maximum of room temperature n in the visible is reported in all cases, in our case it is significantly higher and sharper. This may indicate – despite the low deposition temperature – a better crystallinity (lower volume of an amorphous phase): this kind of sharp features (van Hove singularities) is specific for crystalline materials, while amorphous materials are known to exhibit flatter dispersions. Second, the room temperature k in the visible is in our case down to 0.1 only, compared to approximately (reading from figures) 0.3 [21] –0.4 [11] (possibly due to slightly different compositions, see also the discussion in the previous paragraph).

As mentioned in Sec. 2.2, one of the optical models taken into account included the Drude oscillator as the only oscillator centered in the low-energy range (below 2.5 eV). The corresponding contribution to the total permittivity is $\varepsilon_{Drude} = -1/[\rho\varepsilon_0(\tau\omega^2 + i\omega)]$ where τ is the time between momentum loss collisions of free charge carriers and ρ is the dc rezistivity ($\rho \sim 1/N\tau$ where N is the concentration of free charge carriers). The exactness of this fit was enhanced by considering as low energies as possible (down to 0.5 eV, i.e. up to 2500 nm) in the fit. On the one hand, the assumption that the dispersion of optical constants in the low energy range is given only by the free charge carriers would certainly be an oversimplification (i.e. the resulting ρ is rather the lower bound of the true rezistivity, and this optical model was not used anywhere except in Fig. 6). On the other hand, the temperature dependence of ρ in Fig. 6 shows that in agreement with the discussion above, ρ indeed increases (N decreases; not shown) with decreasing T_m in a wide T_m range below the transition temperature.

3.4. Temperature and thickness dependence of the transmittance

In order to evaluate the application potential of the coating and to facilitate the comparison with the literature, the VO_2 optical constants (measured on Si for the non-round experimental thickness) were used to predict the transmittance of 1 mm thick float glass coated by 100 nm thick VO_2. The results are shown in complementary Figs.7 (dispersion in a wide range), 8 a (dependence on T_m at 550 and 2000 nm) and b (integral quantities T_{lum} and T_{sol} defined in Sec. 2.2). Once again, Fig. 7 shows a clear thermochromic effect – decreasing T with increasing T_m. Note that the quantitative T values and the shape of the dispersion (particularly in the low wavelength range) strongly depend on the interference. For example, the peak around 600 nm is due to the superposition of (i) low k (Fig. 4b) and (ii) constructive interference which takes place due to fulfilling the condition (neglecting k) $\lambda = 2nd$ where λ is the wavelength, n_{600} is close to 3 (Fig. 4a) and d is the aforementioned thickness of 100 nm.

Quantitatively, Fig. 8a shows that T_{550} changes from 54 to 55% ($T_m \leq$ 25 °C) to 33% (100 °C), while T_{2000} changes from 39% (T_m = -30 °C) through 30% (25 °C) to 3.4% (100 °C). The transition temperature defined by half of the total T_{2000} change (at 2000 nm the data are less affected by the interference) is just below 40 °C, and the transition temperature defined by the inflection point of the temperature dependence (maximum temperature derivative) of T_{2000} is around 45 °C (the same derivative for T_m = 40 and 50 °C). In parallel, Fig. 8b shows that T_{lum} decreases from 53 to 33%, and T_{sol} decreases from 40 to 19%.

Finally, in the above context, it is worth to mention the dependence of at least the key coating characteristics (transmittance in the visible and thermochromic modulation of transmittance in the infrared) on the coating thickness. Fig. 9a shows for T_m = 25 °C the room-temperature T_{550} of pure 1 mm thick glass substrate (89%), followed by e.g. a local T_{550} minimum (destructive interference) for a 40 nm thick coating and a local T_{550} maximum of 68% (constructive interference) for a 80 nm thick coating. The 100 nm thickness considered above constitutes an average case from this point of view. Fig. 9b shows the infrared modulation, specifically the difference between T_{2000} at T_m = 25 °C and at T_m = 100 °C. Also this quantity is thickness-dependent, with a maximum for coating thickness of 30 nm. These data facilitate the comparison of individual VO_2 coatings with each other and with the literature, as well as the choice of optimum coating thickness. The fact that the maximum infrared modulation is achieved at a similar thickness as the minimum visible transmittance is particularly important, and may lead to trade-offs depending on a specific application.

4. Conclusions

Thermochromic VO_2 coating was prepared on crystalline Si by reactive high-power impulse magnetron sputtering at a low deposition temperature 250 °C and without any substrate bias voltage, i.e. under conditions which maximize its application potential. Coating properties which can be and were achieved under these conditions were studied in a wide temperature range (–30 to

100 °C) by spectroscopic ellipsometry. The most important properties include room temperature k_{550} of 0.10 at 550 nm, and T_{2000} calculated for a 100 nm thick coating on glass of 39% at −30 °C, 30% at RT and 3.4% above the transition temperature. The transition temperature during the cooling part of the cycle for the quantities Ψ, k and calculated T is 41, <50 and <40 °C, respectively (half of the total change) or 50, 50 and 45 °C, respectively (inflection point of the temperature dependence). The hysteresis curve width at the transition temperature is 6–8 °C. The results are important for the design of thermochromic coatings, and pathways for their preparation under industry-friendly conditions, for various technological applications.

Acknowledgment

This work was supported by the project LO1506 of the Czech Ministry of Education, Youth and Sports.

References

[1] S. Hoffmann, E.S. Lee, C. Clavero, Examination of the technical potential of near-infrared switching thermochromic windows for commercial building applications, Sol. Energy Mater. Sol. Cells. 123 (2014) 65–80.
[2] C.G. Granqvist, Oxide-based chromogenic coatings and devices for energy efficient fenestration: brief survey and update on thermochromics and electrochromics, J. Vac. Sci. Technol. B 32 (2014) 060801.
[3] S. Chen, H. Ma, X. Yi, H. Wang, X. Tao, M. Chen, X. Li, C. Ke, Optical switch based on vanadium dioxide thin films, Infrared Phys. Technol. 45 (2004) 239–242.
[4] S.C. Chen, H. Ma, X. Yi, T. Xiong, H. Wang, C. Ke, Smart VO_2 thin film for protection of sensitive infrared detectors from strong laser radiation, Sens. Actuators A Phys. 115 (2004) 28–31.
[5] P. Kiria, G. Hyett, R. Binionsa, Solid state thermochromic materials, Adv. Mater. Lett. 1 (2010) 86–105.
[6] H.A. Wriedt, The O-V (Oxygen-Vanadium) system, Bull. Alloy Phase Diagr. 10 (1989) 271–277.
[7] C. Sun, L. Yan, B. Yue, H. Liu, Y. Gao, The modulation of metal–insulator transition temperature of vanadium dioxide: a density functional theory study, J. Mater. Chem. 2 (2014) 9283–9293.
[8] S.Y. Li, G.A. Niklasson, C.G. Granqvist, Thermochromic fenestration with VO_2-based materials: three challenges and how they can be met, Thin Solid Films 520 (2012) 3823–3828.
[9] N.H. Azhan, K. Su, K. Okimura, J. Sakai, Radio frequency substrate biasing effects on the insulator-metal transition behavior of reactively sputtered VO_2 films on sapphire (001), J. Appl. Phys. 117 (2015) 185307.
[10] M.J. Miller, J. Wang, Influence of grain size on transition temperature of thermochromic VO_2, J. Appl. Phys. 117 (2015) 034307.
[11] J.-P. Fortier, B. Baloukas, O. Zabeida, J.E. Klemberg-Sapieha, L. Martinu, Thermochromic VO_2 thin films deposited by HiPIMS, Sol. Energy Mater. Sol. Cells. 125 (2014) 291–296.
[12] A. Aijaz, Y.-X. Ji, J. Montero, G.A. Niklasson, C.G. Granqvist, T. Kubart, Low-temperature synthesis of thermochromic vanadium dioxide thin films by reactive high power impulse magnetron sputtering, Sol. Energy Mater. Sol. Cells 149 (2016) 137–144.
[13] S. Lee, T.L. Meyer, S. Park, T. Egami, H.N. Lee, Growth control of the oxidation state in vanadium oxide thin films, Appl. Phys. Lett. 105 (2014) 223515.
[14] J. Vlcek, J. Rezek, J. Houska, T. Kozak, J. Kohout, Benefits of the controlled reactive high-power impulse magnetron sputtering of stoichiometric ZrO_2 films, Vacuum 114 (2015) 131–141.
[15] J. Vlcek, J. Rezek, J. Houska, R. Cerstvy, R. Bugyi, Process stabilization and a significant enhancement of the deposition rate in reactive high-power impulse magnetron sputtering of ZrO_2 and Ta_2O_5 films, Surf. Coat. Technol. 236 (2013) 550–556.
[16] J. Rezek, J. Vlcek, J. Houska, R. Cerstvy, High-rate reactive high-power impulse magnetron sputtering of Ta-O-N films with tunable composition and properties, Thin Solid Films 566 (2014) 70–77.
[17] J. Vlcek, A. Belosludtsev, J. Rezek, J. Houska, J. Capek, R. Cerstvy, S. Haviar, High-rate reactive high-power impulse magnetron sputtering of hard and optically transparent HfO_2 films, Surf. Coat. Technol. 290 (2016) 58–64.
[18] Available e.g. at http://rredc.nrel.gov/solar/spectra/am1.5/, http://hyperphysics.phy-astr.gsu.edu/hbase/vision/efficacy.html.
[19] Y. Hong-Tao, F. Ke-Cheng, W. Xue-Jin, L. Chao, H. Chen-Juan, N. Yu-Xin, Effect of nonstoichiometry on Raman scattering of VO_2 films, Chin. Phys. 13 (2004) 82–84.
[20] S. Shin, S. Suga, M. Taniguchi, M. Fujisawa, H. Kanzaki, A. Fujimori, H. Daimon, Y. Ueda, K. Kosuge, S. Kachi, Vacuum-ultraviolet reflectance and photoemission study of the metal-insulator phase transitions in VO_2, V_6O_{13} and V_2O_3, Phys. Rev. B 41 (1990) 4993–5009.
[21] N.R. Mlyuka, G.A. Niklasson, C.G. Granqvist, Thermochromic multilayer films of VO_2 and TiO_2 with enhanced transmittance, Sol. Energy Mater. Sol. Cells. 93 (2009) 1685–1687.

B Controlled reactive HiPIMS—effective technique for low-temperature (300 °C) synthesis of VO_2 films with semiconductor-to-metal transition

J. Vlček, **D. Kolenatý**, J. Houška, T. Kozák, R. Čerstvý

J. Phys. D: Appl. Phys. 50 (2017) 38LT01

IOP Publishing
Journal of Physics D: Applied Physics
J. Phys. D: Appl. Phys. **50** (2017) 38LT01 (6pp)
https://doi.org/10.1088/1361-6463/aa8356

Letter

Controlled reactive HiPIMS—effective technique for low-temperature (300 °C) synthesis of VO_2 films with semiconductor-to-metal transition

J Vlček[1], D Kolenatý, J Houška, T Kozák and R Čerstvý

Department of Physics and NTIS—European Centre of Excellence, University of West Bohemia, Univerzitní 8, 306 14 Plzeň, Czechia

E-mail: vlcek@kfy.zcu.cz

Received 15 June 2017, revised 17 July 2017
Accepted for publication 1 August 2017
Published 30 August 2017

Abstract

Reactive high-power impulse magnetron sputtering with a pulsed O_2 flow control and to-substrate O_2 injection into a high-density plasma in front of the sputtered vanadium target was used for low-temperature (300 °C) deposition of VO_2 films with a pronounced semiconductor-to-metal transition onto conventional soda-lime glass substrates without any substrate bias voltage and without any interlayer. The depositions were performed using an unbalanced magnetron with a planar target of 50.8 mm diameter in argon–oxygen gas mixtures at the argon pressure of 1 Pa. The deposition-averaged target power density was close to 13 W cm^{-2} at a fixed duty cycle of 1% with a peak target power density up to 5 kW cm^{-2} during voltage pulses ranged from 40 μs to 100 μs. A high modulation of the transmittance at 2500 nm (between 51% and 8% at the film thickness of 88 nm) and the electrical resistivity (changed 350 times) at the transition temperature of 56–57 °C was achieved for the VO_2 films synthesized using 50 μs voltage pulses when the crystallization of the thermochromic VO_2(M1) phase was supported by the high-energy (up to 50 eV relative to ground potential) ions. Principles of this effective low-temperature deposition technique with a high application potential are presented.

Keywords: VO_2, HiPIMS, low deposition temperature, thermochromic films

(Some figures may appear in colour only in the online journal)

Vanadium dioxide (VO_2) is an extremely interesting and increasingly investigated coating material due to its reversible first-order transition [1] between a low-temperature monoclinic VO_2(M1) semiconductive phase (space group $P2_1/c$; distorted rutile) and a high-temperature tetragonal VO_2(R) metallic phase (space group $P4_2/mmm$; perfect rutile) relatively near room temperature (approximately 68 °C [2]). High modulation of the infrared transmittance, and electrical and thermal conductivity makes VO_2-based films a suitable candidate for numerous applications, such as electronic switches, thermal sensors and energy-saving smart windows with automatically varied solar transmission [3–5].

Owing to the worldwide interest in thermochromic VO_2, a number of pathways for its deposition by various kinds of magnetron sputtering have been recently reported [6–16]. Note that the application potential of these films depends on the ability to achieve not only the VO_2 stoichiometry but also the crystallization of the VO_2(M1) phase under as

[1] Author to whom any correspondence should be addressed.

J. Phys. D: Appl. Phys. **50** (2017) 38LT01 Letters

industry-friendly process conditions as possible. In the literature, the VO_2 crystallinity is often supported by high deposition temperatures [6, 7]. This excludes the use of many substrates not only due to their maximum working temperature, but also due to diffusion of substrate atoms (for example, sodium from the conventional soda-lime glass) into the films [8]. Other means supporting the VO_2 crystallinity (rf substrate bias voltage [9, 10, 13, 15], dc substrate bias voltage in case of a conductive substrate or a conductive interlayer on it [12], pulsed dc substrate bias voltage [14], crystalline seed interlayers on amorphous substrates [6, 13] and post-deposition annealing [8, 11]) limit the application potential as well. While in our recent work [16] we report the deposition of thermochromic VO_2 on unbiased crystalline Si at the substrate surface temperature $T_s = 250$ °C, there is no work reporting a deposition of thermochromic VO_2 onto unbiased amorphous substrates at $T_s < 400$ °C.

The present work is focused on the preparation of VO_2 films with a pronounced semiconductor-to-metal transition on conventional soda-lime glass substrates using a controlled reactive high-power impulse magnetron sputtering (HiPIMS) under exceptionally industry-friendly conditions: at low substrate surface temperature $T_s = 300$ °C, without any substrate bias voltage, and without any Na-diffusion barrier interlayer and nucleation-promoting seed interlayer.

HiPIMS is characterized by highly ionized fluxes of particles with high fractions of ionized sputtered metal atoms onto the substrate and by enhanced energies of the ions bombarding the growing films, allowing one to achieve film densification and crystallinity at low T_s and without a substrate bias voltage. However, in spite of several successful applications of reactive HiPIMS to depositions of oxide films (see, for example, [17–21], the works cited therein and the works focused on VO_2 depositions [9, 12–15]), there are still substantial problems with arcing on target surfaces during the reactive deposition processes at high target power densities (up to several kW cm^{-2}) in a pulse and with low deposition rates achieved. To avoid these problems, we have proposed a pulsed reactive gas flow control (RGFC) of the reactive HiPIMS processes [22]. This effective feedback process control makes it possible to deliver a high power into discharge pulses without arcing on the target and to maintain a sputter deposition of stoichiometric films in a region close to the metallic mode [23], allowing for a high-rate deposition of dense stoichiometric oxides [22] and oxynitrides with controlled compositions [24].

The main aim of this study is to show that the VO_2 films with the pronounced semiconductor-to-metal transition can be prepared by reactive HiPIMS with the pulsed RGFC under the aforementioned seemingly unfavorable conditions and to explain the physical principles behind this low-temperature synthesis of the VO_2 films.

The films were deposited onto a rotating substrate using an unbalanced magnetron with a planar vanadium target (diameter of 50.8 mm and thickness of 6 mm) in argon–oxygen gas mixtures at the argon pressure $p_{ar} = 1$ Pa in an ATC 2200-V AJA International Inc. sputter system. The target axis of symmetry, pointing at the center of the substrate holder at the distance $d = 145$ mm from the target, was at the angle of 35° from the axis of the substrate holder. The base pressure before depositions was below 10^{-4} Pa. The magnetron was driven by a high-power pulsed dc power supply (TruPlasma Highpulse 4002 TRUMPF Huettinger). The voltage pulse duration, t_{on}, ranged from 40 μs to 100 μs with the repetition frequency, f_r, being between 100 Hz and 250 Hz at a fixed duty cycle $t_{on}/T_p = 1\%$, where the pulse period $T_p = 1/f_r$. The deposition-averaged target power density (averaged over the total target area), $\langle S_d \rangle$, was close to 13 W cm^{-2}. The substrate was at a floating potential. The substrate surface temperature $T_s = 300$ °C was maintained during the deposition by a built-in heating system calibrated using a thermocouple directly attached to the substrate surface. The room temperature film thickness measured by ellipsometry (except for the opaque film prepared at $t_{on} = 100$ μs), see [16] for details, was 73, 88 and 85 nm for $t_{on} = 40$, 50 and 80 μs, respectively, with the corresponding deposition rate $a_D = 1.4$, 1.7 and 1.9 nm min^{-1}, respectively.

Oxygen was admitted into the vacuum chamber via mass flow controllers and two corundum conduits. Two O_2 inlets with a diameter of 1 mm were placed symmetrically above the target racetrack at the same distance of 20 mm from the target surface and oriented to the substrate [21]. The to-substrate O_2 injection in front of the target results in a substantially decreased compound fraction in the target surface layer [23], leading to reduced arcing, increased sputtering of metal atoms, and lower production of O^- ions at the target [21], and in a substantially increased compound fraction in the substrate layer due to a significantly increased chemisorption flux of O atoms onto the substrate [23]. This is caused by two to three times increased local oxygen partial pressure in front of the O_2 inlets [23] and by a very high degree of dissociation of O_2 molecules in the high-density plasma in front of the target.

The key part of the deposition procedure was the pulsed RGFC: the oxygen flow rate, Φ_{ox}, was not fixed but pulsing between $\Phi_{ox} = 0$ and 2 sccm (figure 1), and the duration of the Φ_{ox} pulses was decided during the deposition by a programmable logic controller using a pre-selected critical value of the oxygen partial pressure $(p_{ox})_{cr} = 15$ mPa. The p_{ox} was determined from the values of $p_{ar} + p_{ox}$, where $p_{ar} = 1$ Pa, measured at the chamber wall using a high-stability capacitance manometer (Baratron, type 627, MKS Instruments).

The key process parameters are t_{on} and $(p_{ox})_{cr}$. The $(p_{ox})_{cr}$ leading to a film composition close to VO_2 has to be chosen within a narrow window (±10%), identified separately for each t_{on} and each system geometry (including, for example, the actual sputter target thickness). In parallel, the deposition procedure becomes even more difficult (the aforementioned window closes from ±10% to zero) at an improper t_{on} which affects the discharge stability, and the film composition and structure. Here, it should be noted that the t_{on} value has to be sufficiently low to avoid arcing on the target surface and to ensure a sufficiently high target power density in a voltage pulse at $\langle S_d \rangle \cong 13$ W cm^{-2} which is close to an upper limit of the deposition device. The high power delivered into discharge pulses results in highly ionized fluxes of particles with high fractions of ionized sputtered V atoms onto the substrate,

J. Phys. D: Appl. Phys. **50** (2017) 38LT01 Letters

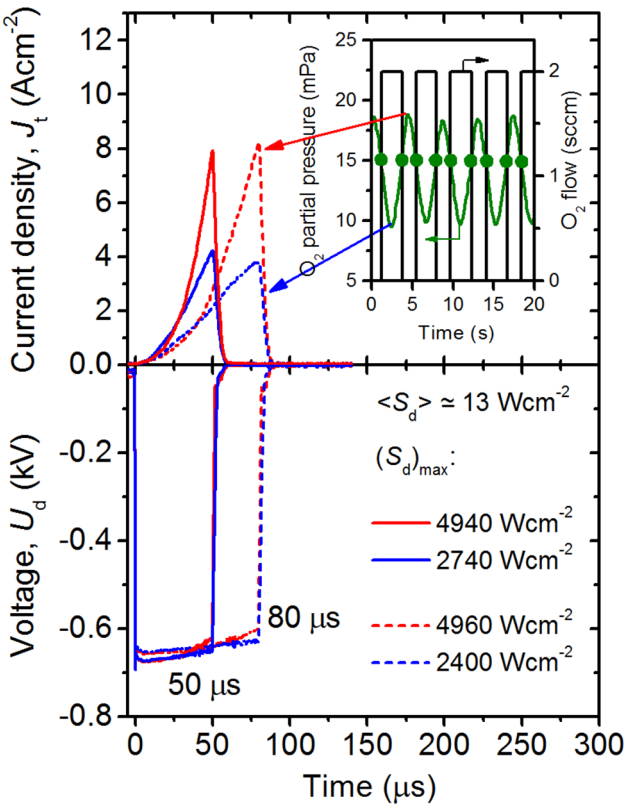

Figure 1. Waveforms of the magnetron voltage, U_d, and the target current density, J_t, for a preset deposition-averaged target power density $\langle S_d \rangle \cong 13$ W cm^{-2} at a voltage pulse duration $t_{on} = 50$ μs (solid lines) with the maximum target power densities in a pulse $(S_d)_{max} = 2740$ W cm^{-2} and 4940 W cm^{-2} related to the minimum and maximum values of the oxygen partial pressure, p_{ox}, respectively, and at a voltage pulse duration $t_{on} = 80$ μs (dashed lines) with the corresponding values $(S_d)_{max} = 2400$ W cm^{-2} and 4960 W cm^{-2} during a deposition of VO_2 films. Time evolution of p_{ox} during the deposition at $t_{on} = 80$ μs is shown in the inset. A preselected critical value $(p_{ox})_{cr} = 15$ mPa determining the switching-on and switching-off of the oxygen flow rate $\Phi_{ox} = 2$ sccm is marked by dots.

in enhanced energies of the ions bombarding the growing films and in a significantly increased chemisorption flux of O atoms onto the substrate.

The time-averaged energy distributions of positive ions incident upon a central region of the substrate holder were measured with an energy-resolved mass spectrometer (EQP300 Hiden Analytical) placed at the substrate position. Assuming the same characteristics for the transmission of all the positive ionic species through the instrument and its energy-independent acceptance cone, the composition of the total flux of positive ions onto the substrate was calculated using the particular integral ion fluxes determined. The flux of negative ions onto the substrate was under the spectrometer detection limit.

For structural investigation of the films, x-ray diffraction (XRD) measurements were carried out using a PANalytical X′Pert PRO diffractometer working with a CuKα (40 kV, 40 mA) radiation at a glancing incidence of 1°. The residual macrostress, σ, was estimated using the Stoney's formula and the bending of Si stripes (used in parallel to glass substrates)

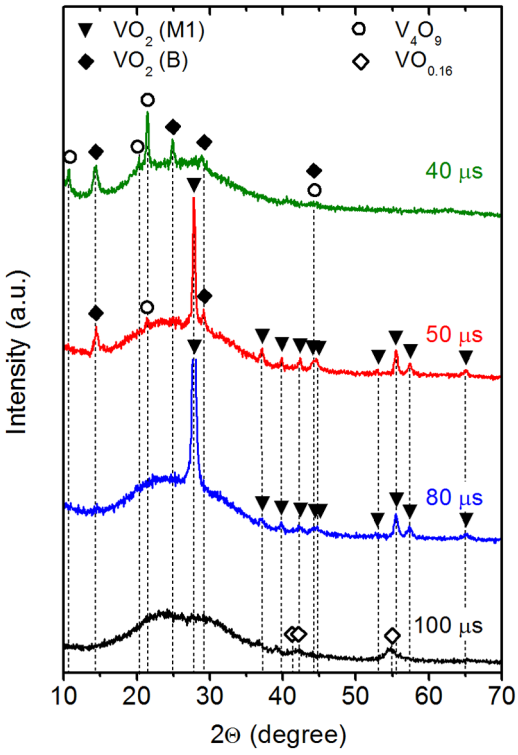

Figure 2. X-ray diffraction patterns taken from the VO_x films prepared at various voltage pulse durations. The main diffraction peaks of VO_2(M1), VO_2(B), V_4O_9 and $VO_{0.16}$ are marked.

measured by profilometry (Dektak 8 Stylus Profiler, Veeco). The temperature dependence of the electrical resistivity, ρ, and the optical transmittance at 2500 nm, T_{2500}, were measured in the range of the sample temperatures, T_m, from 25 °C to 100 °C using a four-point probe system (Jandel MACOR Probe Head) and a spectrophotometer (Agilent Cary 7000) with a custom-designed heat cell, respectively.

Figure 1 shows the time evolution of the magnetron voltage, $U_d(t)$, and the target current density, $J_t(t)$, related to the minimum and maximum values of p_{ox} during a deposition of the thermochromic VO_2 films (figures 2 and 3) at $t_{on} = 50$ μs and 80 μs. Figure 1 shows the range of the waveforms of $U_d(t)$ and $J_t(t)$ during the controlled depositions of the VO_2 films with the maximum target power densities of up to 5 kW cm^{-2} in a pulse. The quicker rise in J_t at a higher (by up to 20 V) $|U_d|$ for $t_{on} = 50$ μs with the pulse-off time of 4.95 ms than for $t_{on} = 80$ μs with the pulse-off time of 7.92 ms at the same $t_{on}/T_p = 1\%$ is caused by a higher plasma density in front of the target at the beginning of the pulse for $t_{on} = 50$ μs. In spite of the quicker rise in J_t, the fraction of the pulse with intense target sputtering is slightly shorter at $t_{on} = 50$ μs than that at $t_{on} = 80$ μs. This is in agreement with a slightly lower $a_D = 1.7$ nm min^{-1} achieved at $t_{on} = 50$ μs than $a_D = 1.9$ nm min^{-1} achieved at $t_{on} = 80$ μs, and with the higher $p_{ox} =$ 10–19 mPa during the deposition at $t_{on} = 50$ μs (table 1) than $p_{ox} = 9$–18 mPa during the deposition at $t_{on} = 80$ μs (figure 1 and table 1) for the same $(p_{ox})_{cr} = 15$ mPa. Moreover, the shorter fraction of the pulse with the intense target sputtering at a higher mean value of p_{ox} during the controlled oscillations at $t_{on} = 50$ μs can result (and did result, see figure 2) in

J. Phys. D: Appl. Phys. **50** (2017) 38LT01 Letters

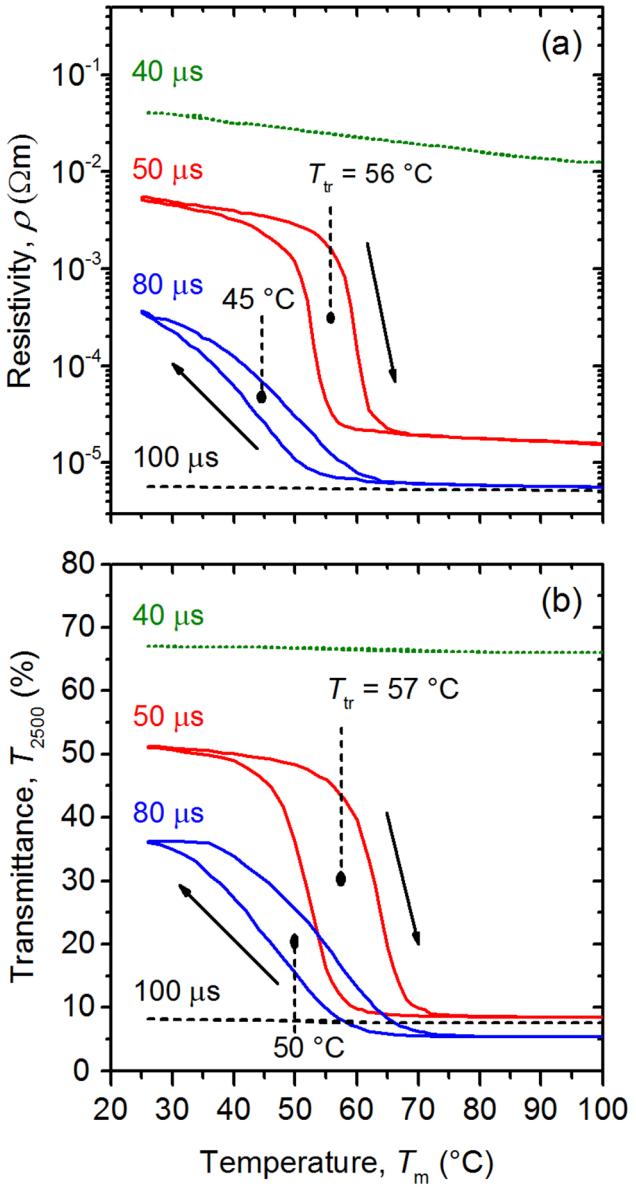

Figure 3. Temperature (T_m) dependence of the electrical resistivity (a) and the transmittance at 2500 nm (b) for the VO_x films prepared at various voltage pulse durations. The transition temperatures, T_{tr}, are also given.

a lower V content in the films due to a slightly higher target coverage by a V oxide [23].

Figure 2 shows the XRD patterns at four different t_{on} values from 40 μs to 100 μs. The overall trend given by the four phase compositions confirms the observation discussed in the previous paragraph: decreasing O content in the films with increasing t_{on}. First, the film prepared at the shortest $t_{on} = 40$ μs exhibits a mixture of the phases V_4O_9 (PDF#04-017-0339 [25]) and VO_2(B) (PDF#01-084-3056), indicating a [O]:[V] compositional ratio well above 2 (result obtained at any $(p_{ox})_{cr}$, not only 15 mPa). A case can be made that while the non-thermochromic phase VO_2(B) is less stable than the thermochromic phase VO_2(M1) for the exact stoichiometric composition, it is more prone to form under O-rich conditions, for example, due to its stabilization by metal vacancies. Second, the phase composition of the film prepared at longer $t_{on} = 50$ μs is dominated by the thermochromic phase VO_2(M1) (PDF#04-003-2035). Thus, this film can be referred to as VO_2. However, small peaks corresponding to the phases V_4O_9 and VO_2(B) are still visible, indicating [O]:[V] slightly above 2. Third, the film prepared at even longer $t_{on} = 80$ μs exhibits only the thermochromic phase VO_2(M1), indicating the desired [O]:[V] close to 2. Fourth, the film prepared at the longest $t_{on} = 100$ μs exhibits only the phase $VO_{0.16}$ (PDF#04-020-6075), indicating [O]:[V] well below 2.

Figure 3 examines the semiconductor-to-metal transition of the aforementioned four films in terms of ρ and T_{2500} between 25 °C and 100 °C. First, the film prepared at $t_{on} = 40$ μs ([O]:[V] > 2) is semiconductive and well transparent in the whole measurement range. Second, the film prepared at $t_{on} = 50$ μs ([O]:[V] slightly above 2) exhibits a strong thermochromic effect: ρ changes 350 times between 5.3×10^{-3} Ωm and 1.5×10^{-5} Ωm and T_{2500} changes between 51% and 8%, with a transition temperature, T_{tr}, of 56–57 °C. The transmittance of this 88 nm thick film in the visible region, which will be investigated in detail in a separate paper, was up to 38% at the wavelength of 625 nm for $T_m = 25$ °C and up to 34% at the wavelength of 640 nm for $T_m = 90$ °C (not shown). Third, the film prepared at $t_{on} = 80$ μs ([O]:[V] of around 2) exhibits a relatively weaker thermochromic effect: ρ changes 64 times between 3.6×10^{-4} Ωm and 5.6×10^{-6} Ωm and T_{2500} changes between 36% and 5%, with T_{tr} of 45-50 °C. The stronger thermochromic effect at $t_{on} = 50$ μs compared to $t_{on} = 80$ μs, despite the slightly worse stoichiometry, can be explained by a better crystallinity of the former film. The VO_2(M1) XRD peak widths (figure 2) indicate a size of coherently diffracting regions of around 73 nm and 29 nm at $t_{on} = 50$ μs and 80 μs, respectively. However, a very strong thermochromic effect was obtained [16] for VO_2 deposited at $t_{on} = 80$ μs on Si: crystalline substrates support the VO_2 crystallinity in a wider t_{on} range, allowing one to fully utilize the desired [O]:[V] = 2. The transition temperatures are consistent with the crystallinity as well: the film prepared at $t_{on} = 50$ μs exhibits not only a larger size of coherently diffracting regions, but also T_{tr} closer to the reported bulk value of 68 °C [2]. On the other hand, the film stress, which can also contribute to decreasing the transition temperature (see e.g. the discussion in [9]), was about the same at $t_{on} = 50$ and 80 μs ($\sigma = -1.2$, -1.3, -1.5 and -0.3 GPa for $t_{on} = 40$, 50, 80 and 100 μs, respectively). Fourth, the film prepared at $t_{on} = 100$ μs ([O]:[V] < 2) is metallic and opaque in the whole measurement range.

In spite of the aforementioned simplifying assumptions applied to the mass spectroscopy measurements, the normalized time-averaged energy distribution functions of dominant positive ions (figure 4) and the compositions of the total fluxes of the positive ions (table 1) at the substrate position provide valuable information contributing to the explanation of the different structure of the VO_2 films prepared at $t_{on} = 50$ μs and $t_{on} = 80$ μs. The lower $(V^+ + V^{2+})$ ion fraction in the total ion flux for $t_{on} = 50$ μs at almost the same $(2O_2^+ + O^+)$ ion fraction as for $t_{on} = 80$ μs (table 1) correlates with the lower V content in the films produced at $t_{on} = 50$ μs.

J. Phys. D: Appl. Phys. **50** (2017) 38LT01 Letters

Table 1. Discharge characteristics and compositions of the total fluxes of positive ions at the substrate position during the depositions of VO_2 films with $t_{on} = 50$ μs and $t_{on} = 80$ μs (figure 1).

Discharge characteristics			Composition of total ion flux						
t_{on} (μs)	p_{ox} (mPa)	$(S_d)_{max}$ (kW cm^{-2})	V^+	V^{2+}	VO^+	O_2^+ (%)	O^+	Ar^+	Ar^{2+}
50	10–19	2.74–4.94	6	2	<1	10	14	66	1
80	9–18	2.40–4.96	9	3	<1	9	15	63	<1

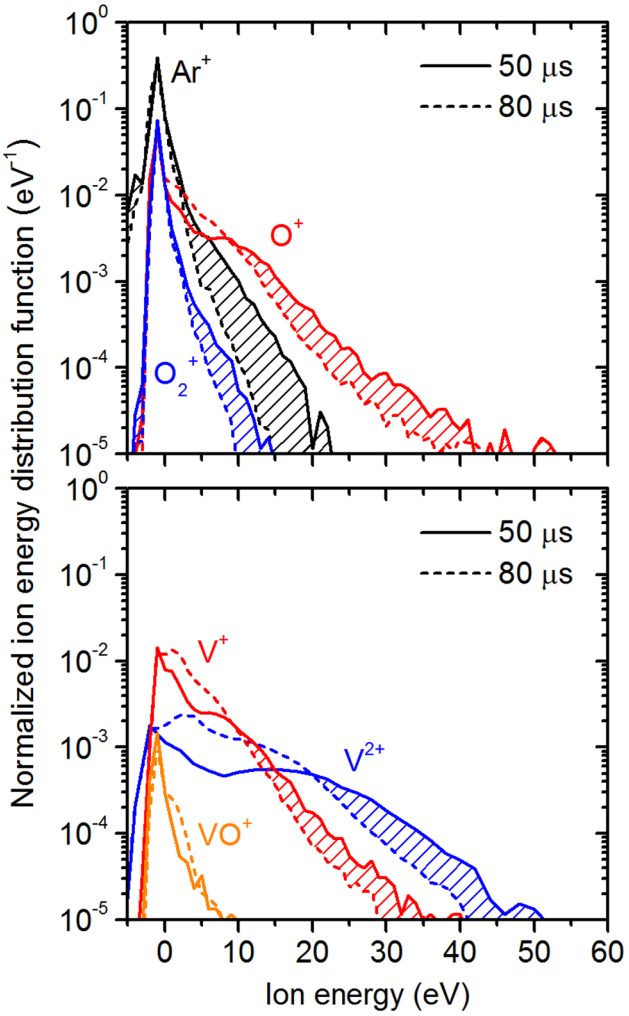

Figure 4. Normalized time-averaged energy distribution functions of dominant positive ions at the substrate position measured for the voltage pulse durations $t_{on} = 50$ μs and $t_{on} = 80$ μs (figure 1). The hatched areas denote the high-energy parts of the ion energy distributions with higher fractions of the ions produced at $t_{on} = 50$ μs compared with $t_{on} = 80$ μs.

Much higher fractions of the high-energy (up to 50 eV relative to ground potential) ions at $t_{on} = 50$ μs, caused mainly by the higher $|U_d|$, support the crystallization of the thermochromic phase (VO_2(R) during the deposition at $T_s > T_{tr}$, VO_2(M1) at the room temperature—figure 2). Recently, the importance of the high-energy particles for the crystallinity of films has been pointed out for ZrO_2 [26].

Reproducibility of the best results achieved at $t_{on} = 50$ μs decreases with erosion of the sputter target (lower U_d at the same $\langle S_d \rangle$) and a decreasing T_s. For a new target and the very low $T_s = 300$ °C, the film properties are the same for about 75% of successive depositions.

In conclusion, we have shown that VO_2 films with pronounced semiconductor-to-metal transition can be prepared on conventional soda-lime glass substrates using the controlled reactive HiPIMS with the to-substrate O_2 injection into the high-density plasma in front of the sputtered V target under exceptionally industry-friendly conditions: at low substrate surface temperature $T_s = 300$ °C, without any substrate bias voltage and without any interlayer. The high-quality VO_2 films were synthesized at the deposition-averaged target power density close to 13 W cm^{-2} with a peak target power density up to 5 kW cm^{-2} during 50 μs voltage pulses at the duty cycle of 1% when the crystallization of the thermochromic phase was supported by the high-energy (up to 50 eV relative to ground potential) ions.

Acknowledgments

This work was supported by the Czech Science Foundation under Project No. 17-08944S.

References

[1] Morin F J 1959 *Phys. Rev. Lett.* **3** 34
[2] Wriedt H A 1989 *Bull. Alloy Phase Diagr.* **10** 271
[3] Tomczak J M and Biermann S 2009 *Phys. Status Solidi* b **246** 1996
[4] Granqvist C G 2016 *Thin Solid Films* **614** 90
[5] Wang S, Liu M, Kong L, Long Y, Jiang X and Yu A 2016 *Prog. Mater. Sci.* **81** 1
[6] Kakiuchida H, Jin P, Nakao S and Tazawa M 2007 *Japan. J. Appl. Phys.* **46** L113
[7] Mlyuka N R, Niklasson G A and Granqvist C G 2009 *Phys. Status Solidi* a **206** 2155
[8] Koo H, You H W, Ko K E, Kwon O J, Chang S H and Park C 2013 *Appl. Surf. Sci.* **277** 237
[9] Fortier J P, Baloukas B, Zabeida O, Klemberg-Sapieha J E and Martinu L 2014 *Sol. Energy Mater. Sol. Cells* **125** 291
[10] Azhan N H, Su K, Okimura K and Sakai J 2015 *J. Appl. Phys.* **117** 185307
[11] Miller M J and Wang J 2015 *J. Appl. Phys.* **117** 034307
[12] Aijaz A, Ji Y X, Montero J, Niklasson G A, Granqvist C G and Kubart T 2016 *Sol. Energy Mater. Sol. Cells* **149** 137
[13] Loquai S, Baloukas B, Zabeida O, Klemberg-Sapieha J E and Martinu L 2016 *Sol. Energy Mater. Sol. Cells* **155** 60
[14] Lin T, Wang L, Wang X, Zhang Y and Yu Y 2016 *Surf. Coat. Technol.* **305** 110
[15] Loquai S, Baloukas B, Klemberg-Sapieha J E and Martinu L 2017 *Sol. Energy Mater. Sol. Cells* **160** 217
[16] Houska J, Kolenaty D, Rezek J and Vlcek J 2017 *Appl. Surf. Sci.* (https://doi.org/10.1016/j.apsusc.2016.10.084) at press

J. Phys. D: Appl. Phys. **50** (2017) 38LT01 Letters

[17] Anders A 2017 *J. Appl. Phys.* **121** 171101
[18] Sarakinos K, Alami J and Konstantinidis S 2010 *Surf. Coat. Technol.* **204** 1661
[19] Lundin D and Sarakinos K 2012 *J. Mater. Res.* **27** 780
[20] Hála M, Čapek J, Zabeida O, Klemberg-Sapieha J E and Martinů L 2012 *J. Phys. D: Appl. Phys.* **45** 055204
[21] Vlček J, Rezek J, Houška J, Kozák T and Kohout J 2015 *Vacuum* **114** 131
[22] Vlček J, Rezek J, Houška J, Čerstvý R and Bugyi R 2013 *Surf. Coat. Technol.* **236** 550
[23] Kozák T and Vlček J 2016 *J. Phys. D: Appl. Phys.* **49** 055202
[24] Belosludtsev A, Houška J, Vlček J, Haviar S, Čerstvý R, Rezek J and Kettner M 2017 *Ceram. Int.* **43** 5661
[25] JCPDS-ICDD 2015 *PDF-4 + Database* (Newton Square, PA: International Centre for Diffraction Data)
[26] Houska J 2016 *Surf. Coat. Technol.* **304** 23

C Properties of thermochromic VO_2 films prepared by HiPIMS onto unbiased amorphous glass substrates at a low temperature of 300 °C

J. Houska, **D. Kolenaty**, J. Vlcek, R. Cerstvy

Thin Solid Films 660 (2018) 463–470

Thin Solid Films 660 (2018) 463–470

Contents lists available at ScienceDirect

Thin Solid Films

journal homepage: www.elsevier.com/locate/tsf

Properties of thermochromic VO_2 films prepared by HiPIMS onto unbiased amorphous glass substrates at a low temperature of 300 °C

J. Houska*, D. Kolenaty, J. Vlcek, R. Cerstvy

Department of Physics and NTIS - European Centre of Excellence, University of West Bohemia, Univerzitni 8, 30614 Plzen, Czech Republic

ARTICLE INFO

Keywords:
Vanadium dioxide
High-power impulse magnetron sputtering
Thermochromic coatings
Low deposition temperature
Industry-friendly deposition technique
Optical properties

ABSTRACT

The paper deals with thermochromic VO_2 films deposited by reactive high-power impulse magnetron sputtering with a pulsed reactive gas flow control under exceptionally industry-friendly conditions: onto amorphous glass substrates without any interlayer, without any substrate bias voltage and at low temperatures (T_{dep}) down to 300 °C. We show that (and how) strongly thermochromic VO_2 films can be prepared even under these unfavorable conditions, and compare their properties with those achieved under more favorable but less industry-friendly conditions. We focus on the film structure studied by X-ray diffraction and Raman spectroscopy, electrical resistivity, and especially optical properties studied by spectroscopic ellipsometry and spectrophotometry. The properties achieved at T_{dep} = 300 °C include e.g. transition temperature (T_{tr}) below 60 °C, extinction coefficient at 550 nm of around 0.50, modulation of the extinction coefficient at 2000 nm between 0.35 (room temperature) and 3.77 (above T_{tr}) or modulation of the resistivity between 5.3×10^{-3} Ωm (room temperature) and 1.5×10^{-5} m (above T_{tr}). The results are important for the design of pathways for the preparation of thermochromic coatings under industry-friendly conditions, and, in turn, significantly increase the application potential of these coatings.

1. Introduction

Thermochromic materials exhibit temperature-dependent changes of their electronic structure, leading to temperature-dependent changes of the optical properties (infrared transmittance in the first place), the electrical conductivity or (the electronic part of) the thermal conductivity. This leads to numerous applications, including - probably in the first place - reducing the energy consumption by controlling the heat fluxes through “smart” windows [1, 2]. Applications in the fields of optical switches, smart radiators or protection of sensitive infrared detectors from a strong laser radiation are of interest as well [3, 4]. The subject of this work is VO_2, material which has attracted a worldwide attention [5–19] due to its reversible first-order thermochromic transition between a low-temperature monoclinic VO_2(M1) semiconductive phase (space group $P2_1/c$; distorted rutile) and a high-temperature tetragonal VO_2(R) metallic phase (space group $P4_2/mmm$; perfect rutile) [20–22]. The reported temperature of this transition is 68 °C for bulk VO_2 [21] and typically well below 68 °C (e.g. close to 50 °C [5]) for thin film VO_2, and can be further decreased towards the room temperature (RT) by doping by other metals such as Mo, W or Nb [18, 19]. This makes VO_2 a very promising material for thermochromic coatings.

Magnetron sputtering constitutes an important technique for preparation of functional coatings. Owing to the worldwide interest in thermochromic VO_2, number of pathways for its deposition by various kinds of magnetron sputtering have been reported in recent years [5–17]. Related issues, ranging from increasing the environmental stability of the coatings by a SiN_x overlayer on the top of VO_2 [9] to studying the changes of VO_2 optical properties down to −30 °C [5], have been addressed as well. The efforts to prepare VO_2-based thermochromic coatings deal with the following two main challenges. The first one is to achieve the correct film composition, avoiding the formation of O-poor (e.g. V_2O_3) or O-rich (e.g. V_4O_9 or V_2O_5) phases. The other one is to achieve the crystallinity of VO_2 films. The overall impression given by the literature is that the VO_2 crystallinity is typically supported by means which actually limit its application potential: (i) high deposition temperature (T_{dep}) [10, 12], (ii) substrates which exhibit at high T_{dep} a weaker effect of a diffusion of their atoms into the coatings than soda-lime glass (e.g. B270 glass [7–9]), (iii) substrate bias voltage [7–9, 11, 13, 14] (rf or dc, the latter is simpler in itself but requires a conductive substrate or a conductive interlayer on it [11]), (iv) crystalline seed layers on amorphous substrates [8, 12] and/or (v) post-deposition annealing [15, 16]. For example, until recently there has been no work reporting a deposition of thermochromic VO_2 onto unbiased substrates at T_{dep} < 400 °C. Exceptions include the recent

* Corresponding author.
E-mail address: jhouska@kfy.zcu.cz (J. Houska).

https://doi.org/10.1016/j.tsf.2018.06.057
Received 13 March 2018; Received in revised form 18 June 2018; Accepted 28 June 2018
Available online 30 June 2018

complementary efforts to utilize rf-superimposed dc magnetron sputtering (T_{dep} = 300 °C on amorphous glass [17]) and high-power impulse magnetron sputtering (HiPIMS) with a reactive gas flow control (RGFC, see Sec. 2.1) (T_{dep} = 300 °C on amorphous glass [6] and 250 °C on crystalline Si [5]).

However, while the aforementioned papers [6] (our recent letter) and [17] describe the deposition procedure in itself, there is a knowledge gap resulting from at least the following two facts. First, some important properties, thickness-independent optical constants in the first place (in the case of Ref. [17] also resistivity), are not reported at all. Second, the best properties obtained on glass substrates at T_{dep} = 300 °C which are reported are not compared with those obtained at T_{dep} > 300 °C using the same deposition parameters such as sputtering powers and (in the case of transmittance) about the same thickness. The main aim of this work is to demonstrate that the film properties (including the thickness-independent optical constants) obtained using HiPIMS with RGFC on soda-lime glass substrates without any substrate bias and without any interlayer at T_{dep} = 300 °C and T_{dep} > 300 °C are fully comparable. In other words, the aim is to show that the advantages of this technique indeed allow one to make the deposition process exceptionally industry-friendly without any concessions in terms of film properties (let alone the possibility to further decrease T_{dep} by combining the advantages of HiPIMS with RGFC with those of substrate bias and/or crystalline interlayer). In order to fulfill this aim we build on the recent letter [6] where we investigated a wide range of sputtering conditions, and identified the optimum conditions allowing a deposition of thermochromic VO_2 at T_{dep} = 300 °C. In this work we provide a detailed analysis of the structure and a wide range of properties of films prepared under the optimum conditions (Sec. 2.2), and compare the properties achieved at T_{dep} = 300 °C (i) with those achieved by us at enhanced T_{dep} = 400 °C, as well as (ii) with the literature.

2. Methodology

2.1. Film deposition

The films were deposited on 1 mm thick soda-lime glass by reactive HiPIMS (ATC 2200-V AJA International Inc. system with a TruPlasma Highpulse 4002 Hüttinger Elektronik power supply) of V target (50.8 mm in diameter) in Ar + O_2 plasma. Pre-deposition substrate cleaning in rf discharge (50 W for 5 min) has been performed. The film thickness (h; Table 1) was around 80 nm at a deposition rate of around 1.8 nm/min. The target to substrate distance was 145 mm and the substrates were at a floating potential. The substrate surface temperature during the depositions (T_{dep}) was 300 or 400 °C and it was maintained by a built-in heating system calibrated using a thermocouple directly attached to the substrate surface. The duty cycle of the voltage pulses was 1% and the voltage pulse duration (t_{on}) was 50 μs (frequency 200 Hz) or 80 μs (frequency 125 Hz). The deposition-averaged power density was around 13 Wcm^{-2}, the pulse-averaged power density was around 1.3 $kWcm^{-2}$ and the peak power density was 5 $kWcm^{-2}$. The base pressure was < 10^{-4} Pa. The Ar partial pressure was 1 Pa at a fixed Ar flow rate of 60 sccm, and the O_2 partial pressure was oscillating between 10 and 20 mPa (see the next paragraph).

The key part of our deposition procedure is the reactive gas flow control (RGFC) [23]. The O_2 flow rate was not fixed but pulsing between 0 and 2 sccm, and the duration of the O_2 flow pulses was decided during the depositions by a programmable logic controller using a preselected critical value (p_{ox_crit} = 15 mPa) of the O_2 partial pressure (p_{ox}). Previously the combination of HiPIMS with RGFC allowed us to design pathways for high-rate deposition of stoichiometric oxides (ZrO_2 [23–25], Ta_2O_5 [23], HfO_2 [26]) and oxynitrides (Ta-O-N [27], Hf-O-N [28]), based on oscillating in the transition mode with a low compound fraction on the target surface. The present case is even more complex, because the deposition procedure has to guarantee (i) the defined O-poor film stoichiometry (subsaturated VO_2 rather than saturated V_2O_5) and (ii) film crystallinity despite the low T_{dep}, amorphous substrates and no substrate bias. The desired VO_2 stoichiometry was achieved by RGFC, i.e. by p_{ox} oscillations around an optimum value given by p_{ox_crit}. The VO_2 crystallization was supported by the energy delivered into the growing films by highly ionized fluxes of energetic particles with many metal ions, resulting from the aforementioned high sputtering powers up to 5 $kWcm^{-2}$. The possibility of target oxidation (which would make using such high powers impossible) was suppressed not only by RGFC in itself, but also by the (i) O_2 inlet orientation towards the substrate and (ii) O_2 inlet location in the dense plasma in front of the target (which increases the degree of dissociation and subsequently the reactivity of oxygen, allowing one to achieve the desired VO_2 stoichiometry at a very low p_{ox_crit}).

2.2. List of films prepared and their reproducibility

There are four films studied in detail in this work, characterized by two varied deposition parameters: T_{dep} = 300 or 400 °C and t_{on} = 50 or 80 μs. T_{dep} = 300 °C is the lowered deposition temperature which constitutes, together with using unbiased substrates, a crucial part of our motivation (Sec. 1). T_{dep} = 400 °C is used for comparative purposes.

The pulse lengths t_{on} = 50–80 μs constitute the range of proper values leading, at p_{ox_crit} = 15 mPa, to compositions close to VO_2. In short, p_{ox_crit} has to be chosen within a narrow window (approximately ± 10% at an ideal t_{on}). At an improper t_{on} (which affects the oxide fraction on the sputtered target and the energetic bombardment of the growing films) the aforementioned window closes from ± 10% to zero. Below we show that the shorter value t_{on} = 50 μs is the only one leading (in parallel to the correct composition) to the same crystallinity and performance of films prepared at T_{dep} = 300 and 400 °C. The longer value t_{on} = 80 μs is considered in order to demonstrate that the film performance in the aforementioned T_{dep} range is not temperature-independent automatically but only at the proper (short) t_{on}.

Reproducibility of the best results achieved at t_{on} = 50 μs decreases with erosion of the sputter target (leading to a lower magnetron voltage at the same deposition-averaged power density) and with decreasing T_s. For a new target and the very low T_s = 300 °C, the film properties are the same for about 75% of successive depositions.

2.3. Film characterization

The room-temperature film structure was studied by X-ray diffraction (XRD) and Raman spectroscopy. The XRD patterns were obtained using the PANalytical X'Pert PRO instrument (Bragg-Brentano geometry; CuKα radiation), over the 2θ-range from 8 to 108°. The approximate size of coherently diffracting domains of the phase VO_2(M1) was estimated from the full width at half maximum (FWHM) of its main peak using the Scherrer formula. The instrument effect on FWHM was estimated using a powder standard LaB_6. The Raman spectra were obtained using the Horiba Jobin Yvon LABRAM HR Evolution instrument (532 nm laser), over the frequency range from 100 to 1000 cm^{-1}. The signal from the glass substrate was subtracted in order to get zero minimum values of the resulting spectra. Let us emphasize that while (the possible artifacts resulting from) the substrate fluorescence could be completely avoided by measuring the Raman spectra not on the truly investigated substrate but on Si (approach used e.g. in Ref. [8]), the aim of this paper requires the opposite.

The optical properties of the films were studied by spectrophotometry and spectroscopic ellipsometry. Both these measurements were performed at the measurement temperature (T_m) between 25 °C (below the transition temperature, T_{tr}) and 100 °C (well above T_{tr}). The spectrophotometric measurements were performed using the Agilent CARY 7000 instrument equipped by an in-house made heat stage, over the wavelength (λ) range from 300 to 2500 nm, at the normal angle of incidence in transmission. The ellipsometric measurements were

Table 1
Parts a-c show characteristics of the four VO_2 films studied. Columns 1–4 show the deposition temperature (T_{dep}), the pulse length (t_{on}), the film thickness (h) and the measurement temperature (T_m), respectively.

T_{dep} (°C)	t_{on} (μs)	h (nm)	T_m (°C)						
(a)				n_{550} (−)	n_{2000} (−)	k_{550} (−)	k_{2000} (−)	ρ (m)	ρ(25 °C)/ρ(100 °C) (−)
400	50	80	25	3.19	3.29	0.44	0.24	3.9×10^{-3}	360
			100	2.77	2.72	0.56	4.24	1.1×10^{-5}	
400	80	77	25	3.20	3.33	0.48	0.38	9.3×10^{-4}	220
			100	2.69	2.55	0.61	4.69	4.1×10^{-6}	
300	50	88	25	3.06	3.24	0.48	0.35	5.3×10^{-3}	350
			100	2.68	3.02	0.51	3.77	1.5×10^{-5}	
300	80	85	25	3.05	3.15	0.51	0.77	3.6×10^{-4}	65
			100	2.71	2.76	0.54	4.03	5.6×10^{-6}	
(b)				T_{lum} (−)	T_{sol} (−)	T_{550} (−)	T_{2000} (−)	T_{2500} (−)	T_{2500}(25 °C) - T_{2500}(100 °C) (−)
400	50	80	25	0.31	0.26	0.32	0.49	0.58	0.52
			100	0.27	0.21	0.28	0.07	0.06	
400	80	77	25	0.30	0.25	0.31	0.44	0.50 ± 0.01	0.44
			100	0.27	0.20	0.28	0.07	0.06 ± 0.01	
300	50	88	25	0.32	0.26	0.32	0.45	0.52 ± 0.01	0.46
			100	0.29	0.22	0.30	0.08	0.08	
300	80	85	25	0.30	0.24	0.30	0.34	0.37 ± 0.01	0.32
			100	0.27	0.21	0.28	0.07	0.05 ± 0.01	
(c)		T_{tr} (°C) according to:		half logρ	max. |logρ'|	half T_{2500}	max. |T_{2500}'|	half Ψ_{2000}	max. |Ψ_{2000}'|
400	50			58	59	60	60	64	63
400	80			51	51	50	52	61	60
300	50			56	56	57	59	64	63
300	80			45	49	50	51	56	54
(d)				n_{550} (−)	n_{2000} (−)	k_{550} (−)	k_{2000} (−)	note	
[5] 250 °C, no bias, on Si				3.20	2.87	0.10	0.96	25 °C (k_{2000} = 0.43 at −30 °C)	
[this work]: 300 °C, no bias, on glass				3.06	3.24	0.48	0.35	25 °C, part a of this table	
[7] 300 °C, RF bias, on B270 glass				2.9	2.8	0.5	0.2	30 °C, reading from Figs.	
[8] 350 °C, RF bias, on Si + TiO_2 seed				3.1		0.3		20 °C, reading from Figs.	
[9] 350 °C, RF bias, on B270 glass				3.20		0.48		20 °C, HiPIMS data in text	
[10] 450 °C, no bias, on glass				2.8	3.0	0.4	0.3	22 °C, reading from Figs.	
[12] 600 °C, no bias, on Si + TiO_2 seed				3.0		0.45		23 °C, reading from Figs.	

Columns 5–10 of part a show the refractive indices at the wavelength of 550 nm (n_{550}) and 2000 nm (n_{2000}), the extinction coefficients at the same wavelengths (k_{550} and k_{2000}), the electrical resistivity (ρ), and the ratio of ρ values at 25 and 100 °C, respectively.
Columns 5–10 of part b show the integral transmittances T_{lum} (Eq. 1) and T_{sol} (Eq. 2), transmittance at the wavelength of 550 nm (T_{550}), 2000 nm (T_{2000}) and 2500 nm (T_{2500}), and the difference of T_{2500} values at 25 and 100 °C, respectively. All these quantities are valid (only) for the thicknesses shown in column 3. T_{2500} includes the horizontal non-uniformity of ± 1% which was observed in some cases.
Columns 5–10 of part c show the transition temperature (T_{tr}; averaged over heating and cooling) according to (i) half of the change between T_m = 25 and 100 °C and (ii) the maximum first derivative of logρ (Fig. 3), T_{2500} (Fig. 4) and Ψ_{2000}. Note that the change defined by half of ρ (instead of half of logρ) takes place at even lower T_{tr} (from the top of the table at 51, 40, 48 and 35 °C instead of 58, 51, 56 and 45 °C, respectively).
Part d compares the low-temperature values of n_{550}, n_{2000}, k_{550} and k_{2000} reported for various T_{dep} values, substrates and substrate biasing in this work (information for T_{dep} = 300 °C and t_{on} = 50 μs, repeated from part a for reader's convenience), in our previous work [5] and in Refs. [7–10, 12] (i.e. those Refs. which include these data, not only the thickness-dependent transmittance).

performed using the J.A. Woollam Co. Inc. VASE instrument equipped by an Instec heat stage with the Instec STC200 controller, at the angles of incidence of 55, 60 and 65° in reflection. The heating/cooling rate during the ellipsometric measurements was 3°/min.

In Sec. 3 we show and discuss (i) the measured ellipsometric data, i.e. the angles Ψ and Δ ($r_p/r_s = \tan\Psi . e^{i\Delta}$ where r_p and r_s is the reflectivity of p- and s-polarized light, respectively), (ii) dispersion of the refractive index (n) and the extinction coefficient (k) calculated from the ellipsometric data, (iii) dispersion of the transmittance (T) calculated from the ellipsometric results, (iv) dispersion of T measured by spectrophotometry, (v) n, k and T at specific wavelengths such as 2000 nm (n_{2000}, k_{2000} and T_{2000}, respectively), and (vi) integral quantities T_{lum} and T_{sol} defined by Eqs. 1 and 2

$$T_{lum} = \int_{380}^{780} \phi_{lum}(\lambda)\phi_{sol}(\lambda)T(\lambda, T_m)d\lambda / \int_{380}^{780} \phi_{lum}(\lambda)\phi_{sol}(\lambda)d\lambda \quad (1)$$

$$T_{sol} = \int_{300}^{2500} \phi_{sol}(\lambda)T(\lambda, T_m)d\lambda / \int_{300}^{2500} \phi_{sol}(\lambda)d\lambda \quad (2)$$

where φ_{um} is the luminous sensitivity of the human eye and φ_{sol} is the solar irradiance spectrum at the sea level [29]. The optical data were fitted using the WVASE software and an optical model consisting of a glass substrate, a bulk VO_2 layer and a surface roughness layer (typically around 10 nm). The semiconductive VO_2 below T_{tr} was represented by a combination of the Cody-Lorentz dispersion formula (oscillator) with three Lorentz oscillators centered in very near IR, visible and in visible or UV (e.g. at 1.34, 2.48 and 3.61 eV, respectively, for T_{dep} = 300 °C and t_{on} = 50 μs). The model follows a preference of the fit quality over the number of oscillators, e.g. in the aforementioned case the third Lorentz oscillator is more than an order of magnitude weaker than any of the first two of them. The metallic VO_2 above T_{tr} was represented by a combination of the Cody-Lorentz oscillator with

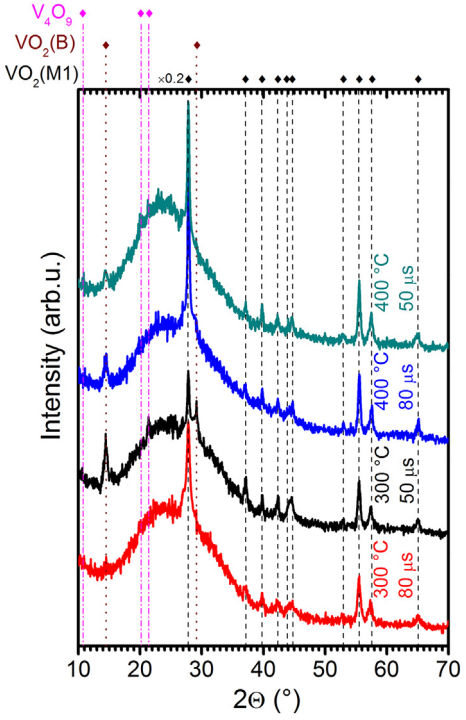

Fig. 1. XRD patterns of the four VO_2 films studied. The labels refer to the deposition temperature T_{dep} = 400 or 300 °C, and the pulse length t_{on} = 50 or 80 µs. The dashed, dotted and dash-dotted vertical lines correspond to the peak positions of VO_2(M1) (PDF#04-003-2035 [30]; the main peak is 5× scaled down), VO_2(B) (PDF#01-084-3056) and V_4O_9 (PDF#04–017-0339), respectively.

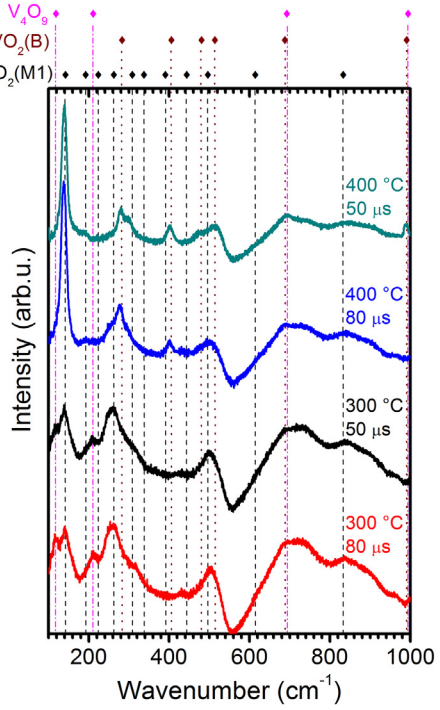

Fig. 2. Raman spectra of the four VO_2 films studied, after subtracting the Raman spectrum of the glass substrate. The dashed, dotted and dash-dotted vertical lines correspond to the peak positions of VO_2(M1) [5, 34], VO_2(B) [35] and V_4O_9 [36], respectively. The figure does not show position of those VO_2(B) and V_4O_9 peaks which overlap with VO_2(M1) peaks.

two Lorentz oscillators centered in IR and visible (e.g. at 0.53 and 2.36 eV, respectively, for T_{dep} = 300 °C and t_{on} = 50 µs) and a Drude oscillator (in order to represent the free charge carriers. This is comparable to VO_2 representations in the literature: three Lorentz oscillators [12], Tauc-Lorentz + two Lorentz oscillators [7] or Tauc-Lorentz + two Gaussian oscillators + Drude oscillator above T_{tr} [8] (let alone a wavelength by wavelength fit without any oscillators [10]).

3. Results and discussion

This section is organized as follows. First, the film structure is shown and discussed in Figs. 1-2. Second, the strength and temperature of the metal-to-insulator transition is shown by hysteresis curves in Figs. 3–4. Third, the spectroscopic data below and above T_{tr} are shown in Figs. 5–9. Following the paper aim, each of the nine figures except Fig. 5 compares the properties achieved at the lowered T_{dep} = 300 °C with those achieved at the more standard T_{dep} = 400 °C. Part of the non-spectroscopic data at T_{dep} = 300 °C are adapted from the initial letter [6] for reader's convenience. All results are summarized and compared with films prepared under other (less industry-friendly) conditions in Table 1.

3.1. Film structure

Fig. 1 shows the XRD patterns of the four films studied. It can be seen that the dominant crystalline phase in all four films is the desired thermochromic phase VO_2(M1) (PDF#04-003-2035 [30]; all peak positions and intensities obtained by the powder diffraction are referred to as theoretical ones throughout this section). The crystal orientation is almost random and independent of T_{dep} and t_{on}. Indeed, the VO_2(M1) peaks which constitute the first, third and fourth theoretically most intensive one for random crystal orientations in a powder sample correspond to the first, second and (perhaps except T_{dep} = 300 °C and

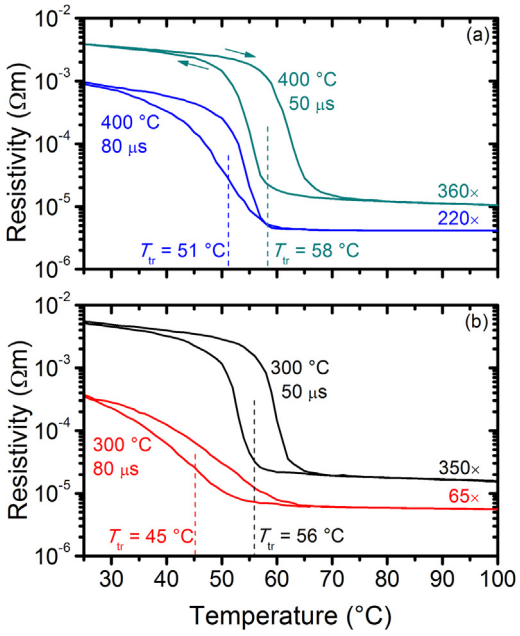

Fig. 3. Temperature (T_m) dependence of the electrical resistivity for the four VO_2 films studied. The strength of the transition (ratio of ρ values at 25 and 100 °C) and the T_{tr} values as indicated by the dashed vertical lines (middle of the hysteresis curves, both vertically and horizontally) are provided as well.

t_{on} = 50 µs) third most intensive visible VO_2(M1) peak, respectively. The corresponding three planes parallel to the film surface are (011) (theoretical peak position 2θ = 27.80°; 5× scaled down in Fig. 1), (211) (2θ = 55.56°) and (022) (2θ = 57.43°), respectively. On the other hand, the theoretically second most intensive peak (−211) (2θ = 36.98°) is visible but - compared to its theoretical intensity -

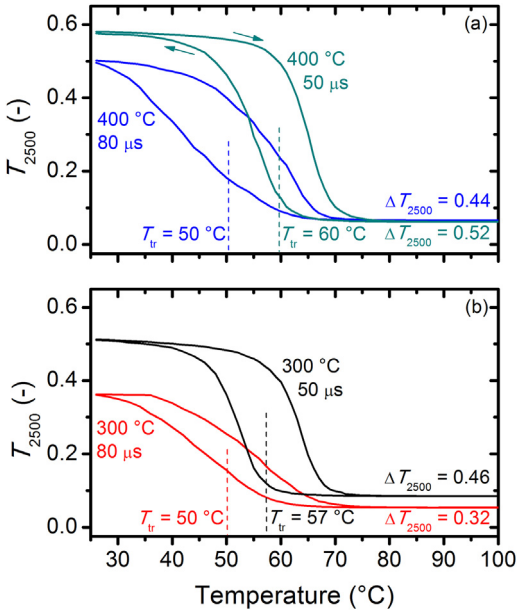

Fig. 4. Temperature (T_m) dependence of the transmittance of approximately 80 nm thick (Table 1) VO_2 on 1 mm thick glass at a wavelength of 2500 nm (T_{2500}) for the four VO_2 films studied. The strength of the transition (difference of T_{2500} values at 25 and 100 °C) and the T_{tr} values as indicated by the dashed vertical lines (middle of the hysteresis curves, both vertically and horizontally) are provided as well.

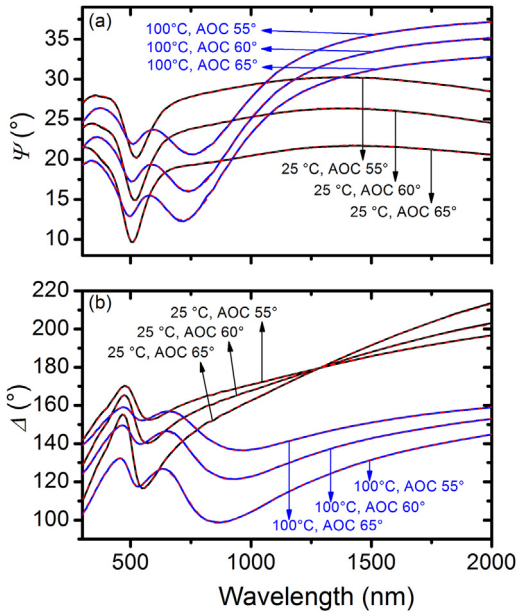

Fig. 5. Spectral dependence of the ellipsometric angles Ψ (panel a) and Δ (panel b) ($r_p/r_s = \tan\Psi.e^{i\Delta}$ where r_p and r_s is the reflectivity of p- and s-polarized light, respectively) at the angles of incidence (AOC) of 55, 60 and 65°. The full black lines show the data measured at T_m = 25°, the full blue lines show the data measured at T_m = 100°, and the dashed red lines show the data fitted using the optical model described in the text. The data constitute an example for T_{dep} = 400 °C and t_{on} = 50 µs (dark cyan lines in all other figures). (For interpretation of the references to colour in this figure legend, the reader is referred to the web version of this article.)

relatively weak, nevertheless indicating a not completely random orientation.

In parallel to the desired phase VO_2(M1), there is a trace amount of two other phases. First, most of the films exhibit a minor fraction of

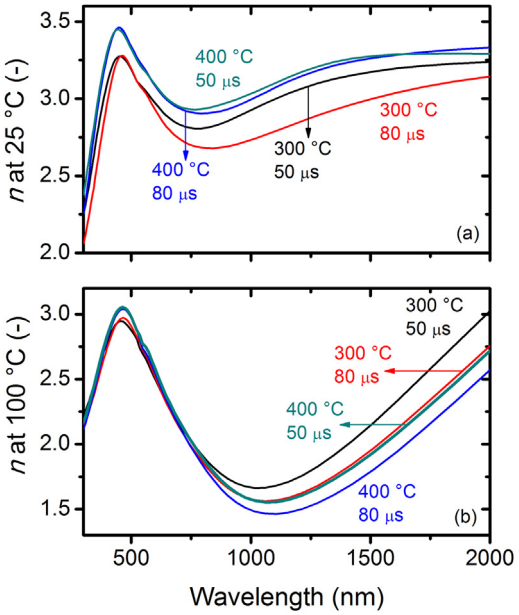

Fig. 6. Spectral dependence of the refractive index (n) for the four VO_2 films studied, measured at T_m = 25 °C (panel a) and 100 °C (panel b).

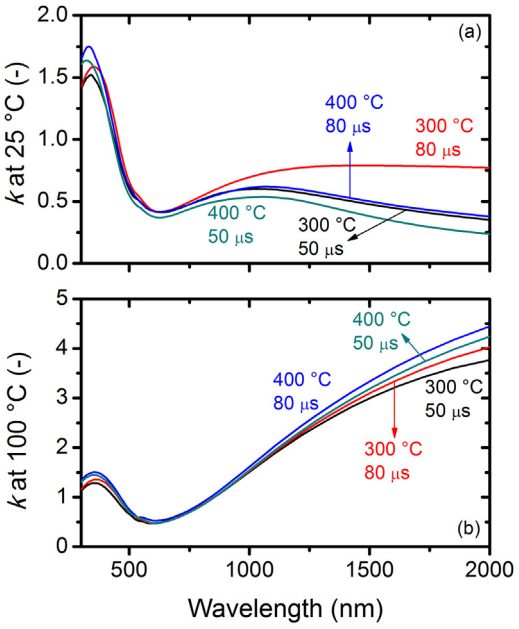

Fig. 7. Spectral dependence of the extinction coefficient (k) for the four VO_2 films studied, measured at T_m = 25 °C (panel a) and 100 °C (panel b).

VO_2(B) (PDF#01-084-3056). Note that while VO_2(M1) is stable at RT and exhibits the aforementioned reversible transition to VO_2(R) around 68 °C, VO_2(B) is metastable and exhibits a non-reversible transition to VO_2(R) just above 400 °C [31, 32] (i.e. its presence is consistent with T_{dep} = 300–400 °C, and supports a statement that the T_{dep} values are not underestimated). The phase VO_2(B) exhibits a preferred orientation with (001) planes ((002) planes for the second order diffraction) parallel to the film surface (2θ = 14.39° and 29.01°, respectively). Second, both films prepared at t_{on} = 50 µs exhibit a very minor fraction of V_4O_9 (PDF#04-017-0339). The visible peaks include the theoretically most intensive one (004) (2θ = 21.45°) and at T_{dep} = 400 °C also (002) (2θ = 10.68°) and (202) (2θ = 20.21°). The theoretically second most intensive peak of V_4O_9, i.e. (220) (2θ = 27.79°), overlaps with the main peak of the dominating phase VO_2(M1).

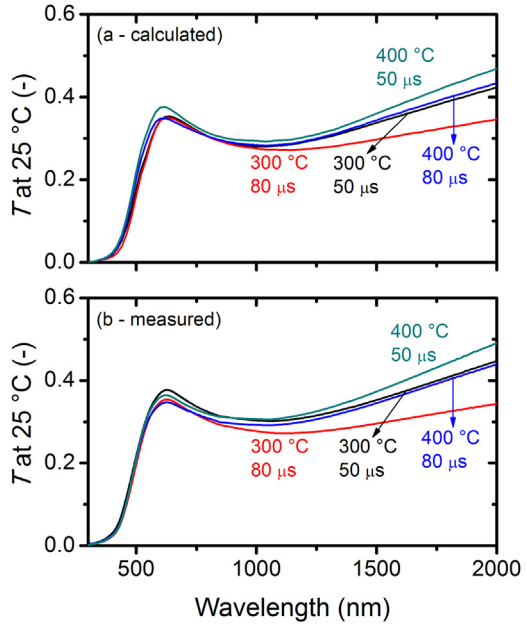

Fig. 8. Spectral dependence of the transmittance (T) of approximately 80 nm thick (Table 1) VO_2 on 1 mm thick glass at T_m = 25 °C for the four VO_2 films studied. Panel a shows T calculated using the data measured by ellipsometry: bulk n (Fig. 7), bulk k (Fig. 8) and thickness. Panel b shows T measured by spectrophotometry.

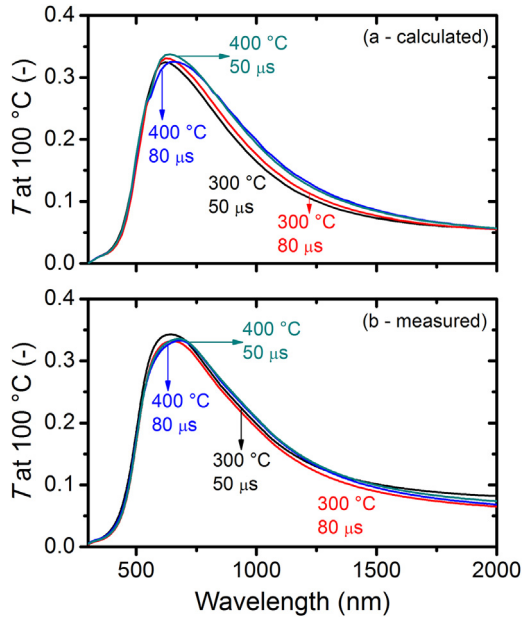

Fig. 9. Spectral dependence of the transmittance (T) of approximately 80 nm thick (Table 1) VO_2 on 1 mm thick glass at T_m = 100 °C for the four VO_2 films studied. Panel a shows T calculated using the data measured by ellipsometry: bulk n (Fig. 7), bulk k (Fig. 8) and thickness. Panel b shows T measured by spectrophotometry.

The widths of the main peak (011) of the phase VO_2(M1) indicate a size of coherently diffracting domains of around 29 nm for the film prepared at T_{dep} = 300 °C and t_{on} = 80 μs, and 69–73 nm for the other three films. The former result is consistent with the fact that longer t_{on} leads to weaker high-energy tails of the energy distribution functions (EDFs) of the arriving particles [6]. The latter result shows that the strong high-energy tails of the EDFs of the arriving particles (including many metal ions) resulting from the short t_{on} = 50 μs sufficiently increase the mobility of deposited atoms and, consequently, the film crystallinity, independently of T_{dep} in the present range. In other words, lowering T_{dep} from 400 to 300 °C does not harm the VO_2 crystallinity for the present optimized deposition technique (HiPIMS with RGFC at the short t_{on} = 50 μs).

Fig. 2 shows the Raman spectra of the four films studied. The figure is consistent with the fact (Fig. 1) that the stoichiometry of all films is close to VO_2. However, there are interesting qualitative differences between individual films. First, both films prepared on glass at T_{dep} = 400 °C exhibit a dominant VO_2(M1) peak at 139 cm^{-1}. Second, both films prepared on glass at T_{dep} = 300 °C exhibit a weaker peak at 139 cm^{-1} but stronger and better positioned VO_2(M1) peaks at 259 cm^{-1} and 498 cm^{-1} (depolarized B_g modes [33]). Third, it is worth to recall that VO_2 deposited using the same technique on crystalline Si [5] exhibits yet another signature, with the strongest VO_2(M1) peaks at 195, 224 and 615 cm^{-1} (polarized A_g modes [33]). This difference can be explained by changes in the crystal orientation: dominantly (011) (with a contribution of (020)) on Si due to the epitaxial growth (see also Ref. [34] for a similar observation), contrary to a much wider range of orientations observed on glass (Fig. 1). All the six aforementioned peak positions are consistent with the VO_2(M1) peak positions in the literature (e.g. 141, 261, 497, 192, 223 and 614 cm^{-1}, respectively, in Ref. [34]; see also the literature overview in Ref. [33]). Although the interpretation is not completely straightforward owing to similar positions reported for some peaks of VO_2(M1) [34], VO_2(B) [35] and V_4O_9 [36], it is the only one which is consistent with the XRD patterns above and (especially) with the properties below.

However, also the Raman spectra include minor peaks which constitute fingerprints of the other phases VO_2(B) and V_4O_9. First, the film which exhibits the highest number of V_4O_9 XRD peaks (T_{dep} = 400 °C and t_{on} = 50 μs) is also the only one which exhibits a minor Raman peak at 991 cm^{-1} (the relevant literature peak positions are 991 cm^{-1} for VO_2(B) [35] and 1000 cm^{-1} for V_4O_9 [36], let alone 993 cm^{-1} for V_2O_5 [37]). Second, there is a wide halo around 700 cm^{-1} (consistent with the literature peak positions of 688 cm^{-1} for VO_2(B) and especially 693 cm^{-1} for V_4O_9 and 697 cm^{-1} for V_2O_5), possibly indicating an oxidation of a thin surface amorphous layer. Third, the aforementioned phases may be at least partially responsible for the minor peaks which are too far (10–20 cm^{-1}) from the nearest literature peak position of VO_2(M1), but close to literature peak positions of VO_2(B) (especially 280, 401 and 515 cm^{-1} at T_{dep} = 400 °C [35]) and V_4O_9 (especially 211 cm^{-1} at T_{dep} = 300 °C [36]).

Note that the trace amounts of phases VO_2(B) and/or V_4O_9 do not harm the overall thermochromic behavior which is due to the dominating phase VO_2(M1). For example, the results below actually show that the only film which does not exhibit any XRD peak of the non-thermochromic phase VO_2(B) (T_{dep} = 300 °C and t_{on} = 80 μs) is the relatively least thermochromic one.

3.2. Hysteresis curves

Figs. 3 and 4 show the semiconductor-to-metal transition in terms of changes in ρ and T_{2500}. The figures show (i) values of these quantities (which also complements Figs. 1–2 concerning the film composition and structure), (ii) ratios or differences of these quantities below and above T_{tr} (measure of the strength of the transition) and (iii) the T_{tr} values.

The first thing to note that independently of T_{dep}, the films exhibit a higher room-temperature resistivity and transmittance at the shorter t_{on} = 50 μs. This is consistent with the fact that increasing t_{on} leads to increasingly effective metal sputtering, and to subsequently decreasing [O]:[V] compositional ratio. Let us also recall that XRD (Fig. 1) shows the O-rich phase V_4O_9 only at t_{on} = 50 μs (albeit Fig. 2 indicates that vibrational modes characteristic of V_4O_9, e.g. in the surface amorphous layer, may exist at any t_{on}).

Second, the strength of the semiconductor-to-metal transition is also

higher at t_{on} = 50 μs, probably owing to the better crystallinity supported by a higher energy delivered into the growing films due to the aforementioned strong high-energy tails of the EDFs. This is despite the slight off-stoichiometry as indicated by the V_4O_9 phase. Quantitatively, the effect of t_{on} is more pronounced at T_{dep} = 300 °C. For example, t_{on} = 80 μs instead of 50 μs means that ρ changes along the transition 65× instead of 350× at T_{dep} = 300 °C, and 220× instead of 360× at T_{dep} = 400 °C (Table 1a). Indeed, in the former case the difference can be expressed also in terms of the size of coherently diffracting VO_2(M1) domains given by the XRD peak widths (Sec. 3.1). However, t_{on} = 50 μs leads to a slightly stronger transition than t_{on} = 80 μs also at T_{dep} = 400 °C, despite the similar XRD peak widths.

Third, the results collectively show that the film properties achieved at the optimum t_{on} = 50 μs are almost independent of T_{dep} in the present range. For example, ρ changes along the transition 360× at T_{dep} = 400 °C and 350× at T_{dep} = 300 °C, and T_{2500} changes along the transition between 0.58 and 0.06 at T_{dep} = 400 °C and h = 80 nm, and between 0.52 and 0.08 at T_{dep} = 300 °C and h = 88 nm. See Table 1a-b for more numerical results. This constitutes one of the key results of this paper, because it shows that using HiPIMS with RGFC at optimum t_{on} allows one to decrease T_{dep} from 400 to 300 °C at not only preserved structure (Sec. 3.1) but also preserved properties.

Finally, the figures show that the transition from T_{dep} = 400 °C to T_{dep} = 300 °C preserves not only the properties below and above T_{tr}, but also T_{tr} in itself. The T_{tr} values obtained are also summarized in Table 1c, including those resulting from hysteresis of ρ (Fig. 3), T_{2500} (Fig. 4) and the ellipsometric angle Ψ_{2000} (less common but also possible [5] approach, not shown graphically). The T_{tr} values at t_{on} = 50 μs are in the range 58–64 °C at T_{dep} = 400 °C and 56–64 °C at T_{dep} = 300 °C, in both cases depending (i) on the quantity of interest and (ii) whether the definition is based on half of the total change of the corresponding quantity (dashed lines in Figs. 3–4) or on it's maximum temperature derivative (not shown graphically). Note that the T_{tr} values are below 68 °C reported for bulk VO_2 in Ref. [21] (although not as low as e.g. 45–50 °C reported for thin films in Ref. [5]). The smaller crystals obtained (especially at T_{dep} = 300 °C) at the longer t_{on} = 80 μs exhibit a lower T_{tr} (also especially at T_{dep} = 300 °C), at the cost of the fact that the transition is weaker. In other words, moving far from the bulk in terms of crystal size moves one far from the bulk also in terms of T_{tr}.

3.3. Spectroscopic data

Owing to the fact that this section primarily deals with the results of the spectroscopic ellipsometry, Fig. 5 shows an example of the ellipsometric data below and above T_{tr}. The figure shows not only the thermochromic transition in itself, but especially the overlap of the experimental data and the data calculated using the optical model used (Sec. 2.3). In addition to the confirmation of the correctness of the oscillators describing VO_2 in itself, note that the overlap is excellent despite the fact that the optical model does not include any density gradient (voids above the substrate-VO_2 interface). In other words, HiPIMS well supports the film densification from the very start of the growth, similarly as reported for other metal oxides prepared in the same way [23, 24, 26] as well as for VO_2 prepared in a similar way [7].

Figs. 6 and 7 show the dispersion of n and k, respectively, obtained from the ellipsometric data. Let us recall that these bulk quantities allow one to truly quantify the film properties in general and the thermochromic behavior in particular, contrary to the (more often reported) thickness-dependent transmittance. Furthermore, these quantities not only (i) affect the light absorption in films, but also allow one to tailor (ii) the optimum film thickness which leads to an interference maximum (minimum) at a wavelength of interest and (iii) the optimum properties and thickness of an antireflection layer on the top of VO_2.

The dispersions are qualitatively similar to each other and to the literature [8]. Two relatively largest quantitative differences include (i) higher room-temperature n at higher T_{dep} (Fig. 6a) and (ii) relatively high room-temperature infrared k of the relatively least crystalline film prepared at T_{dep} = 300 °C and t_{on} = 80 μs (Fig. 7a). It is worth to point out that the film prepared at T_{dep} = 300 °C and t_{on} = 80 μs exhibits more "metallic" properties (low ρ and high infrared k) than that prepared at T_{dep} = 400 °C and t_{on} = 80 μs. This is despite (i) the same film-forming particle fluxes, (ii) qualitatively the same phase composition (at a worse crystallinity in the former case) and (iii) the fact that the worse crystallinity in itself is supposed to even decrease the mobility of free charge carriers. This phenomenon may be caused by an expected larger volume of an amorphous phase at lower T_{dep}: a case can be made that the VO_2 crystal growth supports the O incorporation, while the [O]:[V] ratio in the simultaneously growing amorphous phase is below 2. At the short t_{on} = 50 μs, which guarantees a good crystallinity independently of T_{dep} (Sec. 3.1), the equivalent difference is much less pronounced in Figs. 6–7.

Figs. 8 and 9 show the dispersion of the transmittance below and above T_{tr}, respectively. The figures also constitute a crosscheck of T values (i) calculated from n and k which are themselves calculated from the ellipsometric data and (ii) directly measured by spectrophotometry. Both figures show an excellent agreement between these two sets of data: the sum of both measurement errors and the horizontal non-uniformity is within ± 0.01 below and ± 0.02 above T_{tr}. Qualitatively, the figures show (i) absorption in the ultraviolet due to the soda-lime glass substrates, (ii) approximately the same T below and above T_{tr} in the visible, and (iii) significantly enhanced T above T_{tr} in the infrared, primarily due to the free charge carrier absorption.

Quantitatively, the properties of the film prepared at the low T_{dep} = 300 °C and optimum t_{on} = 50 μs change along the transition in the following way: n_{550} between 3.06 and 2.68, n_{2000} between 3.24 and 3.02, k_{550} only between 0.48 and 0.51, k_{2000} between 0.35 and 3.77, T_{lum} (at h = 88 nm) between 32 and 29% and T_{sol} (at h = 88 nm) between 26 and 22%. Let us recall that all transmittance-related quantities can be significantly varied by varying the film thickness (typically leading to a tradeoff between T_{lum} and a modulation of T_{sol}). The properties obtained at t_{on} = 50 μs and T_{dep} = 300 °C are similar to those obtained at t_{on} = 50 μs and the enhanced T_{dep} = 400 °C. The difference between k_{2000} above T_{tr} of 3.77 at T_{dep} = 300 °C and 4.24 at T_{dep} = 400 °C may look relatively large, but basically both values are sufficiently high to make the materials opaque: e.g. the difference between the corresponding T_{2000} values is 0.01 only. Once again, see Table 1a–b for more numerical results.

The comparison of the film properties with the literature is focused on the thickness-independent optical constants. Table 1d shows that the room-temperature optical constants obtained by HiPIMS with RGFC under the unfavorable conditions used in this work (T_{dep} = 300 °C, conventional soda-lime amorphous glass substrates without any interlayer, no substrate bias) are comparable not only with those obtained under more favorable conditions (T_{dep} = 400 °C) in this work, but also with those obtained under more favorable conditions in the literature. Compare e.g. n_{550} = 3.06 (this work) with 2.8–3.2 [7–10, 12] or k_{550} = 0.48 (this work) with 0.3–0.5 [7–10, 12]. Let alone the low k_{550} = 0.10 obtained (despite the possibly relatively metallic composition, see k_{2000}) using HiPIMS with RGFC for the well crystalline VO_2 deposited onto crystalline Si substrate [5] (indicating, beyond the scope of the present work, the potential of transparent crystalline interlayers).

4. Conclusions

High-power impulse magnetron sputtering with a pulsed reactive gas flow control allowed us to prepare thermochromic VO_2 under exceptionally industry-friendly deposition conditions: onto conventional soda-lime glass substrates without any interlayer, without any substrate bias voltage and at a low deposition temperature of 300 °C. While the qualitative fact that this can be done has been shown in our previous letter, the present paper shows that at an optimum voltage pulse length (i.e. as short pulse length as possible which still leads to the correct film

stoichiometry), the energetic ion bombardment of the growing films leads to a very similar structure and properties of the films prepared at 300 °C and 400 °C. Furthermore, we show that the thickness-independent optical constants are comparable to those achieved (under less industry-friendly deposition conditions) in the literature. The results in general and the lowered deposition temperature in particular are important for the design of pathways for the preparation of thermochromic coatings under industry-friendly conditions, and, in turn, significantly increase the application potential of these coatings.

Acknowledgment

This work was supported by the project LO1506 of the Czech Ministry of Education, Youth and Sports.

References

[1] S. Hoffmann, E.S. Lee, C. Clavero, Examination of the technical potential of near-infrared switching thermochromic windows for commercial building applications, Sol. Energy Mater. Sol. Cells 123 (2014) 65–80.
[2] C.G. Granqvist, Oxide-based chromogenic coatings and devices for energy efficient fenestration: brief survey and update on thermochromics and electrochromics, J. Vac. Sci. Technol. B 32 (2014) 060801.
[3] S. Chen, H. Ma, X. Yi, H. Wang, X. Tao, M. Chen, X. Li, C. Ke, Optical switch based on vanadium dioxide thin films, Infrared Phys. Technol. 45 (2004) 239–242.
[4] S. Chen, H. Ma, X. Yi, T. Xiong, H. Wang, C. Ke, Smart VO_2 thin film for protection of sensitive infrared detectors from strong laser radiation, Sensors Actuators A Phys. 115 (2004) 28–31.
[5] J. Houska, D. Kolenaty, J. Rezek, J. Vlcek, Characterization of thermochromic VO_2 (prepared at 250 °C) in a wide temperature range by spectroscopic ellipsometry, Appl. Surf. Sci. 421 (2017) 529–534.
[6] J. Vlcek, D. Kolenaty, J. Houska, T. Kozak, R. Cerstvy, Controlled reactive HiPIMS – effective technique for low-temperature (300 °C) synthesis of VO_2 films with semiconductor-to-metal transition, J. Phys. D. Appl. Phys. 50 (2017) 38LT01.
[7] J.-P. Fortier, B. Baloukas, O. Zabeida, J.E. Klemberg-Sapieha, L. Martinu, Thermochromic VO_2 thin films deposited by HiPIMS, Sol. Energy Mater. Sol. Cells 125 (2014) 291–296.
[8] S. Loquai, B. Baloukas, O. Zabeida, J.E. Klemberg-Sapieha, L. Martinu, HiPIMS-deposited thermochromic VO_2 films on polymeric substrates, Sol. Energy Mater. Sol. Cells 155 (2016) 60–69.
[9] S. Loquai, B. Baloukas, J.E. Klemberg-Sapieha, L. Martinu, HiPIMS-deposited thermochromic VO_2 films with high environmental stability, Sol. Energy Mater. Sol. Cells 160 (2017) 217–224.
[10] N.R. Mlyuka, G.A. Niklasson, C.G. Granqvist, Thermochromic VO_2-based multilayer films with enhanced luminous transmittance and solar modulation, Phys. Status Solidi A 206 (2009) 2155–2160.
[11] A. Aijaz, Y.-X. Ji, J. Montero, G.A. Niklasson, C.G. Granqvist, T. Kubart, Low-temperature synthesis of thermochromic vanadium dioxide thin films by reactive high power impulse magnetron sputtering, Sol. Energy Mater. Sol. Cells 149 (2016) 137–144.
[12] H. Kakiuchida, P. Jin, S. Nakao, M. Tazawa, Optical properties of vanadium dioxide film during Semiconductive–metallic phase transition, Jpn. J. Appl. Phys. 46 (2007) L113–L116.
[13] N.H. Azhan, K. Su, K. Okimura, J. Sakai, Radio frequency substrate biasing effects on the insulator-metal transition behavior of reactively sputtered VO_2 films on sapphire (001), J. Appl. Phys. 117 (2015) 185307.
[14] D.-P. Zhang, M.-D. Zhu, Y. Liu, K. Yang, G.-X. Liang, Z.-H. Zheng, X.-M. Cai, P. Fan, High performance VO_2 thin films growth by DC magnetron sputtering at low temperature for smart energy efficient window application, J. Alloys Compd. 659 (2016) 198–202.
[15] H. Koo, H.W. You, K.-E. Ko, O.-J. Kwon, S.-H. Chang, C. Park, Thermochromic properties of VO_2 thin film on SiN_x buffered glass substrate, Appl. Surf. Sci. 277 (2013) 237–241.
[16] M.J. Miller, J. Wang, Influence of grain size on transition temperature of thermochromic VO_2, J. Appl. Phys. 117 (2015) 034307.
[17] Y. Choi, Y. Jung, H. Kim, Low-temperature deposition of thermochromic VO_2 thin films on glass substrates, Thin Solid Films 615 (2016) 437–445.
[18] C. Sun, L. Yan, B. Yue, H. Liu, Y. Gao, The modulation of metal–insulator transition temperature of vanadium dioxide: a density functional theory study, J. Mater. Chem. C 2 (2014) 9283–9293.
[19] S.Y. Li, G.A. Niklasson, C.G. Granqvist, Thermochromic fenestration with VO_2-based materials: three challenges and how they can be met, Thin Solid Films 520 (2012) 3823–3828.
[20] F.J. Morin, Oxides which show a metal-to-insulator transition at the Neel temperature, Phys. Rev. Lett. 3 (1959) 34–36.
[21] H.A. Wriedt, The O-V (oxygen-vanadium) system, Bull. Alloy Phase Diagr. 10 (1989) 271–277.
[22] J.M. Tomczak, S. Biermann, Optical properties of correlated materials – or why intelligent windows may look dirty, Phys. Status Solidi B 246 (2009) 1996–2005.
[23] J. Vlcek, J. Rezek, J. Houska, R. Cerstvy, R. Bugyi, Process stabilization and a significant enhancement of the deposition rate in reactive high-power impulse magnetron sputtering of ZrO_2 and Ta_2O_5 films, Surf. Coat. Technol. 236 (2013) 550–556.
[24] J. Vlcek, J. Rezek, J. Houska, T. Kozak, J. Kohout, Benefits of the controlled reactive high-power impulse magnetron sputtering of stoichiometric ZrO_2 films, Vacuum 114 (2015) 131–141.
[25] A. Belosludtsev, J. Vlcek, J. Houska, R. Cerstvy, Reactive high-power impulse magnetron sputtering of ZrO_2 films with gradient ZrO_x interlayers on pretreated steel substrates, J. Vac. Sci. Technol. A 35 (2017) 031503.
[26] J. Vlcek, A. Belosludtsev, J. Rezek, J. Houska, J. Capek, R. Cerstvy, S. Haviar, High-rate reactive high-power impulse magnetron sputtering of hard and optically transparent HfO_2 films, Surf. Coat. Technol. 290 (2016) 58–64.
[27] J. Rezek, J. Vlcek, J. Houska, R. Cerstvy, High-rate reactive high-power impulse magnetron sputtering of Ta-O-N films with tunable composition and properties, Thin Solid Films 566 (2014) 70–77.
[28] A. Belosludtsev, J. Houska, J. Vlcek, S. Haviar, R. Cerstvy, J. Rezek, M. Kettner, Structure and properties of Hf-O-N films prepared by high-rate reactive HiPIMS with smoothly controlled composition, Ceram. Int. 43 (2017) 5661–5667.
[29] available e.g. at http://rredc.nrel.gov/solar/spectra/am1.5/, http://hyperphysics.phy-astr.gsu.edu/hbase/vision/efficacy.html
[30] JCPDS-ICDD, PDF-4 + Database, International Centre for Diffraction Data, Newton Square, PA, USA, 2015.
[31] J.C. Valmalette, J.R. Gavarri, High efficiency thermochromic VO_2(R) resulting from the irreversible transformation of VO_2(B), Mat. Sci. Eng. B 54 (1998) 168–173.
[32] S.R. Popuri, M. Miclau, A. Artemenko, C. Labrugere, A. Villesuzanne, Michael Pollet, Rapid hydrothermal synthesis of VO_2(B) and its conversion to thermochromic VO_2(M1), Inorg. Chem. 52 (2013) 4780–4785.
[33] P. Schilbe, Raman scattering in VO_2, Physica B 316-317 (2002) 600–602.
[34] Y. Hong-Tao, F. Ke-Cheng, W. Xue-Jin, L. Chao, H. Chen-Juan, N. Yu-Xin, Effect of nonstoichiometry on Raman scattering of VO_2 films, Chin. Phys. 13 (2004) 82–84.
[35] L. Soltane, F. Sediri, Rod-like nanocrystalline B-VO_2: hydrothermal synthesis, characterization and electrochemical properties, Mater. Res. Bull. 53 (2014) 79–83.
[36] A. Bouzidi, N. Benramdane, S. Bresson, C. Mathieu, R. Desfeux, M. El Marssi, X-ray and Raman study of spray pyrolysed vanadium oxide thin films, Vib. Spectrosc. 57 (2011) 182–186.
[37] C.V. Ramana, R.J. Smith, O.M. Hussain, M. Massot, C.M. Julien, Surface analysis of pulsed laser-deposited V_2O_5 thin films and their lithium intercalated products studied by Raman spectroscopy, Surf. Interface Anal. 37 (2005) 406–411.

D Improved performance of thermochromic VO_2/SiO_2 coatings prepared by low-temperature pulsed reactive magnetron sputtering: Prediction and experimental verification

D. Kolenaty, J. Houska, J. Vlcek

J. Alloys Compd. 767 (2018) 46–51

Journal of Alloys and Compounds 767 (2018) 46–51

Contents lists available at ScienceDirect

Journal of Alloys and Compounds

journal homepage: http://www.elsevier.com/locate/jalcom

Improved performance of thermochromic VO_2/SiO_2 coatings prepared by low-temperature pulsed reactive magnetron sputtering: Prediction and experimental verification

D. Kolenaty, J. Houska*, J. Vlcek

Department of Physics and NTIS - European Centre of Excellence, University of West Bohemia, Univerzitni 8, 30614, Plzen, Czech Republic

ARTICLE INFO

Article history:
Received 11 April 2018
Received in revised form
29 June 2018
Accepted 8 July 2018
Available online 9 July 2018

Keywords:
VO_2
HiPIMS
Thermochromic coatings
Low deposition temperature
Industry-friendly deposition technique
Antireflection layer

ABSTRACT

The paper deals with thermochromic VO_2/SiO_2 coatings prepared by low-temperature pulsed reactive magnetron sputtering on conventional soda-lime glass substrates without any substrate bias and without any interlayer. Thermochromic VO_2 layers were deposited using reactive high-power impulse magnetron sputtering with a pulsed O_2 flow control at a substrate surface temperature of 300 °C. Antireflection SiO_2 layers were deposited using mid-frequency bipolar dual magnetron sputtering onto the top of VO_2 layers at a surface temperature below 35 °C in order to improve the optical and mechanical performance. We focus on the dependence of the luminous transmittance (T_{lum}) and the modulation of the solar transmittance (ΔT_{sol}) on the SiO_2 layer thickness. The measured dependencies are in good agreement with those predicted using properties of pure VO_2 layers measured by spectroscopic ellipsometry. Two different VO_2 layer thicknesses (30 and 88 nm) have been used to demonstrate the tradeoff between T_{lum} and ΔT_{sol}. We show an improvement due to the SiO_2 overlayer of up to 16% (from 40.3% to 56.3%) for T_{lum} measured at 25 °C and up to 2.6% (from 7.7% to 10.3%) for ΔT_{sol}. The results are important for the design and low-temperature fabrication of high-performance durable thermochromic VO_2-based coatings for smart window applications.

1. Introduction

Vanadium dioxide is a technologically important thin film material of a high current worldwide interest due to its reversible first-order thermochromic transition [1–3]. The transition takes place between a low-temperature semiconductive phase (monoclinic - distorted rutile - VO_2(M1) with the space group $P2_1/c$) and a high-temperature metallic phase (tetragonal - perfect rutile - VO_2(R) with the space group $P4_2/mmm$). The transition leads to temperature-dependent optical properties (infrared transmittance at the first place), electrical conductivity or the electronic part of the thermal conductivity. This leads to a wide range of applications, ranging from controlling the heat fluxes through smart windows, optical switches and smart radiators to a protection of sensitive infrared detectors from a strong laser radiation [4–7].

Magnetron sputtering is probably the most important preparation technique of VO_2 films, and numerous deposition pathways have been reported in recent years [8–17]. The research in this area is focused on (at least) the following three challenges. First, doping of VO_2 by other metals [18,19] in order to decrease the transition temperature (T_{tr}) from 68 °C [2] (bulk materials) or e.g. 50 °C [8] (thin films) to the room temperature. Second, decreasing the deposition temperature (T_{dep}) of crystalline VO_2 at least below 300 °C, ideally without any substrate bias and without any crystalline interlayer [9,17], in order (i) to facilitate the large-scale production by reducing the energy consumption and minimizing problems with temperature uniformity over large substrate surfaces, (ii) to limit the diffusion of harmful elements from substrates such as soda-lime glass and (iii) to allow deposition on temperature-sensitive plastic substrates. Third, improving the luminous transmittance (T_{lum}) and the modulation of the solar transmittance (ΔT_{sol}) of the coatings by antireflection (AR) layers of SiO_2 or SiO_x [20–24], TiO_2 [24–28], ZrO_2 [29] or Al_2O_3 [30]. Let alone the beneficial side-effect of the AR layers: enhanced durability of the coatings due to the mechanical and chemical (prevented contact with the atmosphere) protection.

However, there is a knowledge gap resulting from at least the following two facts. First, the three aforementioned efforts are typically not combined. For example, there is no work dealing with the sputter deposition of VO_2-based coatings with an AR layer at

* Corresponding author.
E-mail address: jhouska@kfy.zcu.cz (J. Houska).

https://doi.org/10.1016/j.jallcom.2018.07.093
0925-8388/

temperatures of all depositions (and post-deposition annealing) below 380 °C. Second, most of the reported results deal with a single AR-layer thickness (see Refs. [25,26] for exceptions), let alone a comparison of predicted and measured optimum AR-layer thickness.

Our recent papers [9,31] show that (and how) high-power impulse magnetron sputtering (HiPIMS) with a pulsed O_2 flow control allows one to prepare thermochromic VO_2 under exceptionally industry-friendly deposition conditions: onto soda-lime glass substrates without any substrate bias and without any interlayer at as low T_{dep} as 300 °C. In Ref. [31] we show that optimum deposition parameters (Sec. 2.1) allowed us to decrease T_{dep} from 400 °C to 300 °C without any concessions in terms of optical properties. (Let alone even lower T_{dep} obtained by combining this deposition technique with less industry-friendly conditions, e.g. 250 °C on a crystalline substrate [8]). The aim of the present paper is threefold: to examine and maximize the potential of SiO_2 to constitute an antireflection and protective overlayer on VO_2 (for various SiO_2 and VO_2 layer thicknesses), to show the ability of the deposition technique used to prepare the whole bilayer coating under the aforementioned industry-friendly conditions, and to show the possibility to correctly predict the optimum SiO_2 layer (and, by extrapolation, any AR layer) thickness and its performance.

2. Methodology

2.1. Coating preparation

The thermochromic VO_2/SiO_2 coatings were prepared by pulsed reactive magnetron sputtering on conventional soda-lime glass substrates (1 mm thick) without any substrate bias and without any interlayer in an ultra-high vacuum multi-magnetron sputter device (ATC 2200-V AJA International Inc.). The base pressure before all depositions was below 10^{-4} Pa.

The thermochromic VO_2 layers were deposited at a thickness (h) of 30 and 88 nm using reactive HiPIMS in Ar-O_2 gas mixtures. An unbalanced magnetron with a planar vanadium target (99.9% purity, diameter of 50.8 mm and thickness of 6 mm) was driven by a high-power pulsed dc power supply (TruPlasma Highpulse 4002 TRUMPF Huettinger). The voltage pulse duration was $t_{on} = 50$ μs at the repetition frequency of 200 Hz (duty cycle of 1%). The deposition-averaged target power density (averaged over the total target area) was close to 13 Wcm^{-2}, the pulse-averaged power density was around 1.3 $kWcm^{-2}$ and the peak power density was 5 $kWcm^{-2}$. The substrate surface temperature was 300 °C. The Ar partial pressure was 1 Pa at a fixed Ar flow rate of 60 sccm, and the O_2 partial pressure was oscillating between 10 and 20 mPa. The key part of our deposition procedure is a feedback pulsed reactive gas flow control (RGFC): the O_2 flow rate was not fixed but pulsing between 0 and 2 sccm, and the duration of the O_2 flow pulses was decided during the depositions by a programmable logic controller using a pre-selected critical value ($p_{ox\_crit} = 15$ mPa) of the O_2 partial pressure (p_{ox}). The desired VO_2 stoichiometry was achieved by RGFC, i.e. by p_{ox} oscillations around an optimum value given by p_{ox_crit}. The VO_2 crystallization was supported by the energy delivered into the growing films by highly ionized fluxes of energetic particles with many metal ions, resulting from the aforementioned high sputtering powers up to 5 $kWcm^{-2}$ corresponding to the short $t_{on} = 50$ μs. Let us emphasize that while p_{ox_crit} has to be chosen within a narrow window (±10%) even at the most optimum t_{on}, at an improper t_{on} this window closes to zero. The possibility of target oxidation (which would make using such high powers impossible) was suppressed not only by RGFC in itself, but also by the (i) O_2 inlet orientation towards the substrate and (ii) O_2 inlet location in the dense plasma in front of the target (which increases the degree of dissociation and subsequently the reactivity of oxygen, allowing one to achieve the desired VO_2 stoichiometry at a very low p_{ox_crit}). A detailed description of this effective controlled deposition technique is given in Ref. [9].

Subsequently (after characterization of the VO_2 layers), the antireflection SiO_2 layers were deposited onto the top of the VO_2 layers using reactive mid-frequency bipolar dual magnetron sputtering in Ar-O_2 gas mixture at $p_{Ar} = 1$ Pa and $p_{ox} = 0.1$ Pa (oxide regime). Two unbalanced magnetrons with planar silicon targets (99.999% purity, diameter of 50.8 mm and thickness of 6 mm) in a commonly used closed magnetic field configuration were driven by a bipolar dual power supply (TruPlasma Bipolar 4010 TRUMPF Huettinger). They operated in the same asymmetric bipolar pulsed mode at the repetition frequency of 50 kHz with the voltage pulse duration of 10 μs(duty cycle of 50%), but their operations were shifted by a half of the period (i.e., by 10 μs). The deposition-averaged target power density (the same for both magnetrons) was close to 8 Wcm^{-2}. The substrate surface temperature was less than 35 °C. The resulting VO_2/SiO_2 coatings were characterized at four SiO_2-layer thickness (h_t) values (62, 109, 155 and 202 nm for $h = 30$ nm, and 56, 97, 139 and 181 nm for $h = 88$ nm), successively increased by performing sets of four subsequent SiO_2 depositions with the same original VO_2 layer. The small differences in h_t achieved at the same deposition times for $h = 30$ and 88 nm are due to changes in the Si targets erosion (the two sets of four SiO_2 depositions were not carried out in the same period).

2.2. Coating characterization

The film structure was confirmed by X-ray diffraction (XRD) using the PANalytical X'Pert PRO instrument working with a CuKα (40 kV, 40 mA) radiation at a glancing incidence of 1°. The rest of the coating characterization in the present paper is focused on those characteristics which are particularly affected by the SiO_2 overlayer. It included (i) transmittance (T) measurements for all h_t values at a measurement temperature (T_m) both below ($T_m = 25$ °C; also referred to as room temperature throughout the manuscript) and above ($T_m = 90$ °C) T_{tr}, (ii) ellipsometric measurements of n, k and h of each VO_2 layer below and above T_{tr}, (iii) prediction of the coating transmittance in a wide h_t range below and above T_{tr}, (iv) ellipsometric measurement of n, k and h_t of a pure SiO_2 layer deposited on Si (in order to predict the approximate deposition rate and, in turn, the optimum deposition times) and (v) ellipsometric measurements of h_t of the thickest SiO_2 overlayer on each VO_2 layer (in order to get the exact deposition rate). Below we also provide values of optical quantities at a specific wavelength (λ) given in the subscript, e.g. n_{550} or T_{550} for $\lambda = 550$ nm.

The transmittance was measured in the wavelength range from 300 to 2500 nm at the normal angle of incidence by spectrophotometry using the Agilent CARY 7000 instrument equipped with an in-house made heat stage. Below we present also two integral quantities: luminous transmittance (T_{lum}) and solar transmittance (T_{sol}) defined as

$$T_{lum} = \int_{380}^{780} \phi_{lum}(\lambda)\phi_{sol}(\lambda)T(\lambda, T_m)d\lambda \Big/ \int_{380}^{780} \phi_{lum}(\lambda)\phi_{sol}(\lambda)d\lambda \quad (1)$$

and

$$T_{sol} = \int_{300}^{2500} \phi_{sol}(\lambda)T(\lambda, T_m)d\lambda \Big/ \int_{300}^{2500} \phi_{sol}(\lambda)d\lambda \quad (2)$$

where φ_{lum} is the luminous sensitivity of the human eye and φ_{sol} is the solar irradiance spectrum at the sea level [32]. The difference of T_{lum} and T_{sol} values below and above T_{tr} is referred to as ΔT_{lum} and ΔT_{sol}, respectively, from now on.

The ellipsometric measurements were performed using the J.A. Woollam Co. Inc. VASE instrument equipped by an Instec heat stage with the Instec STC200 controller, at the angles of incidence of 55, 60 and 65° in reflection. The optical model (Fig. 1) used to fit the optical data measured on and to predict T of pure VO_2 layers consisted of a glass substrate, a bulk VO_2 layer and a surface roughness layer (around 10 nm thick). The optical model used to predict T of VO_2/SiO_2 coatings consisted of a glass substrate, a bulk VO_2 layer, a VO_2+SiO_2 intermix layer (exactly 10 nm thick, following the typical VO_2 surface roughness) and a bulk SiO_2 layer. The VO_2-layer thickness (h) is a sum of that of the bulk VO_2 layer and half of that of the surface roughness layer or intermix layer. The SiO_2-layer thickness (h_t) is a sum of that of the bulk SiO_2 layer and half of that of the intermix layer. VO_2 was represented by a combination of the Cody-Lorentz dispersion formula (oscillator) with Lorentz oscillators and a Drude oscillator. The WVASE software was used to fit the optical data and to calculate T.

3. Results and discussion

Fig. 2 shows that, indeed, the film structure is dominated by the desired thermochromic phase VO_2(M1) (PDF#04-003-2035 [33]). For example, the most intensive peak in Fig. 2 is most intensive also for random crystal orientations in a powder sample and corresponds to (011) planes perpendicular to the diffraction vector (theoretical peak position at $2\Theta = 27.80°$). In addition, there is a trace fraction of non-thermochromic phases of VO_2(B) (PDF#01-084-3056) and V_4O_9 (PDF#04-017-0339). This, however, does not significantly harm the overall thermochromic behavior of the coating (see the transmittances below). Furthermore, the comparison of both XRD spectra shown in Fig. 2 reveals that the phase composition did not change after the deposition of the thickest SiO_2 overlayer ($h_t = 181$ nm). In other words, the structure of SiO_2 is X-ray amorphous, in agreement with its low deposition temperature. The optical constants of VO_2 (not shown graphically) include e.g. $n_{550} = 3.06$ and $k_{550} = 0.48$ below T_{tr} and $n_{550} = 2.68$ and $k_{550} = 0.51$ above T_{tr}. The electrical resistivity of VO_2 was 5.3×10^{-3} Ωm below T_{tr} and 1.5×10^{-5} Ωm above T_{tr} (modulation 350 ×). The optical constants of SiO_2 are very close to a stoichiometric thermally grown oxide (as expected for depositions in the oxide regime).

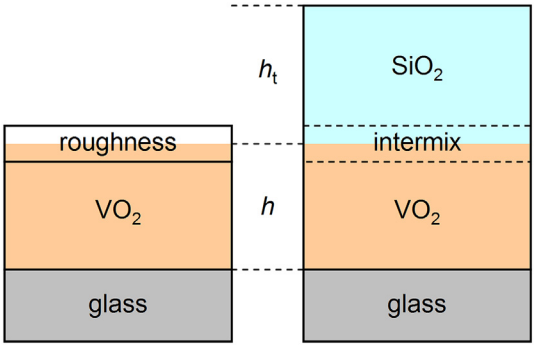

Fig. 1. Optical models used to describe the coating without and with the SiO_2 AR-layer, definition of the VO_2-layer thickness (h) and definition of the SiO_2-layer thickness (h_t). The measured surface roughness layer (VO_2+void) was around 10 nm thick, and half of it contributes to h. The expected intermix layer (VO_2+SiO_2) was exactly 10 nm thick (following the typical VO_2 surface roughness), and contributes to both h and h_t.

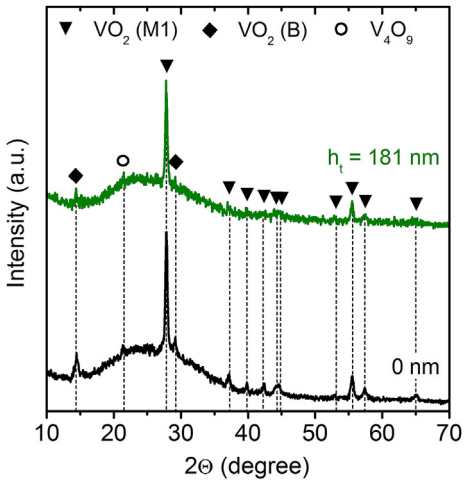

Fig. 2. XRD spectra of the pure VO_2 film with $h = 88$ nm (SiO_2-layer thickness $h_t = 0$; bottom line) and of the same film with the thickest overlayer (SiO_2-layer thickness $h_t = 181$ nm; top line). Relevant peak positions of the phases VO_2(M1) (PDF#04-003-2035 [33]), VO_2(B) (PDF#01-084-3056) and V_4O_9 (PDF#04-017-0339) are marked.

Fig. 3 shows the measured spectral transmittance of the VO_2/SiO_2 coatings, and its modulation by the thermochromic transition. First, the data for pure VO_2 layers (black lines) make clear what is behind the tradeoff represented by the two h values. Fig. 3a shows that the thinner VO_2 layer ($h = 30$ nm) exhibits a high transmittance in the visible at the cost of low modulation of the integrated solar transmittance. The latter is due to the fact that above

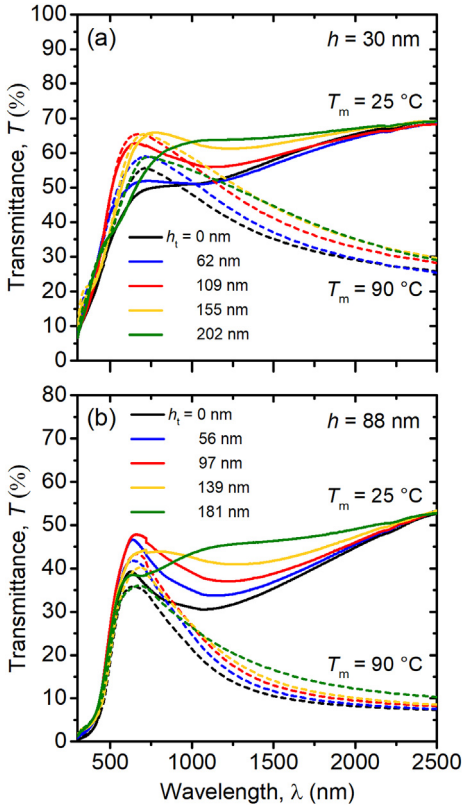

Fig. 3. Spectral transmittance of pure VO_2 layers ($h_t = 0$) and VO_2/SiO_2 bilayers (four h_t values) at the measurement temperature (T_m) below (25 °C, full lines) and above (90 °C, dashed lines) T_{tr}. The data are shown for a VO_2 thickness (h) of 30 nm (panel a) and 88 nm (panel b).

T_{tr} the lower T in the infrared (due to closing of the band gap) is partially compensated by a higher T in the visible (due to a different interference). Although the T enhancement above T_{tr} takes place only in a narrow λ range, this range overlaps with that of high φ_{sol} values. Fig. 3b shows that the thicker VO_2 layer ($h = 88$ nm) exhibits exactly the opposite: higher modulation of the integrated solar transmittance at the cost of lower transmittance in the visible. The former is due to the fact that this time T is lower above T_{tr} in the whole λ range.

Second, most importantly, Fig. 3 shows that the SiO_2 AR-layer indeed leads to a transmittance enhancement. The $T(\lambda)$ dispersions exhibit an interference maximum which shifts to higher wavelengths with increasing h_t. For example, the highest T_{550} was achieved at $h_t = 97$ nm ($h = 88$ nm) - 109 nm ($h = 30$ nm). This is consistent with the simplified interference condition (assuming zero k and no roughness/intermix layer) $h_t = 550/(4n_{550}) = 94$ nm ($n_{550} = 1.46$ for SiO_2). Note that while the AR layer improves the transmittance in itself, the improvement of the modulation of the integrated solar transmittance is limited by the fact that the AR layer increases T not only below but also above T_{tr}. The comparison of Fig. 3a and b indicates that higher h (88 nm) leads (i) to a higher T improvement below T_{tr} (particularly in the infrared) and (ii) to a lower T improvement above T_{tr} (primarily because the T values themselves are lower due to the absorption in the thicker layer of metallic VO_2), i.e. (iii) to a higher improvement of the modulation of the integrated solar transmittance due to the AR layer.

Figs. 4 and 5 quantify the above considerations in terms of the room-temperature integrated quantities T_{lum} and T_{sol} (Fig. 4) and their modulations due to the thermochromic transition (Fig. 5), calculated and measured as a function of h_t. The lines in Fig. 4a predict that the maximum room-temperature T_{lum} can be achieved at $h_t = 100$ nm for 30 nm thick VO_2, and at $h_t = 85$ nm for 88 nm thick VO_2. Although these h_t values are close to the aforementioned $550/(4n_{550}) = 94$ nm, they are neither equal to it nor equal to each other due to the (i) contribution of other wavelengths than 550 nm, (ii) contribution of the interference on VO_2 layers and (iii) non-zero k of VO_2, i.e. phase change at the VO_2/SiO_2 boundary different from 180 deg. The datapoints in Fig. 4a show that the measured T_{lum} (h_t) dependencies are in an excellent qualitative agreement with the predicted ones, and that the measured T_{lum} values are even slightly higher than the predicted ones. Part of the small difference may be due to the thickness of the intermix layer (expected to be 10 nm in Sec. 2): e.g. room-temperature T_{lum} and T_{sol} calculated for $h = 88$ nm and $h_t = 100$ nm change of ±0.4% and ±0.3%, respectively, for intermix layer thickness varied between 5 and 15 nm (not shown). Additional vertical gradient of the coatings, not captured by ellipsometry, may be present as well. The AR layer on the top of 30 nm thick VO_2 improved the experimental room-temperature T_{lum} by 16.0% from 40.3% ($h_t = 0$) to 56.3% ($h_t = 109$ nm), and that on the top of 88 nm thick VO_2 improved the experimental T_{lum} by 5.5% from 32.6% ($h_t = 0$) to 38.1% ($h_t = 97$ nm).

The lines in Fig. 4b predict that the maximum room-temperature T_{sol} can be achieved at $h_t = 115$ nm for 30 nm thick VO_2, and at $h_t = 110$ nm for 88 nm thick VO_2. These h_t values are higher than those leading to the highest T_{lum} due to the contribution of the infrared transmittance. Note that the dependencies in Fig. 4b are far from symmetrical: the initial increase of T_{sol} towards the first order maximum (the only maximum shown) is not followed by any further deep T_{sol} minima between high T_{sol} maxima of higher orders. This is due to the integration over mutually compensating interference minima and maxima of T which are present in the wide 300–2500 nm wavelength range. Again, the datapoints in Fig. 4b show that the measured T_{sol} (h_t) dependencies are in an excellent qualitative agreement with the predicted ones, and that the measured T_{sol} values are slightly higher than the predicted ones. The AR layer on the top of 30 nm thick VO_2 enhanced the experimental room-temperature T_{sol} by 9.1% from 44.8% ($h_t = 0$) to 53.8–53.9% ($h_t = 109$–155 nm), and that on the top of 88 nm thick VO_2 enhanced the experimental T_{sol} by 6.4% from 29.7% ($h_t = 0$) to 36.1% ($h_t = 97$ nm).

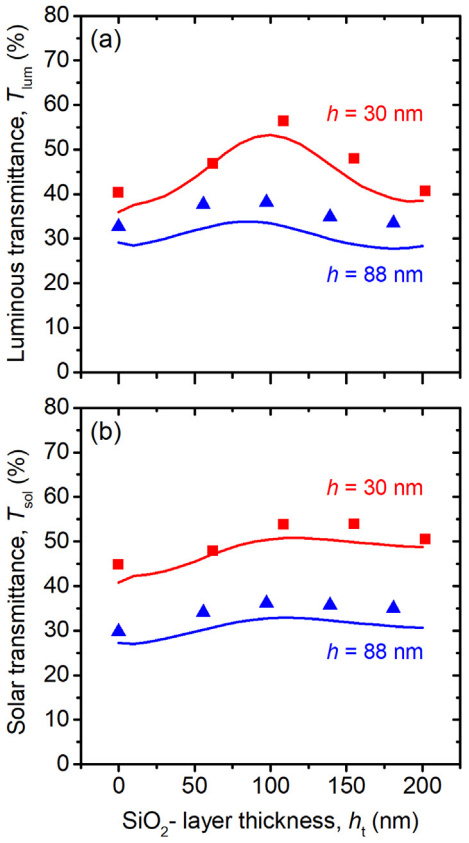

Fig. 4. Dependence of the predicted (lines) and measured (symbols) luminous transmittance (T_{lum}, panel a) and solar transmittance (T_{sol}, panel b) of VO_2/SiO_2 coatings below T_{tr} on the SiO_2-layer thickness. The data are shown for a VO_2 thickness (h) of 30 nm (red squares and lines) and 88 nm (blue triangles and lines). (For interpretation of the references to colour in this figure legend, the reader is referred to the Web version of this article.)

The lines in Fig. 5a predict that the SiO_2 AR-layer leads to a slight enhancement of ΔT_{lum} (except the effect of the VO_2 roughness at zero h_t, which disappears at very low h_t). In other words, the T_{lum} improvement below T_{tr} is higher than that of above T_{tr}. This effect is particularly pronounced at a low h, where the AR layer can compensate the negative ΔT_{lum} exhibited by the pure VO_2 layer. The data points in Fig. 6a show that the predicted and measured data well correspond to each other also in this case (although the relative error of ΔT_{lum} is enhanced by the low ΔT_{lum} values). See e.g. the maximum ΔT_{lum} for $h = 30$ nm: the predicted value is −2.1% at or just below $h_t = 120$ nm, next to the datapoint of −1.5% measured at $h_t = 109$ nm (compensating more than half of $\Delta T_{lum} = -3.8\%$ measured at $h_t = 0$).

Fig. 5b shows the modulation of the other integral quantity, ΔT_{sol}. Let us recall that while ΔT_{lum} (at high T_{lum}) should be close to zero, ΔT_{sol} should be as high as possible. The figure shows that the predicted and measured data once again well correspond to each other, and that the phenomena shown in Fig. 5b for ΔT_{sol} are similar to those shown in Fig. 4b for T_{sol} in itself. First, the first order maximum of ΔT_{sol} is not followed by any further deep minima and high maxima. Second, this maximum is achieved at higher h_t (close to the upper bound of the h_t range shown) than that of T_{lum} and

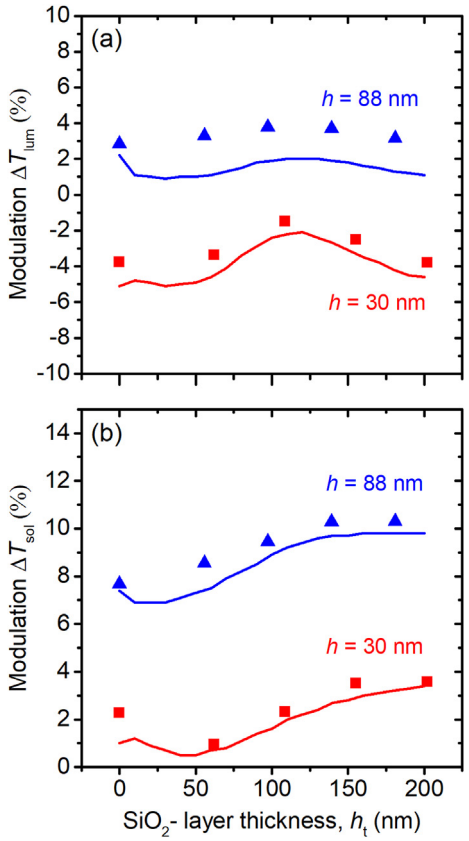

Fig. 5. Dependence of the predicted (lines) and measured (symbols) modulation of the luminous transmittance (ΔT_{lum}, panel a) and modulation of the solar transmittance (ΔT_{sol}, panel b) of VO_2/SiO_2 coatings on the SiO_2-layer thickness. The data are shown for a VO_2 thickness (h) of 30 nm (red squares and lines) and 88 nm (blue triangles and lines). (For interpretation of the references to colour in this figure legend, the reader is referred to the Web version of this article.)

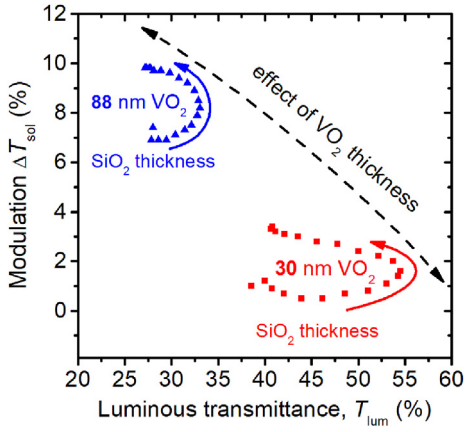

Fig. 6. Calculated relationship between the luminous transmittance (average of T_{lum} values below and above T_{tr}) and the modulation of the solar transmittance (ΔT_{sol}). The data are shown for a VO_2 thickness (h) of 30 nm (red squares) and 88 nm (blue triangles). There are 21 datapoints for each h, corresponding to a SiO_2 thickness (h_t) increasing along the arrows from 0 to 200 nm with a step of 10 nm. The first datapoint ($h_t = 0$) is slightly off the dependence formed by the other datapoints due to the surface roughness of VO_2 (Fig. 1). (For interpretation of the references to colour in this figure legend, the reader is referred to the Web version of this article.)

ΔT_{lum}. The AR layer on the top of 30 nm thick VO_2 enhanced the experimental ΔT_{sol} by 1.3% from 2.3% ($h_t = 0$) to 3.5–3.6% ($h_t = 155–202$ nm), and that on the top of 88 nm thick VO_2 enhanced the experimental ΔT_{sol} by 2.6% from 7.7% ($h_t = 0$) to 10.3% ($h_t = 139–181$ nm). Note that the improvement is two times higher (2.6% compared to 1.3%) for the thicker VO_2 layer ($h = 88$ nm), in agreement with the transmittance spectra shown in Fig. 3 and the discussion therein. Thus, while the usual tradeoff (especially) between T_{lum} and ΔT_{sol} exists also in this case, using the AR layer may shift the optimum h resulting from this tradeoff towards higher values.

The calculated relationship (confirmed experimentally in Figs. 4–5) between the two most technologically important quantities, i.e. T_{lum} and ΔT_{sol}, is directly shown in Fig. 6. The datapoints in Fig. 6 correspond to the same range as the lines in Figs. 4a and 5b. i.e. to $h_t = 0–200$ nm (up to or slightly beyond the first order minimum of T_{lum}). Other combinations of T_{lum} and ΔT_{sol} values can be obtained by utilizing higher-order maxima as indicated by the discussion above (at the cost of increasing importance of the h exactness and uniformity and of the beam angle). The upper envelope of the T_{lum} (ΔT_{sol}) dependencies obtained for individual h values (dashed line in Fig. 5) defines the achievable pairs of T_{lum} and ΔT_{sol}, and represents the aforementioned tradeoff between these quantities (i.e. the effect of the h choice).

While all above figures deal only with $T_m = 25$ and 90 °C (well below and above T_{tr}, respectively), Fig. 7 shows the temperature dependence of T_{2500} in a wide T_m range. While the extremal T_{2500} values have been shown in Fig. 3, the main new information shown in Fig. 7 is the thermochromic transition temperature and its independence of the coating design. The figure confirms that the effect of both (i) VO_2 thickness and (ii) AR overlayer on T_{tr} is negligible. All four T_{tr} values shown in Fig. 7 are within 57 ± 2 °C. Let

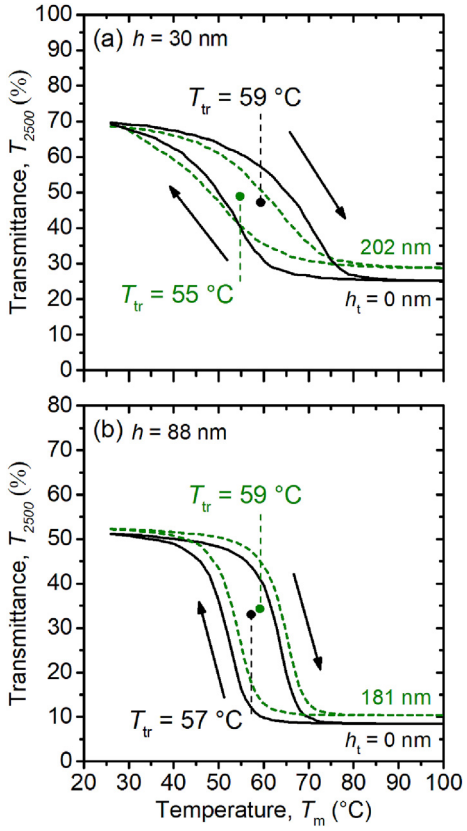

Fig. 7. Temperature (T_m) dependence of the transmittance at $\lambda = 2500$ nm (T_{2500}) for pure VO_2 layers (full lines) and VO_2/SiO_2 bilayers with the thickest SiO_2 layers (dashed lines). The data are shown for a VO_2 thickness (h) of 30 nm (panel a) and 88 nm (panel b). The transition temperatures (T_{tr}) corresponding to the middle of the hysteresis curves, both horizontally and vertically, are denoted as well.

us recall the aforementioned possibility to control this quantity by doping [18,19].

4. Conclusions

Thermochromic VO_2 layers of two different thicknesses were deposited on soda-lime glass substrates by HiPIMS with a pulsed O_2 flow control at a low temperature of 300 °C without any substrate bias and without any interlayer, and antireflection SiO_2 layers of various thicknesses were deposited on the top of them. The results show that the SiO_2 overlayers improved the luminous transmittance (T_{lum}) by up to 16% (from 40.3% to 56.3% for 30 nm thick VO_2) and the modulation of the solar transmittance (ΔT_{sol}) by up to 2.6% (from 7.7% to 10.3% for 88 nm thick VO_2). The results also quantify the tradeoff between (i) T_{lum} and its improvement by the SiO_2 overlayer (these quantities are higher for thinner VO_2) and (ii) ΔT_{sol} and its improvement by the SiO_2 overlayer (these quantities are higher for thicker VO_2). There is an excellent qualitative and a good quantitative agreement of the experimental data and the predictions based on the properties of pure VO_2 and SiO_2. The success of the industry-friendly preparation technique used can be also extrapolated to multilayer coatings which include more than two layers, and the qualitative conclusions concerning the design of the SiO_2 overlayer can be also extrapolated to antireflection layers of other materials.

Acknowledgment

This work was supported by the Czech Science Foundation under Project No. 17-08944S.

References

[1] F.J. Morin, Oxides which show a metal-to-insulator transition at the Neel temperature, Phys. Rev. Lett. 3 (1959) 34–36.
[2] H.A. Wriedt, The O-V (Oxygen-Vanadium) system, Bull. Alloys Phase Diagrams 10 (1989) 271–277.
[3] J.M. Tomczak, S. Biermann, Optical properties of correlated materials – or why intelligent windows may look dirty, Phys. Status Solidi B 246 (2009) 1996–2005.
[4] S. Hoffmann, E.S. Lee, C. Clavero, Examination of the technical potential of near-infrared switching thermochromic windows for commercial building applications, Sol. Energy Mater. Sol. Cells 123 (2014) 65–80.
[5] C.G. Granqvist, Oxide-based chromogenic coatings and devices for energy efficient fenestration: brief survey and update on thermochromics and electrochromics, J. Vac. Sci. Technol. B 32 (2014), 060801.
[6] S. Chen, H. Ma, X. Yi, H. Wang, X. Tao, M. Chen, X. Li, C. Ke, Optical switch based on vanadium dioxide thin films, Infrared Phys. Technol. 45 (2004) 239–242.
[7] S. Chen, H. Ma, X. Yi, T. Xiong, H. Wang, C. Ke, Smart VO_2 thin film for protection of sensitive infrared detectors from strong laser radiation, Sensors Actuators, A Phys. 115 (2004) 28–31.
[8] J. Houska, D. Kolenaty, J. Rezek, J. Vlcek, Characterization of thermochromic VO_2 (prepared at 250 °C) in a wide temperature range by spectroscopic ellipsometry, Appl. Surf. Sci. 421 (2017) 529–534.
[9] J. Vlcek, D. Kolenaty, J. Houska, T. Kozak, R. Cerstvy, Controlled reactive HiPIMS – effective technique for low-temperature (300 °C) synthesis of VO_2 films with semiconductor-to-metal transition, J. Phys. D Appl. Phys. 50 (2017), 38LT01.
[10] J.-P. Fortier, B. Baloukas, O. Zabeida, J.E. Klemberg-Sapieha, L. Martinu, Thermochromic VO_2 thin films deposited by HiPIMS, Sol. Energy Mater. Sol. Cells 125 (2014) 291–296.
[11] N.R. Mlyuka, G.A. Niklasson, C.G. Granqvist, Thermochromic VO_2-based multilayer films with enhanced luminous transmittance and solar modulation, Phys. Status Solidi A 206 (2009) 2155–2160.
[12] A. Aijaz, Y.-X. Ji, J. Montero, G.A. Niklasson, C.G. Granqvist, T. Kubart, Low-temperature synthesis of thermochromic vanadium dioxide thin films by reactive high power impulse magnetron sputtering, Sol. Energy Mater. Sol. Cells 149 (2016) 137–144.
[13] N.H. Azhan, K. Su, K. Okimura, J. Sakai, Radio frequency substrate biasing effects on the insulator-metal transition behavior of reactively sputtered VO_2 films on sapphire (001), J. Appl. Phys. 117 (2015), 185307.
[14] D.-P. Zhang, M.-D. Zhu, Y. Liu, K. Yang, G.-X. Liang, Z.-H. Zheng, X.-M. Cai, P. Fan, High performance VO_2 thin films growth by DC magnetron sputtering at low temperature for smart energy efficient window application, J. Alloys Compd. 659 (2016) 198–202.
[15] H. Koo, H.W. You, K.-E. Ko, O.-J. Kwon, S.-H. Chang, C. Park, Thermochromic properties of VO_2 thin film on SiN_x buffered glass substrate, Appl. Surf. Sci. 277 (2013) 237–241.
[16] M.J. Miller, J. Wang, Influence of grain size on transition temperature of thermochromic VO_2, J. Appl. Phys. 117 (2015), 034307.
[17] Y. Choi, Y. Jung, H. Kim, Low-temperature deposition of thermochromic VO_2 thin films on glass substrates, Thin Solid Films 615 (2016) 437–445.
[18] C. Sun, L. Yan, B. Yue, H. Liu, Y. Gao, The modulation of metal–insulator transition temperature of vanadium dioxide: a density functional theory study, J. Mater. Chem. C 2 (2014) 9283–9293.
[19] S.Y. Li, G.A. Niklasson, C.G. Granqvist, Thermochromic fenestration with VO_2-based materials: three challenges and how they can be met, Thin Solid Films 520 (2012) 3823–3828.
[20] M.-H. Lee, J.-S. Cho, Better thermochromic glazing of windows with antireflection coating, Thin Solid Films 365 (2000) 5–6.
[21] H. Kakiuchida, P. Jin, M. Tazawa, Control of thermochromic spectrum in vanadium dioxide by amorphous silicon suboxide layer, Sol. Energy Mater. Sol. Cells 92 (2008) 1279–1284.
[22] X. Chen, Q. Lv, X. Yi, Smart window coating based on nanostructured VO2 thin film, Optik 123 (2012) 1187–1189.
[23] D. Li, Y. Shan, F. Huang, S. Ding, Sol–gel preparation and characterization of SiO_2 coated VO_2 films with enhanced transmittance and high thermochromic performance, Appl. Surf. Sci. 317 (2014) 160–166.
[24] Z. Chen, Y. Gao, L. Kang, J. Du, Z. Zhang, H. Luo, H. Miao, G. Tan, VO_2-based doublelayered films for smart windows: optical design, all-solution preparation and improved properties, Sol. Energy Mater. Sol. Cells 95 (2011) 2677–2684.
[25] N.R. Mlyuka, G.A. Niklasson, C.G. Granqvist, Thermochromic VO_2-based multilayer films with enhanced luminous transmittance and solar modulation, Phys. Status Solidi A 206 (2009) 2155–2160.
[26] Z. Zhang, Y. Gao, H. Luo, L. Kang, Z. Chen, J. Du, M. Kanehira, Y. Zhang, Z.L. Wang, Solution-based fabrication of vanadium dioxide on F:SnO_2 substrates with largely enhanced thermochromism and low-emissivity for energy-saving applications, Energy Environ. Sci. 4 (2011) 4290–4297.
[27] H. Wang, W. He, G. Yuan, X. Wang, Q. Chen, Large change of visible transmittance with VO_2 phase transition in VO_2/TiO_2 polycrystalline films, Thin Solid Films 540 (2013) 168–172.
[28] P. Jin, G. Xu, M. Tazawa, K. Yoshimura, Design, formation and characterization of a novel multifunctional window with VO_2 and TiO_2 coatings, Appl. Phys. A 77 (2003) 455–459.
[29] G. Xu, P. Jin, M. Tazawa, K. Yoshimura, Optimization of antireflection coating for VO_2-based energy efficient window, Sol. Energy Mater. Sol. Cells 83 (2004) 29–37.
[30] Y.-X. Ji, S.-Y. Li, G.A. Niklasson, C.G. Granqvist, Durability of thermochromic VO_2 thin films under heating and humidity: effect of Al oxide top coatings, Thin Solid Films 562 (2014) 568–573.
[31] J. Houska, D. Kolenaty, J. Vlcek, R. Cerstvy, Properties of thermochromic VO_2 films prepared by HiPIMS onto unbiased amorphous glass substrates at 300 °C, Thin Solid Films 660 (2018) 463–470, https://doi.org/10.1016/j.tsf.2018.06.057.
[32] Available e.g. at http://rredc.nrel.gov/solar/spectra/am1.5/, http://hyperphysics.phy-astr.gsu.edu/hbase/vision/efficacy.html.
[33] Jcpds-icdd, PDF-4+ Database, International Centre for Diffraction Data, Newton Square, PA, USA, 2015.

E Ion-flux characteristics during low-temperature (300 °C) deposition of thermochromic VO_2 films using controlled reactive HiPIMS

J. Vlček, **D. Kolenatý**, T. Kozák, J. Houška, J. Čapek, Š. Kos

J. Phys. D: Appl. Phys. 52 (2019) 025205

IOP Publishing
Journal of Physics D: Applied Physics
J. Phys. D: Appl. Phys. **00** (2018) 000000 (9pp)
UNCORRECTED PROOF

Ion-flux characteristics during low-temperature (300 °C) deposition of thermochromic VO_2 films using controlled reactive HiPIMS

Jaroslav Vlček[1], David Kolenatý, Tomáš Kozák, Jiří Houška, Jiří Čapek and Šimon Kos

Department of Physics and NTIS—European Centre of Excellence, University of West Bohemia, Univerzitní 8, 30614 Plzeň, Czechia

E-mail: vlcek@kfy.zcu.cz

Received 18 July 2018, revised 8 October 2018
Accepted for publication 19 October 2018
Published

Abstract

The ion-flux characteristics at a substrate position and the corresponding discharge characteristics were investigated during controlled low-temperature (300 °C) reactive HiPIMS depositions of thermochromic VO_2 films onto conventional soda-lime glass substrates without any substrate bias voltage and without any interlayer. It was shown that the phase composition of the films correlates with the $(V^+ + V^{2+})$ ion fraction and the $(V^+ + V^{2+})$:$(2O_2^+ + O^+)$ ion ratio in the total ion flux onto the substrate. Setting the amount of oxygen in the gas mixture allowed us to control not only the phase composition of the films but also their crystallinity. It was found that an appropriate composition of the total ion flux and high ion energies (up to 50 eV relative to ground potential) support the crystallization of the thermochromic phase in the VO_2 films. We achieved a high modulation of the transmittance at 2500 nm (between 51% and 8%) and of the electrical resistivity (changed 350 times) for a 88 nm thick VO_2 film.

Keywords: pulsed control, ion-flux characteristic, mass spectroscopy, thermochromic VO_2, HiPIMS

(Some figures may appear in colour only in the online journal)

1. Introduction

Vanadium dioxide (VO_2) exhibits a reversible first-order semiconductor-to-metal transition [1]. At a critical temperature of approximately 68 °C for bulk material [2], VO_2 crystal abruptly changes from a low-temperature monoclinic VO_2(M1) semiconductive phase ($P2_1/c$; distorted rutile) to a high-temperature tetragonal VO_2(R) metallic phase ($P4_2/mmm$; perfect rutile). This structure transition is accompanied by significant changes in the infrared transmittance, and in electrical and thermal conductivity which make VO_2-based films a suitable candidate for numerous applications, such as electronic switches, thermal sensors and energy-saving smart windows with automatically varied solar transmission [3–5].

There have been many investigations and much progress in thermochromic VO_2-based coatings in recent years (see, for example [4, 5], and the works cited therein). However, there are still some obstacles impeding practical applications of VO_2-based smart coatings, including a high temperature needed for fabrication, a high transition temperature, a low luminous transmittance, a low modulation of the solar transmittance and an unattractive color.

Magnetron sputter deposition with its versatility and the ease of scaling up to larger substrate sizes is probably the most important preparation technique of thermochromic VO_2 films. A number of pathways for their deposition by various kinds of magnetron sputtering have been reported in recent

[1] Author to whom any correspondence should be addressed.

JNL:JPD PIPS: AAE9C6 TYPE: PAP TS: NEWGEN DATE:29/10/18 EDITOR: IOP SPELLING: US

years [6–17]. Note that the application potential of these films depends on the ability to achieve not only the VO_2 stoichiometry but also the crystallization of the thermochromic phase (VO_2(R) during the deposition at a temperature above the transition temperature, T_{tr}, and VO_2(M1) at room temperature) under as industry-friendly process conditions as possible, i.e. at the substrate surface temperature $T_s \leqslant 300$ °C, without any substrate bias voltage and without any crystalline interlayer.

The decrease of the deposition temperature of crystalline VO_2 films at least to 300 °C is of key importance: (1) to facilitate their large-scale production by reducing the energy consumption and minimizing problems with a temperature non-uniformity over large substrate surfaces, (2) to limit the diffusion of sodium from the usually used soda-lime glass substrates into the VO_2 films, and (3) to allow deposition of the VO_2 films onto temperature-sensitive plastic substrates.

In our recent work [18], reactive high-power impulse magnetron sputtering (HiPIMS) with a pulsed O_2 flow control and to-substrate O_2 injection into a high-density plasma in front of the sputtered vanadium target was used for low-temperature ($T_s = 300$ °C) deposition of VO_2 films with a pronounced semiconductor-to-metal transition onto conventional soda-lime glass substrates without any substrate bias voltage and without any interlayer. Except for [13], where rf-superimposed dc magnetron sputtering was applied to deposit VO_2 films onto soda-lime glass at $T_s = 300$ °C, there is no work in the literature reporting a magnetron sputter deposition of thermochromic VO_2 films onto unbiased amorphous substrates at $T_s < 400$ °C. Here, it should be mentioned that HiPIMS techniques have the advantage of using essentially conventional magnetron sputtering equipment, while only replacing the power supply. Thus, these techniques can be implemented into industrial-size deposition systems with various target geometries (for example, rotating targets or configurations with multiple magnetron sources with independent operation [19, 20]). Valuable results concerning the low-temperature HiPIMS depositions of thermochromic VO_2 films, but on biased substrates, have been presented in [11, 12, 14].

In this work, we report on the discharge characteristics, and on the ion energy distributions and compositions of the total ion fluxes at the substrate position during low-temperature ($T_s = 300$ °C) depositions of VO_x films using reactive HiPIMS with a feedback pulsed O_2 flow control at various oxygen partial pressures, and a fixed target power and voltage pulse duration. The oxygen partial pressure is an important process parameter significantly affecting not only the complicated processes on the sputter target and in the discharge plasma, which determine the time evolution of the target current and power during discharge pulses [20–22], but also the processes on the surface of growing films [23, 24].

The main aim of the present work is to explain the correlations between the oxygen partial pressure oscillating around pre-selected critical values, and the phase composition and crystallinity of the produced films and their thermochromic properties. In this regard, the paper forms an extension of our recent letter [18] where only fundamental principles of this low-temperature deposition technique were briefly presented. This study is a part of an overall program conducted to develop a new effective magnetron sputter technique for a low-temperature compatible fabrication of high-performance durable thermochromic VO_2-based multilayer coatings for smart-window applications.

2. Methodology

2.1. Film preparation

The films were deposited using an unbalanced magnetron with an indirectly water-cooled planar vanadium target (99.9% V purity, diameter of 50.8 mm, and thickness of 6 mm) in argon-oxygen gas mixtures at the argon pressure $p_{Ar} = 1$ Pa in an ultra-high vacuum multi-magnetron sputter device (ATC 2200-V AJA International Inc.). The stainless-steel vacuum chamber was evacuated by a turbomolecular pump (1200 l s^{-1}) backed up with a double stage Roots pump (27 m^3 h^{-1}). The base pressure before deposition was below 10^{-4} Pa.

The magnetron was driven by a high-power pulsed dc power supply (TruPlasma Highpulse 4002 TRUMPF Huettinger). In this work, the voltage pulse duration, t_{on}, was 50 μs with the repetition frequency, f_r, of 200 Hz giving a duty cycle $t_{on}/T_p = 1\%$, where the pulse period $T_p = 1/f_r$. The deposition-averaged target power density (spatially averaged over the total target area), $\langle S_d \rangle$, was close to 13 Wcm^{-2}.

The target axis of symmetry, pointing at the center of the substrate holder at the distance $d = 145$ mm from the target, was at the angle of 35° from the axis of the substrate holder being at the axis of the vacuum chamber (figure 1). The rotating (20 rpm) conventional soda-lime glass substrate (1 mm thick) was at a floating potential. The substrate surface temperature $T_s = 300$ °C was maintained during the deposition by a built-in heating system calibrated using a thermocouple directly attached to the substrate surface (additional heating effect by the plasma included). Pre-deposition substrate cleaning using rf discharge (50 W in argon at the pressure of 0.4 Pa for 5 min) was performed.

Oxygen was admitted into the vacuum chamber via mass flow controllers and two corundum conduits (figure 1). Two O_2 inlets with a diameter of 1 mm were placed symmetrically above the target racetrack at the same distance of 20 mm from the target surface and oriented to the substrate [25]. The to-substrate O_2 injection in front of the target results in a substantially decreased compound fraction in the target surface layer [23, 24], leading to reduced arcing, increased sputtering of metal atoms, and low production of O^- ions at the target [25], and in a substantially increased compound fraction in the substrate layer due to a significantly increased chemisorption flux of O atoms onto the substrate [23, 24]. This is caused by a substantially (2–3 times in [23]) increased local oxygen partial pressure in front of the O_2 inlets and by a very high degree of dissociation of O_2 molecules in the high-density plasma in front of the target.

Prior to the admission of O_2 into the system, the Ar flow rate was set to 60 sccm and the pumping speed of the turbomolecular pump was adjusted to attain the argon partial pressure $p_{Ar} = 1$ Pa for all the depositions. The values of p_{Ar}, and of $p_{Ar} + p_{O_2}$, where p_{O_2} is the oxygen partial pressure in the

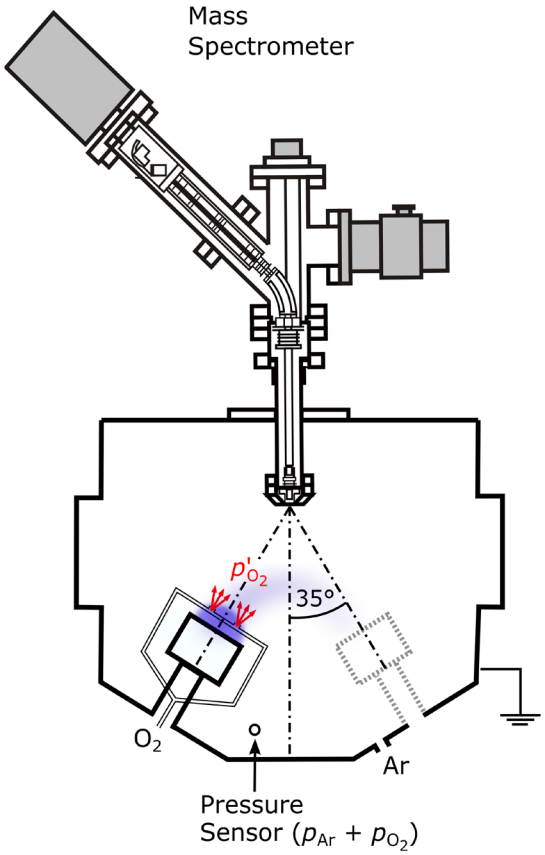

Figure 1. Schematic diagram of the experimental setup with the to-substrate O_2 injection in front of the target (20 mm from the target surface) and an energy-resolved mass spectrometer. Positions of the pressure sensor and the Ar inlet in the vacuum chamber wall are also shown. An increased local value of the oxygen partial pressure due to the O_2 injection is denoted as p'_{O_2}.

chamber, were measured at the chamber wall using a high stability capacitance manometer (Baratron, Type 127, MKS) with the accuracy much better than 1%.

Waveforms of the magnetron voltage, $U_d(t)$, and the discharge current, $I_d(t)$, were monitored [25], and our own software evaluated the time-varying (p_{O_2} oscillates during a deposition, see figures 2–4) average target power density in a discharge pulse, S_{da}, given by

$$S_{da} = \frac{1}{t_{on}} \int_0^{t_{on}} U_d(t) J_t(t) \mathrm{d}t. \quad (1)$$

Here, the target current density $J_t(t) = I_d(t)/A_t$, where A_t is the total area of the target (20.27 cm^2 in our case). The deposition-averaged target power density, $\langle S_d \rangle$, was evaluated with the use of the formula

$$\langle S_d \rangle = \frac{1}{t_e - t_s} \int_{t_s}^{t_e} U_d(t) J_t(t) \mathrm{d}t, \quad (2)$$

where t_s and t_e are the start and end times of the deposition. An analogous integral expression was used to calculate the deposition-averaged oxygen partial pressure, $\langle p_{O_2} \rangle$, from the monitored dependences of $p_{O_2}(t)$.

Prior to a given deposition, we fixed the applied target power density $\langle S_d \rangle \simeq 13\ \mathrm{Wcm^{-2}}$ at an essentially constant value of $U_d(t)$ during discharge pulses, kept by the power supply, and at preset argon partial pressure $p_{Ar} = 1$ Pa and total oxygen flow rate in both conduits $\Phi_{O_2} = 2$ sccm, and a pre-selected critical value, $(p_{O_2})_{cr}$, of the oxygen partial pressure, $p_{O_2}(t)$, which is the process control parameter (input parameter for the feedback control) monitored by a process controller (programmable logic controller). During the deposition, the process controller used then provided a control feedback signal to the O_2 mass flow controllers to adjust the pulsed $\Phi_{O_2}(t)$ by adjusting the duration of the Φ_{O_2} pulses by means of the pre-selected $(p_{O_2})_{cr}$: when $p_{O_2}(t) < (p_{O_2})_{cr}$, $\Phi_{O_2} = 2$ sccm and when $p_{O_2}(t) \geqslant (p_{O_2})_{cr}$, $\Phi_{O_2} = 0$. A basic principle of the pulsed O_2 flow control is illustrated in figures 2–4. Note that, in contrast with standard control systems, the pulsed O_2 flow control does not keep a pre-selected constant value of p_{O_2} during the deposition.

This feedback process control [26] makes it possible to deliver a high power into discharge pulses without arcing on the target surface and thus, to utilize exclusive benefits of the HiPIMS discharges (such as highly ionized fluxes of particles with high fractions of ionized sputtered V atoms onto the substrate, enhanced energies of the ions bombarding the growing films, and a significantly increased chemisorption flux of O atoms onto the substrate) in the preparation of crystalline thermochromic VO_2 films on unbiased amorphous substrates at low T_s.

In the present experiments, we used the preset values of $(p_{O_2})_{cr} = 10$, 15 and 20 mPa (table 1). The time-averaged energy distributions of positive ions incident upon a central region of the substrate holder were measured with an energy-resolved mass spectrometer (EQP300, Hiden Analytical) placed at the same position ($d = 145$ mm) as the substrates during depositions (figure 1). The major natural isotopes of vanadium (^{51}V with 99.7% occurrence), argon (^{40}Ar with 99.6% occurrence) and oxygen (^{16}O with 99.8% occurrence) were considered, together with the corresponding molecular species. Assuming, as is usual (see, for example [21, 27],), the same characteristics for the transmission of all the positive ionic species through the instrument and its energy-independent acceptance cone, the composition of the total flux of positive ions onto the substrate was calculated using the particular integral ion fluxes determined. Taking into account the simplifying assumptions and the mutual position of the target and the mass spectrometer (figure 1), which can result in a lowered detection of high-energy ions, it should be stated here that the presented ion flux characteristics could be determined with relatively high but systematic errors [21, 27]. The flux of negative ions onto the substrate was under the spectrometer detection limit.

2.2. Film characterization

For structural investigation of the films, x-ray diffraction (XRD) measurements were carried out using a PANalytical X'Pert PRO diffractometer working with a CuKα (40 kV, 40 mA) radiation at a glancing incidence of 1°. The average size of coherently diffracting regions of VO_2(M1) phase was

Table 1. Discharge characteristics and compositions of the total fluxes of positive ions at the substrate position during the depositions of VO_x films at $(p_{O_2})_{cr} = 10$, 15 and 20 mPa (see figures 2–4) with the corresponding deposition-averaged oxygen partial pressure $\langle p_{O_2} \rangle$ calculated after the depositions.

Discharge characteristics				Composition of total ion flux						
$\langle S_d \rangle$ (W cm^{-2})	$(p_{O_2})_{cr}$ (mPa)	$\langle p_{O_2} \rangle$ (mPa)	$(S_d)_{max}$ (kW cm^{-2})	V^+	V^{2+}	VO^+	O_2^+ (%)	O^+	Ar^+	Ar^{2+}
13.2	10	10	2.02–3.63	11	2	<1	9	10	66	<1
12.8	15	14	2.74–4.94	6	2	<1	10	14	66	1
12.6	20	18	3.64–6.76	1	<1	<1	13	11	73	<1

estimated from the full width at half maximum of the main VO_2(M1) diffraction peak, corrected for instrumental broadening, using the Scherrer's equation.

The VO_x film thickness (85–118 nm) was measured at room temperature by spectroscopic ellipsometry using the J.A. Woollam Co. Inc. VASE instrument at the angles of incidence of 55, 60 and 65° in reflection. The optical data were fitted using the WVASE software and an optical model consisting of a glass substrate, a bulk VO_x layer and a surface roughness layer. VO_x was represented by a combination of the Cody–Lorentz dispersion formula (oscillator) with Lorentz oscillators.

The residual macrostress, σ, in the films was estimated using the Stoney's formula and the bending of Si stripes (used together with glass substrates) measured by profilometry (Dektak 8 Stylus Profiler, Veeco).

The temperature dependence of the normal-incidence optical transmittance for the wavelength of 2500 nm, T_{2500}, and the electrical resistivity, ρ, were measured in the range of the sample temperatures, T_m, from 25 to 100 °C using a spectrophotometer (Agilent Cary 7000) with a custom-designed heat cell and a four-point probe system (Jandel MACOR Probe Head), respectively.

2.3. Ion backscattering calculations

The backscattering of ions from the surface of V and VO_2 targets was calculated by the SDTrimSP program [28]. The program simulates the trajectory of energetic atoms or ions incident onto a target material using a binary collision approximation (Monte Carlo) method. The backscattering probability and the mean energy of backscattered Ar, V and O atoms, resulting from the bombardment of the target by the respective Ar^+, V^+, O^+ and O_2^+ ions, was evaluated. The interaction between individual atoms was approximated by the Kr-C interatomic potential [29] and the standard displacement energies supplied in the program's material database (26.0 eV and 0.5 eV for V and O, respectively) were used.

3. Results and discussion

3.1. Discharge characteristics

Figures 2–4 show the time evolution of the magnetron voltage, $U_d(t)$, and the target current density, $J_t(t)$, related to the minimum and maximum values of p_{O_2} during depositions of the VO_x films at a preset $\langle S_d \rangle \simeq 13$ Wcm^{-2} and various critical values of the oxygen partial pressure $(p_{O_2})_{cr} = 10$, 15 and 20 mPa, respectively. Thus, figures 2–4 show the ranges of the waveforms of $U_d(t)$ and $J_t(t)$ during the controlled depositions with p_{O_2} oscillating between 6 and 14 mPa at the deposition-averaged value $\langle p_{O_2} \rangle = 10$ mPa, between 10 and 19 mPa at $\langle p_{O_2} \rangle = 14$ mPa, and between 12 and 24 mPa at $\langle p_{O_2} \rangle = 18$ mPa, respectively (table 1), when the pulse-averaged target power densities, S_{da}, were in the range from 1000 to 1450 Wcm^{-2}.

As seen in figures 2–4, the maximum target power density in a discharge pulse, $(S_d)_{max}$, quickly increases (up to 6760 Wcm^{-2} for $p_{O_2} = 24$ mPa at $(p_{O_2})_{cr} = 20$ mPa, see figure 4) with an increase in p_{O_2} resulting in a larger target coverage by a V oxide during the deposition. The higher values of $J_t(t)$ leading to the higher $(S_d)_{max}$ and S_{da} at the higher p_{O_2} can be explained by three factors: (1) A higher density of O_2 molecules and O atoms, arising in front of the partly oxidized V target by an O_2 dissociation and by an intense sputtering from the target [23], at a higher p_{O_2} results in a significantly enlarged flux of the O_2^+ and O^+ ions onto the target for the high target power densities S_{da} applied [30, 31]. At a later stage of discharge pulses, a back attraction of the O^+ ions produced close to the target from the O atoms preferentially sputtered from the target surface becomes particularly important. (2) The O^+ and O_2^+ induced secondary-electron emission coefficients of the target surface may be higher than that induced by Ar^+ ions [21, 32]. (3) The secondary-electron emission coefficient of a V target partly covered by an oxide may increase with the target coverage [33].

3.2. Ion-flux characteristics

The time-averaged energy distribution functions of dominant positive ions and the compositions of the total fluxes of the positive ions at the substrate position are presented in figure 5 and table 1, respectively, for $(p_{O_2})_{cr} = 10$, 15 and 20 mPa. The total ion flux of 8.32×10^5 counts s^{-1} measured for $\langle S_d \rangle = 13.2$ Wcm^{-2} and $(p_{O_2})_{cr} = 10$ mPa decreased to 7.21×10^5 counts s^{-1} for $\langle S_d \rangle = 12.8$ Wcm^{-2} and $(p_{O_2})_{cr} = 15$ mPa, and to 7.08×10^5 counts s^{-1} for $\langle S_d \rangle = 12.6$ Wcm^{-2} and $(p_{O_2})_{cr} = 20$ mPa.

As is typical for reactive HiPIMS discharges (see, for example [21, 22, 25, 27, 34, 35], and the works cited therein), the energy distributions of the positive ions measured at the substrate position for $\langle S_d \rangle \simeq 13$ Wcm^{-2} are extended to high energies (up to 50 eV relative to ground potential) being different for different species (figure 5). The energy distributions

Table 2. The backscattering probability of particles and the mean energy of backscattered atoms at the target surface calculated for the Ar^+, V^+, O^+ and O_2^+ ions incident on V and VO_2 targets with the kinetic energy of 550 eV and 700 eV. For the incident O_2^+ ions, we present the fractions of these ions backscattered from the targets in the form of two neutral O atoms with the same kinetic energy (given for one atom).

Energy of incident ions (eV)	Backscattering probability (%)				Mean energy of backscattered atoms (eV)			
	Ar	V	O	O_2	Ar	V	O	2O
V target								
550	7.0	1.8	19.0	11.1	29.5	23.2	125.0	64.6
700	6.4	1.8	18.0	10.5	38.2	29.5	158.4	81.4
VO_2 target								
550	2.0	0.4	7.4	4.4	20.3	18.7	95.9	50.0
700	1.9	0.4	6.9	4.2	25.3	21.4	121.1	62.6

for V^+, V^{2+} and O^+ ions are similar, having a longer energy tail, while the distributions for Ar^+ and O_2^+ ions are less energetic.

The high-energy parts of the energy distributions for the V^+, V^{2+} and O^+ ions originate from the Thompson energy distribution of sputtered V and O atoms, respectively, which is superimposed with energy gains caused by localized potential humps formed in ionization zones (plasma spokes) close to the target [22, 27, 35]. The effect of the spoke regions on the ionization of Ar atoms and O_2 molecules is much weaker as their densities near the target are significantly reduced [31] mainly due to a momentum transfer from the sputtered V atoms during high-power pulses. In the case of the O^+ ions, a backscattering (reflection) of light O (the relative atomic mass $m_O = 16.00$) atoms from the sputtered V target (the relative atomic mass $m_V = 50.94$) partly covered by a V oxide can be also important.

Table 2 shows that for the kinetic energy of the incident ions in the range from 550 eV (see the minimum $|U_d(t)| = 555$ V for $(p_{O_2})_{cr} = 20$ mPa in figure 4) to 700 eV (see the maximum $|U_d(t)| = 715$ V for $(p_{O_2})_{cr} = 10$ mPa in figure 2), 18%–19% of the incident O^+ ions leave a pure V target surface as neutral O atoms with a mean energy from 125 to 158 eV, respectively. For the same energy range of the incident ions, 11% of the incident O_2^+ ions leave the pure V target surface in the form of two O atoms with the same mean energy from 65 to 81 eV, respectively. In the case of a fully oxidized VO_2 target, the backscattering probabilities would decrease approximately 2.5 times and the mean energies of the backscattered atoms would decrease by almost 25%.

As is seen in table 1 and figure 5, an increase in the $(p_{O_2})_{cr}$ values from 10 to 20 mPa with the corresponding deposition-averaged oxygen partial pressures from 10 to 18 mPa resulted in a rapid decrease in the $(V^+ + V^{2+})$ ion fractions in the total fluxes of positive ions onto the substrate. Let us recall that the fraction of ionized sputtered metal atoms in the total flux onto the substrate is an important characteristic of reactive HiPIMS depositions affecting densification of produced films [25]. The decreased $(V^+ + V^{2+})$ ion fractions with the increased $(p_{O_2})_{cr}$ can be explained by a combination of two main effects: (1) A natural increase in the $(O_2^+ + O^+)$ ion fraction which is limited for $(p_{O_2})_{cr} = 20$ mPa due to a possible reduction in the electron temperature [31]. (2) A decreased sputtering of V atoms from the target due to an increased compound fraction in the target surface layer [23], being important for $(p_{O_2})_{cr} = 20$ mPa as discussed in section 3.1. Moreover, the composition of the total ion flux at the substrate position is influenced by a strongly increased ionization of sputtered V and O atoms, and by an increased backward flux of V^+, V^{2+} and O^+ ions onto the target [23] during the short (shorter for a higher $(p_{O_2})_{cr}$) later stages of the pulses with very high (higher for a higher $(p_{O_2})_{cr}$) target power densities (see figures 2–4). Different time-dependent probabilities of ionization and subsequent return of the sputtered V atoms onto the target during the discharge pulses affect the deposition rate of VO_x films [23, 24].

The elemental composition of the VO_x films deposited onto the substrate is given by complicated time-dependent processes, predominantly the deposition of vanadium and oxygen atoms or ions sputtered as atoms from the target, and the chemisorption of oxygen particles (neutral and ionized atoms and molecules), see details in [23, 24]. Assuming in the first approximation that the $(V^+ + V^{2+})$ flux onto the substrate is proportional to the V flux and the $(2O_2^+ + O^+)$ flux is proportional to the $(2O_2 + O)$ flux, and that the sticking coefficients of all the oxygen particles on the growing films are the same, the $(V^+ + V^{2+})$:$(2O_2^+ + O^+)$ ion ratio in the flux onto the substrate can be used to characterize the trends in the elemental composition of films.

Comparing the ion energy distributions obtained at $(p_{O_2})_{cr} = 10$ and 15 mPa, when we measured sufficiently high $(V^+ + V^{2+})$:$(2O_2^+ + O^+)$ ion ratios (table 1) needed for preparation of VO_2 films (see section 3.3), it is seen in figure 5 that the higher-energy parts of all ion energy distributions at the substrate position are more populated for $(p_{O_2})_{cr} = 15$ mPa. This is a consequence of the much higher target power densities at the later stages of the pulses for $(p_{O_2})_{cr} = 15$ mPa (see the much higher $(S_d)_{max}$ oscillating between 2740 and 4940 Wcm^{-2} at $(p_{O_2})_{cr} = 15$ mPa (figure 3) in comparison with those oscillating between 2020 and 3630 Wcm^{-2} at $(p_{O_2})_{cr} = 10$ mPa (figure 2)). The same effect of the higher peak power on the broadening of the energy distributions for Ti^+ and O^+ ions was observed in a reactive HiPIMS deposition of TiO_2 films [34]. In the recent study [35] dealing with an origin of the energetic ions at the substrate during a HiPIMS deposition of Ti films, the broadening of the measured energy distributions for Ti^+ and Ti^{2+} ions at higher target power densities was explained by a growing width of double layers surrounding the mentioned spoke regions in front of the sputter target. Moreover, a time dependence of the local electric fields in the spoke

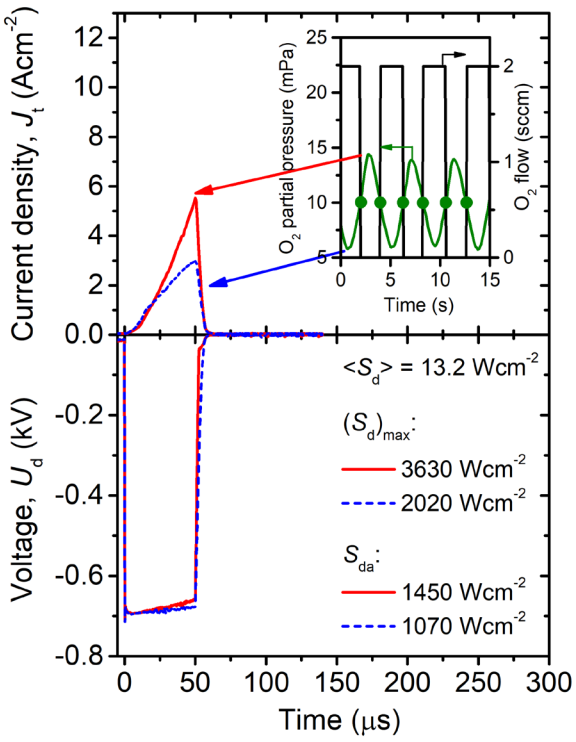

Figure 2. Waveforms of the magnetron voltage, U_d, and the target current density, J_t, for a preset deposition-averaged target power density $\langle S_d \rangle = 13.2\ \mathrm{W\,cm^{-2}}$ with the maximum target power densities in a discharge pulse $(S_d)_{max} = 2020$ W cm^{-2} and 3630 W cm^{-2}, and the pulse-averaged target power densities $S_{da} = 1070$ W cm^{-2} and 1450 W cm^{-2} related to the minimum and maximum values of the oxygen partial pressure, p_{O_2}, respectively, during a deposition of VO_2 films. Time evolution of p_{O_2} during the deposition is shown in the inset. A pre-selected critical value $(p_{O_2})_{cr} = 10$ mPa determining the switching-on and switching-off of the oxygen flow rate $\Phi_{O_2} = 2$ sccm is marked by dots.

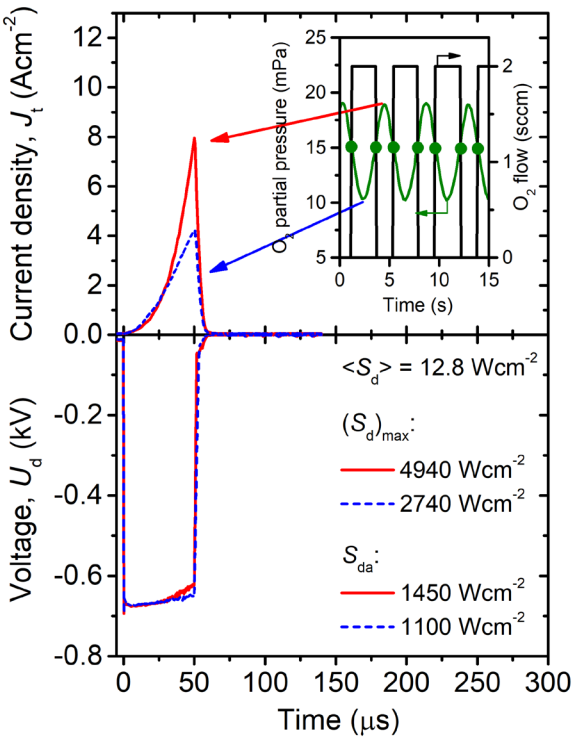

Figure 3. Similar to figure 2, but for $\langle S_d \rangle = 12.8\ \mathrm{W\,cm^{-2}}$ and $(p_{O_2})_{cr} = 15$ mPa.

regions along the ion trajectories was mentioned as a further possible reason for the broadening of the ion energy distributions at higher target power densities. As is seen in figure 5, the highest $(S_d)_{max}$ oscillating between 3640 and 6760 Wcm^{-2} at $(p_{O_2})_{cr} = 20$ mPa (figure 4) did not result in the most populated higher-energy parts of the ion energy distributions, except for the Ar^+ ions. For the V^+, V^{2+} and O^+ ions, for which the high-energy parts of the energy distributions originate from the Thompson energy distribution of the corresponding sputtered atoms superimposed with energy gains in the plasma spokes, the effect of the highest $(S_d)_{max}$ is compensated by a lower energy of the sputtered V and O atoms due to a decreased magnetron voltage to $U_d = 555$ V (figure 4). The lower U_d leads also to a lower energy of O atoms backscattered from the target surface (table 2). Similar O_2^+ ion energy distributions for $(p_{O_2})_{cr} = 10$–20 mPa is a consequence of a weak effect of the plasma spokes, as the O_2 molecules are ionized at larger distances from the target (to-substrate O_2 injection 20 mm from the target and gas rarefaction in front of the target).

3.3. Film structure and properties

Figure 6 shows the XRD patterns taken from the VO_x films prepared at three different $(p_{O_2})_{cr}$ values from 10 to 20 mPa.

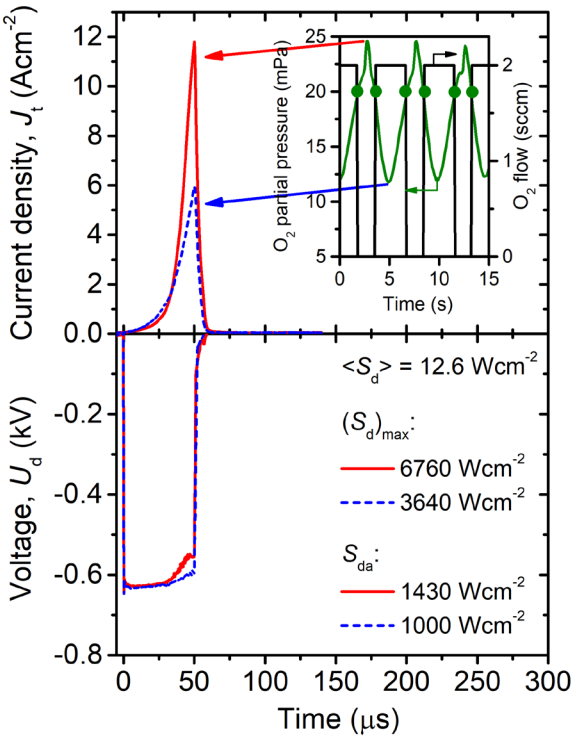

Figure 4. Similar to figure 2, but for $\langle S_d \rangle = 12.6\ \mathrm{W\,cm^{-2}}$ and $(p_{O_2})_{cr} = 20$ mPa. Under these conditions, semiconductive non-thermochromic VO_x films were produced (see figure 7).

As is seen in figure 6 and table 1, the phase composition of the films correlates with the $(V^+ + V^{2+})$ ion fraction (13%, 8% and <2% for $(p_{O_2})_{cr} = 10$, 15 and 20 mPa, respectively) and with the $(V^+ + V^{2+})$:$(2O_2^+ + O^+)$ ion ratio (0.46, 0.24

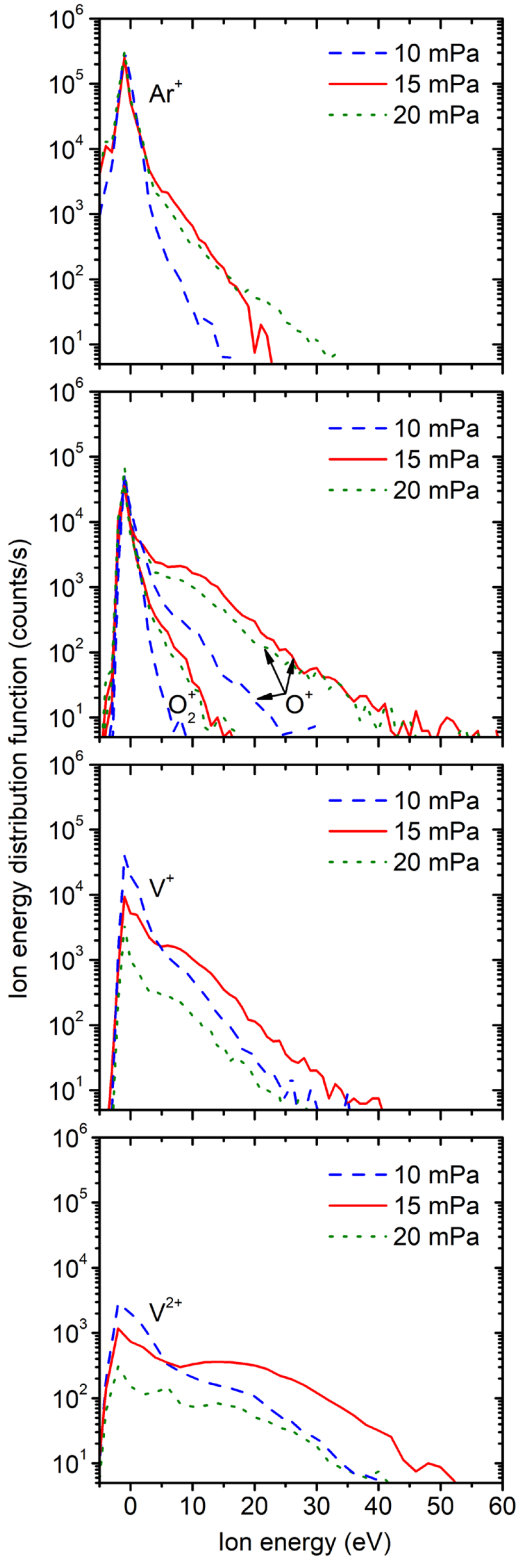

Figure 5. Time-averaged energy distribution functions of dominant positive ions at the substrate position measured for $\langle S_d \rangle \simeq 13\,\mathrm{W\,cm^{-2}}$ and various critical values of the oxygen partial pressure $(p_{O_2})_{cr} = 10$, 15 and 20 mPa.

and < 0.05 for $(p_{O_2})_{cr} = 10$, 15 and 20 mPa, respectively) in the total ion flux onto the substrate.

The film prepared at the lowest $(p_{O_2})_{cr} = 10$ mPa exhibits only the thermochromic phase VO_2(M1) (PDF# 04-003-2035

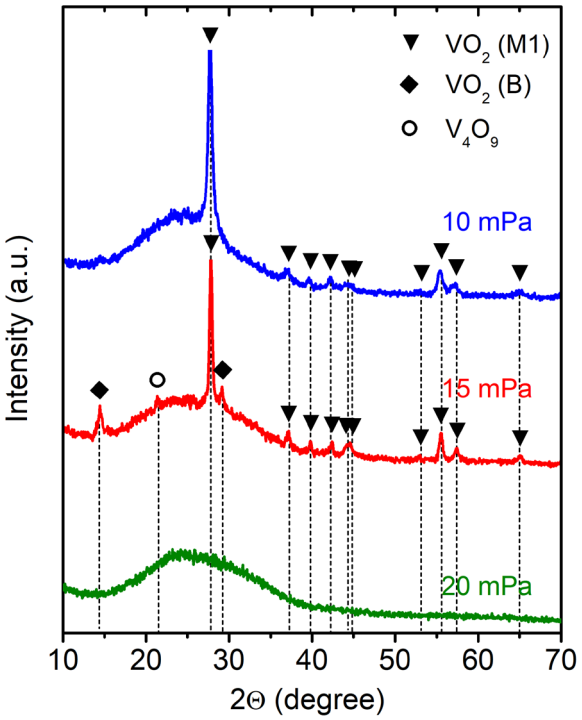

Figure 6. X-ray diffraction patterns taken at $T_m = 25$ °C from the VO_x films with the thickness of 85, 88 and 118 nm prepared at various critical values of the oxygen partial pressure $(p_{O_2})_{cr} = 10$, 15 and 20 mPa, respectively. The main diffraction peaks of VO_2(M1), VO_2(B) and V_4O_9 are marked.

[36]), indicating the desired [V]:[O] compositional ratio close to 0.5. The phase composition of the film prepared at higher $(p_{O_2})_{cr} = 15$ mPa is dominated by the thermochromic phase VO_2(M1). Thus, this film can also be referred to as VO_2. However, small peaks corresponding to the phases V_4O_9 (PDF# 04-017-0339) and VO_2(B) (PDF# 01-084-3056) are also visible, indicating [V]:[O] slightly below 0.5. A case can be made that while the non-thermochromic phase VO_2(B) is less stable than the thermochromic phase VO_2(M1) for the exact stoichiometric composition, it is more prone to forming under O-rich conditions, for example, due to its stabilization by metal vacancies. The film prepared at the highest $(p_{O_2})_{cr} = 20$ mPa is amorphous. It is semiconductive and well transparent (see figure 7) which indicates its [V]:[O] considerably below 0.5.

Figure 7 examines the semiconductor-to-metal transition of the aforementioned three films in terms of T_{2500} and ρ between 25 and 100 °C. The film prepared at $(p_{O_2})_{cr} = 15$ mPa ([V]:[O] slightly below 0.5) exhibits a strong thermochromic effect: T_{2500} changes between 51% and 8%, and ρ changes 350 times between 5.3×10^{-3} Ωm and 1.5×10^{-5} Ωm with a transition temperature $T_{tr} = 56$ °C–57 °C. On the contrary, the film prepared at $(p_{O_2})_{cr} = 10$ mPa ([V]:[O] close to 0.5) exhibits a much weaker thermochromic effect: T_{2500} changes between 21% and 5%, and ρ changes 6.3 times between 2.6×10^{-5} Ωm and 4.1×10^{-6} Ωm with a transition temperature $T_{tr} = 43$ °C–44 °C.

The stronger thermochromic effect at $(p_{O_2})_{cr} = 15$ mPa compared to $(p_{O_2})_{cr} = 10$ mPa, despite the slightly worse stoichiometry, can be explained by a better crystallinity of

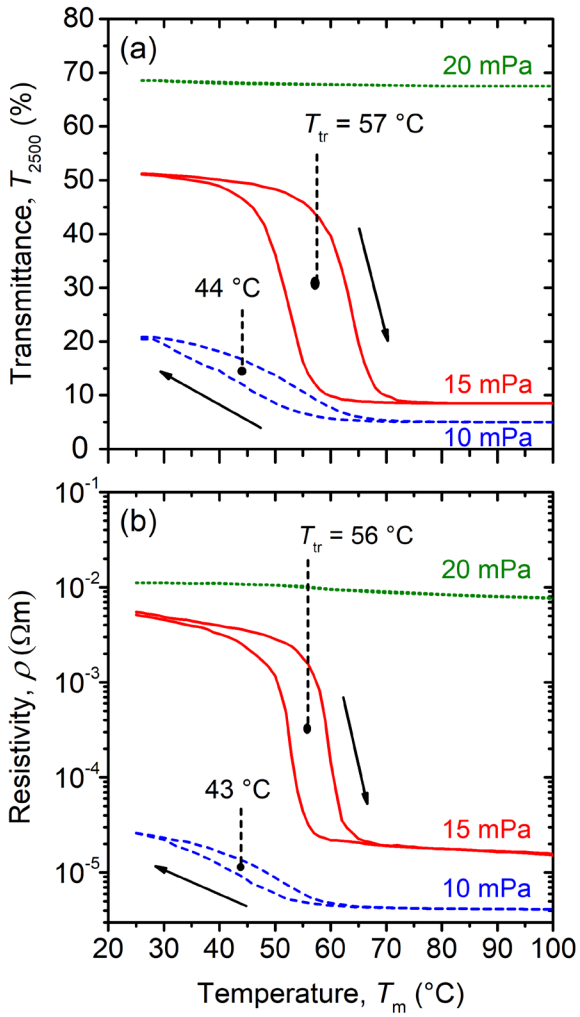

Figure 7. Temperature (T_m) dependence of the transmittance at 2500 nm (a) and the electrical resistivity (b) for the VO_x films with the thickness of 85, 88 and 118 nm deposited onto 1 mm thick glass substrates at various critical values of the oxygen partial pressure $(p_{O_2})_{cr}$ = 10, 15 and 20 mPa, respectively. The transition temperatures, T_{tr}, are also given.

the former film. The VO_2(M1) XRD peak widths (figure 6) indicate a size of coherently diffracting regions of 73 nm and 28 nm in the 88 nm and 85 nm thick films prepared at $(p_{O_2})_{cr}$ = 15 mPa and 10 mPa, respectively. The transition temperatures are consistent with the crystallinity as well: the film prepared at $(p_{O_2})_{cr}$ = 15 mPa exhibits not only a much larger size of coherently diffracting regions, but also T_{tr} closer to the reported bulk value of 68 °C [2]. On the other hand, the film stress, which can also contribute to decreasing the transition temperature (see, for example, the discussion in [8]), was almost the same ($\sigma \simeq -1$ GPa) at $(p_{O_2})_{cr}$ = 10 and 15 mPa.

In spite of the aforementioned simplifying assumptions applied to the mass spectroscopy measurements (see section 2.1) and their implication for the elemental composition of films (see section 3.2), the presented ion flux characteristics are of key importance for the explanation of not only the different phase compositions of the produced VO_x films but also their different crystallinity. The much higher fractions of the high-energy (up to 50 eV relative to ground potential) ions at $(p_{O_2})_{cr}$ = 15 mPa compared with those at $(p_{O_2})_{cr}$ = 10 mPa (see figure 5), when the similar phase composition of the VO_2 films was formed, support the crystallization of the thermochromic phase (VO_2(R) during the deposition at $T_s > T_{tr}$ and VO_2(M1) at room temperature—figure 6) in the VO_2 films growing on glass substrates at a floating potential. Assuming the same atomic density of the VO_2 films with the similar phase composition and very different crystallinity produced at $(p_{O_2})_{cr}$ = 10 and 15 mPa, and taking into account the decrease of the total ion flux from 8.32×10^5 counts s^{-1} for $(p_{O_2})_{cr}$ = 10 mPa to 7.21×10^5 counts s^{-1} for $(p_{O_2})_{cr}$ = 15 mPa and the corresponding decrease of the deposition rate of the films from 1.9 nm min^{-1} to 1.7 nm min^{-1}, it can be stated that these films were deposited at almost the same total ion flux per deposited atom. Recently, the importance of the high-energy film-forming particles for the crystallinity of films has been pointed out for ZrO_2 [37].

The reactive HiPIMS technique with the pulsed O_2 flow control can be easily combined with other pulsed magnetron sputter techniques which can operate simultaneously (atomic doping of VO_2 to decrease T_{tr}) with the controlled reactive HiPIMS deposition, before it (structural template and antireflection layers on substrates) or after it (antireflection and protective layers on VO_2-based layers). In separate papers, we will present the results for advanced thermochromic VO_2-based trilayer coatings which were deposited using this combined technique onto 1 mm thick soda-lime glass at T_s = 330 °C. Their luminous transmittance is above 50% at a modulation of the solar transmittance above 10% and doping-dependent transition temperatures down to T_{tr} = 20 °C. Let us mention that the luminous transmittance of the 88 nm thick VO_2 film, presented in this work, is 32.6% at a modulation of the solar transmittance of 7.7%.

4. Conclusions

It was shown that the phase composition of the films correlates with the $(V^+ + V^{2+})$ ion fraction and the $(V^+ + V^{2+})$:$(2O_2^+ + O^+)$ ion ratio in the total ion flux onto the substrate, which are given by a pre-selected $(p_{O_2})_{cr}$ determining the range of the p_{O_2} oscillating during the deposition. Setting the amount of oxygen in the gas mixture allowed us to control not only the phase composition of the films but also their crystallinity (by means of increased ion energies). It was found that an appropriate composition of the total ion flux and high ion energies (up to 50 eV relative to ground potential) support the crystallization of the thermochromic phase (VO_2(R) during the deposition and VO_2(M1) at room temperature) in the VO_2 films deposited at T_s = 300 °C onto conventional soda-lime glass substrates without any substrate bias voltage and without any interlayer.

We have thus demonstrated a great potential of the controlled reactive HiPIMS for a low-temperature compatible fabrication of high-performance durable thermochromic VO_2-based coatings for smart-window applications.

Acknowledgments

This work was supported by the Czech Science Foundation under Project No. 17-08944S.

ORCID iDs

Jaroslav Vlček https://orcid.org/0000-0003-2627-2074
Tomáš Kozák https://orcid.org/0000-0002-5046-7253

References

[1] Morin F J 1959 *Phys. Rev. Lett.* **3** 34
[2] Wriedt H A 1989 *Bull. Alloy Phase Diagr.* **10** 271
[3] Tomczak J M and Biermann S 2009 *Phys. Status Solidi* b **246** 1996
[4] Granqvist C G 2016 *Thin Solid Films* **614** 90
[5] Wang S, Liu M, Kong L, Long Y, Jiang X and Yu A 2016 *Prog. Mater. Sci.* **81** 1
[6] Mlyuka N R, Niklasson G A and Granqvist C G 2009 *Phys. Status Solidi* a **206** 2155
[7] Koo H, You H W, Ko K-E, Kwon O-J, Chang S-H and Park C 2013 *Appl. Surf. Sci.* **277** 237
[8] Fortier J-P, Baloukas B, Zabeida O, Klemberg-Sapieha J E and Martinu L 2014 *Sol. Energy Mater. Sol. Cells* **125** 291
[9] Azhan N H, Su K, Okimura K and Sakai J 2015 *J. Appl. Phys.* **117** 185307
[10] Miller M J and Wang J 2015 *J. Appl. Phys.* **117** 034307
[11] Aijaz A, Ji Y-X, Montero J, Niklasson G A, Granqvist C G and Kubart T 2016 *Sol. Energy Mater. Sol. Cells* **149** 137
[12] Loquai S, Baloukas B, Zabeida O, Klemberg-Sapieha J E and Martinu L 2016 *Sol. Energy Mater. Sol. Cells* **155** 60
[13] Choi Y, Jung Y and Kim H 2016 *Thin Solid Films* **615** 437
[14] Loquai S, Baloukas B, Klemberg-Sapieha J E and Martinu L 2017 *Sol. Energy Mater. Sol. Cells* **160** 217
[15] Dietrich M, Kuhl F, Polity A and Klar P J 2017 *Appl. Phys. Lett.* **110** 141907
[16] Chang T, Cao X, Li N, Long S, Gao X, Dedon L R, Sun G, Luo H and Jin P 2017 *ACS Appl. Mater. Interfaces* **9** 26029
[17] Houska J, Kolenaty D, Rezek J and Vlcek J 2017 *Appl. Surf. Sci.* **421** 529
[18] Vlček J, Kolenatý D, Houška J, Kozák T and Čerstvý R 2017 *J. Phys. D: Appl. Phys.* **50** 38LT01
[19] Gudmundsson J T, Brenning N, Lundin D and Helmersson U 2012 *J. Vac. Sci. Technol.* A **30** 030801
[20] Gudmundsson J T 2015 *Plasma Phys. Control. Fusion* **58** 014002
[21] Aiempanakit M, Aijaz A, Lundin D, Helmersson U and Kubart T 2013 *J. Appl. Phys.* **113** 133302
[22] Anders A 2017 *J. Appl. Phys.* **121** 171101
[23] Kozák T and Vlček J 2016 *J. Phys. D: Appl. Phys.* **49** 055202
[24] Kozák T and Vlček J 2017 *J. Appl. Phys.* **122** 043304
[25] Vlček J, Rezek J, Houška J, Kozák T and Kohout J 2015 *Vacuum* **114** 131
[26] Vlček J, Rezek J, Houška J, Čerstvý R and Bugyi R 2013 *Surf. Coat. Technol.* **236** 550
[27] Panjan M, Franz R and Anders A 2014 *Plasma Sources Sci. Technol.* **23** 025007
[28] Eckstein W, Dohmen R, Mutzke A and Schneider R 2007 Sdtrimsp: a Monte-Carlo code for calculating collision phenomena in randomized targets *Technical Report*, Max-Planck-Institute für Plasmaphysik
[29] Wilson W D, Haggmark L G and Biersack J P 1977 *Phys. Rev.* **B15** 2458
[30] Benzeggouta D, Hugon M C, Bretagne J and Ganciu M 2009 *Plasma Sources Sci. Technol.* **18** 045025
[31] Pajdarová A D, Vlček J and Rezek J 2017 *J. Appl. Phys.* **121** 171908
[32] Yamauchi Y and Shimizu R 1983 *Japan. J. Appl. Phys.* **22** L227
[33] Phelps A V and Petrović Z L 1999 *Plasma Sources Sci. Technol.* **8** R21
[34] Aiempanakit M, Helmersson U, Aijaz A, Larsson P, Magnusson R, Jensen J and Kubart T 2011 *Surf. Coat. Technol.* **205** 4828
[35] Maszl C, Breilmann W, Benedikt J and von Keudell A 2014 *J. Phys. D: Appl. Phys.* **47** 224002
[36] JCPDS-ICDD 2015 *PDF-4 + Database* (Newton Square, PA: International Centre for Diffraction Data)
[37] Houska J 2016 *Surf. Coat. Technol.* **304** 23

F Significant improvement of the performance of $ZrO_2/V_{1-x}W_xO_2/ZrO_2$ thermochromic coatings by utilizing a second-order interference

J. Houska, **D. Kolenaty**, J. Vlcek, J. Rezek, T. Barta, S. Haviar

Sol. Energy Mater. Sol. Cells (submitted for publication)

Abstract

The paper deals with VO_2-based thermochromic coatings prepared by reactive magnetron sputtering. We combine four ways how to improve the coating performance and to increase its application potential. First, reactive high-power impulse magnetron sputtering with a pulsed O_2 flow control allowed us to prepare crystalline VO_2 of the correct stoichiometry under highly industry-friendly deposition conditions: without any substrate bias at a low deposition temperature of 330 °C. Second, doping of VO_2 by W (leading to $V_{1-x}W_xO_2$, with $x = 0.012$ in this work) allowed us to shift the thermochromic transition temperature towards the room temperature (39 °C in this work), without concessions in terms of coating properties. Third, we employ ZrO_2 antireflection layers both below and above the thermochromic $V_{1-x}W_xO_2$ layer, and present an optimum design of the resulting $ZrO_2/V_{1-x}W_xO_2/ZrO_2$ coatings. Most importantly, we show that while utilizing a first-order interference on ZrO_2 leads one to a tradeoff between the luminous transmittance (T_{lum}) and the modulation of the solar transmittance (ΔT_{sol}), utilizing a second-order interference allows one to optimize both T_{lum} and ΔT_{sol} in parallel. Fourth, the crystalline structure of the bottom ZrO_2 layer further improves the VO_2 crystallinity and the process reproducibility. The optimum experimental values of ZrO_2 thickness are in agreement with those predicted during the coating design. The results are important for the design and low-temperature fabrication of high-performance durable thermochromic VO_2-based coatings for smart window applications.

Keywords: VO_2; Thermochromic coatings; Antireflection layer; Doping; Low deposition temperature; HiPIMS

1 Introduction

Vanadium dioxide is a technologically important thin film material of a high current worldwide interest due to its reversible first-order thermochromic transition [1-3]. The transition takes place between a low-temperature semiconductive phase (monoclinic - distorted rutile - VO_2(M1) with the space group $P2_1/c$, No. 14) and a high-temperature metallic phase (tetragonal - perfect rutile - VO_2(R) with the space group $P4_2/mmm$, No. 136). The transition leads to temperature-dependent optical, electrical or thermal properties (infrared transmittance in the first place), which in turn leads to numerous technological applications (controlling the heat fluxes through smart windows in the first place) [4,5].

In addition to the overall efforts to maximize the luminous transmittance (T_{lum}) and the modulation of the solar transmittance (ΔT_{sol}), the research in the field of VO_2-based thermochromic coatings is focused on the following specific challenges. First, while numerous pathways for the deposition of VO_2 films have been reported [6-17], there are efforts to decrease the deposition temperature (T_{dep}) of crystalline VO_2 to ≤300 °C while keeping the other process conditions (e.g. no substrate bias) industry-friendly [6-10]. Low T_{dep} (i) facilitates the large-scale production by reducing the energy consumption and minimizing problems with temperature uniformity, (ii) limits the diffusion of harmful elements from substrates such

as soda-lime glass and (iii) allows deposition on temperature-sensitive plastic substrates. Second, there are efforts to shift the transition temperature (T_{tr}; 68 °C for bulk VO_2 [2]) towards the room temperature (RT) by doping of VO_2 by numerous other elements [18,19] such as W [20-23]. Third, the overall transmittance is being controlled by using antireflection (AR) layers of e.g. SiO_2 or SiO_x [24-29], TiO_2 [12,28,30-32], ZrO_2 [33] or Al_2O_3 [34]. The coating design can be not only bilayer but also multilayer (AR-layers both below and above the thermochromic layer(s)) [12,29,30]. Fourth, there are beneficial side-effects of the AR-layers (in some papers they even constitute the main motivation): enhanced durability of the coatings in the case of top AR-layers [35], and providing a crystalline template for the VO_2 growth in the case of bottom AR-layers [36-38].

However, the overall impression given by the literature is that while the available papers collectively constitute a significant progress in all the aforementioned directions, they often follow only one of the relevant priorities at once. In order to maximize the application potential of the coatings, it is necessary to avoid e.g. (i) optimizing only T_{lum} and ΔT_{sol}, regardless of T_{dep} and/or T_{tr}, (ii) decreasing T_{dep} at the cost of making the process significantly less industry-friendly, e.g. by introducing substrate bias voltage or post-deposition annealing, (iii) decreasing T_{tr} by doping at the cost of much lower ΔT_{sol}, or (iv) choosing the AR-layer thickness in order to optimize only T_{lum} (typically utilizing the first-order interference maximum, i.e. approximately quarter-wavelength layer), regardless of ΔT_{sol}. Thus, the aim of this paper is to combine all available ways how to improve the coating performance (decreasing T_{dep} by a deposition technique described in Sec. 2, decreasing T_{tr} by doping, increasing not only T_{lum} but also ΔT_{sol} by a multilayer design described in Sec. 3). We particularly focus on the optimum thickness of ZrO_2 AR-layers, and present the benefits of utilizing a second-order interference maximum.

2 Methodology

2.1 Overall strategy

The coatings were prepared by pulsed reactive magnetron sputtering on conventional soda-lime glass substrates (1 mm thick) without any substrate bias, at $T_{dep} \leq 330$ °C and base pressures below 10^{-4} Pa. Each coating consisted of bottom ZrO_2 AR-layer, middle $V_{1-x}W_xO_2$ thermochromic layer, and top ZrO_2 AR-layer. Properties and deposition rates of pure ZrO_2 and pure $V_{1-x}W_xO_2$ were obtained during preliminary depositions, allowing us to predict the transmittance during the coating design and to achieve the required thicknesses of all layers (Sec. 3.1) during the coating preparation. The coating properties were evaluated for three successively increasing thicknesses of the top ZrO_2 AR-layer, achieved by performing sets of three subsequent ZrO_2 depositions with the same bottom and middle layer. The deposition techniques are detailed in Secs. 2.2 ($V_{1-x}W_xO_2$) and 2.3 (ZrO_2).

2.2 $V_{1-x}W_xO_2$ preparation

The $V_{1-x}W_xO_2$ layers were prepared at $T_{dep} = 330$ °C by reactive high-power impulse magnetron sputtering (HiPIMS) in Ar+O_2, utilizing a feedback pulsed O_2 flow control [39]: the Ar flow rate was 60 sccm corresponding to a partial pressure of 1 Pa, while the O_2 flow rate, Φ_{ox}, was not fixed but pulsing between 0.6 and 1.5 sccm, and the duration of the Φ_{ox} pulses was decided during the deposition by a programmable logic controller using a pre-selected critical value of the discharge current in a period of the power supply. The depositions were performed in an ultra-high vacuum multi-magnetron sputter device (ATC 2200-V AJA International Inc.) equipped by two unbalanced magnetrons with planar targets of V and W (99.9% purity, diameter of 50 mm and thickness of 6 mm in both cases). The magnetron with a V target was driven by a high-power pulsed dc power supply (TruPlasma Highpulse 4002 TRUMPF Huettinger). The voltage pulse duration was 50 µs at the repetition frequency of 200 Hz (duty cycle of 1 %) and the deposition-averaged target power density (spatially averaged over the total target area) was close to 13 Wcm^{-2}. The magnetron with a W target was driven by an asymmetric pulsed dc power supply (IAP-1010 EN Technologies Inc.). The voltage pulse duration was 16 µs at the repetition frequency of 5 kHz (duty cycle of 8 %) and the deposition-averaged target power density was close to 24 $mWcm^{-2}$. Under these conditions, W content in the metal sublattice of $V_{1-x}W_xO_2$ (as measured on a dedicated 315 nm thick film in a scanning electron microscope (SU-70, Hitachi) using wave-dispersive spectroscopy (Magnaray, Thermo Scientific)) was 1.2 ± 0.1 at. % ($x = 0.012$).

2.3 ZrO_2 preparation

Both bottom and top ZrO_2 AR-layers were prepared without ohmic heating ($T_{dep} < 100$ °C) by dual reactive sine-wave mid-frequency ac magnetron sputtering in Ar+O_2, in an oxide mode: the Ar partial pressure was 1 Pa and the O_2 partial pressure was 0.35 Pa. The depositions were performed using two strongly unbalanced magnetrons with Zr targets (diameter of 100 mm and thickness of 6 mm) driven by a mid-frequency ac power supply (TruPlasma MF 3010, TRUMPF Huettinger). The oscillation frequency was close to 85 kHz and the deposition-averaged target power density was 15.5 Wcm^{-2}. See Ref. [40] for further details.

2.4 Coating characterization

The coating structure was characterized by X-ray diffraction (XRD) using the PANalytical X'Pert PRO instrument working with a CuKα (40 kV, 40 mA) radiation at a glancing incidence of 1°.

The coating transmittance was measured by spectrophotometry using the Agilent CARY 7000 instrument equipped with an in-house made heat/cool stage. The measurements were performed in the wave-

length (λ) range from 300 to 2500 nm at the normal angle of incidence and at a measurement temperature (T_m) both below and above T_{tr}. Below we present also the aforementioned integral quantities T_{lum} and T_{sol} defined as

$$T_{lum}(T_m) = \int_{380}^{780} \varphi_{lum}(\lambda)\varphi_{sol}(\lambda)T(\lambda,T_m)d\lambda \,/\, \int_{380}^{780} \varphi_{lum}(\lambda)\varphi_{sol}(\lambda)d\lambda \text{ and} \quad (1)$$

$$T_{sol}(T_m) = \int_{300}^{2500} \varphi_{sol}(\lambda)T(\lambda,T_m)d\lambda \,/\, \int_{300}^{2500} \varphi_{sol}(\lambda)d\lambda\,, \quad (2)$$

where φ_{lum} is the luminous sensitivity of the human eye and φ_{sol} is the sea-level solar irradiance spectrum [41]. The difference of T and T_{sol} values below and above T_{tr} is referred to as ΔT and ΔT_{sol}, respectively.

The thickness and optical constants (refractive index, n, and extinction coefficient, k) of individual layers were measured by spectroscopic ellipsometry using the J.A. Woollam Co. Inc. VASE instrument equipped by an Instec heat stage with the Instec STC200 controller. The measurements were performed at the angles of incidence of 55, 60 and 65° in reflection, again at T_m both below and above T_{tr}. The WVASE software was used (i) to fit the optical data during the measurements as well as (ii) to predict the coating transmittance during its design. In addition to the spectroscopic data, below we also provide values of T, ΔT, n and k at a specific λ given in the subscript, e.g. n_{550} for λ = 550 nm or ΔT_{2500} for λ = 2500 nm.

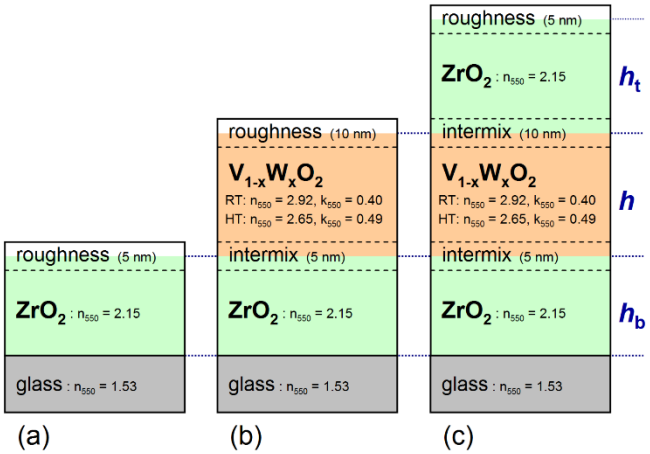

Figure 1. Optical model representing the individual stages of the coating preparation and used to predict the coating transmittance. Half of each surface roughness layer (top layer + void) contributes to the thickness of the corresponding top layer. The thickness of each expected intermix layer is given by a typical roughness of the layer below it, and contributes to the thicknesses of both corresponding layers. Selected optical constants, in the case of $V_{1-x}W_xO_2$ both below and above T_{tr} (RT and HT, respectively), are shown as well.

Figure 1 shows the optical model used. The model includes the glass substrate, bottom ZrO_2 layer (thickness h_b), $V_{1-x}W_xO_2$ layer (thickness h), top ZrO_2 layer (thickness h_t), surface roughness layer (typical measured roughness, used as exact roughness during the design, was 5 nm on ZrO_2 and 10 nm on $V_{1-x}W_xO_2$) and intermix layers (with a thickness given by the roughness of the corresponding bottom layer). ZrO_2 was described by the Cauchy dispersion formula, and $V_{1-x}W_xO_2$ was represented by a combination of the Cody-Lorentz dispersion formula (oscillator) with Lorentz oscillators.

3 Results and discussion

3.1 Coating design

The first quantity to note at the start of the coating design is n_{550} of the thermochromic layer. The room-temperature values include $n_{550} = 3.0 \pm 0.2$ for undoped VO_2 reported in the literature [7,8] [11,29,35-37], and $n_{550} = 2.92$ (at $k_{550} = 0.40$) for the slightly doped $V_{1-x}W_xO_2$ used in this work. Furthermore, n_{550} of the glass substrate is 1.53. Thus, the upper envelope of the interference curve $T(\lambda)$ can be moved as high as possible using AR-layers with $n_{550} = \sqrt{(2.92 \times 1.53)} = 2.11$ and $n_{550} = \sqrt{(2.92 \times 1.00)} = 1.71$ for the bottom and the top AR-layer, respectively (neglecting finite k_{550} and effects of the other optical boundaries present). This makes ZrO_2 (n_{550} around 2.15 in the present work) an ideal candidate for the bottom AR-layer, and an acceptable candidate for the top AR-layer. The former choice is further supported by the ability of ZrO_2 to crystallize (and in turn to support the nucleation of $V_{1-x}W_xO_2$) at low T_{dep}. This is contrary to other materials, such as Ta_2O_5, which exhibit n_{550} close to 2.1 but which require much higher T_{dep} to crystallize. The latter choice (using the same ZrO_2 also for the top AR-layer, instead of e.g. Al_2O_3 which has n_{550} closer to 1.7) can be justified as a trade-off between the coating characteristics and the simplicity of the coating preparation.

The choice of the material of the AR-layers ($n_{550} = 2.15$) has to be followed by optimizing their thicknesses, h_b and h_t. T_{lum} is highly correlated with T_{550}, which has maximum values ($T(\lambda)$ hits its upper envelope) for $h_{b,t} = \lambda/(4n_{550}) = 64$ nm, $(3\lambda)/(4n_{550}) = 192$ nm, etc. (again, neglecting finite k_{550} and effects of the other optical boundaries). The exact calculation of T_{lum}, without any neglections and averaged over values obtained using $V_{1-x}W_xO_2$ properties at T_m below (25 °C) and above (100 °C) the T_{tr} value of 39 °C (see Sec. 3.2), is shown in figure 2a. The exact optimum h_b and h_t values are lower that the aforementioned approximate optimum values: slightly above 40 nm and around 180 nm for the first and the second-order interference maximum, respectively.

It is necessary to say that the first-order interference maximum of T_{lum} has two clear, albeit quantitatively not decisive, advantages which probably lead to its usual preference: slightly higher value of the maximum (for $h = 50$ nm used in figure 2: $T_{lum} = 59.9\%$ at $h_b = h_t = 40$ nm compared to $T_{lum} = 57.2\%$ at $h_b = h_t = 180$ nm), and higher width of the maximum in terms of $\Delta h_{b,t}/h_{b,t}$ (allowing higher error of the deposition rate). However, the comparison of T_{lum} shown in figure 2a and ΔT_{sol} shown in figure 2b

reveals that while the first-order interference maximum of T_{lum} almost overlaps with an interference minimum of ΔT_{sol}, the second-order (with respect to both h_b and h_t) interference maximum of T_{lum} almost overlaps with an interference maximum of ΔT_{sol}. In other words, figure 2 shows that utilizing the second-order interference maximum of T_{lum} allows one to achieve much higher (about two times higher in this case) ΔT_{sol} at the cost of only slightly lower T_{lum}. This is the key statement of the present paper, further explained in the rest of this section and tested experimentally in the next section. Let us emphasize that the statement is valid in a wide range of h values and VO_2 or $V_{1-x}W_xO_2$ properties (not shown graphically: figure 2 would look about the same, at varied values corresponding to individual colors). Furthermore, the values presented in figure 2 are only weakly dependent on the surface roughness and the resulting intermix layers. For example, the values for the optimum $h_b = h_t = 180$ nm are $T_{lum} = 57.2\%$, 57.2% and 57.1% and $\Delta T_{sol} = 8.3\%$, 8.5% and 8.6% for the thickness of the relatively thickest intermix layer between $V_{1-x}W_xO_2$ and the top ZrO_2 of 5 nm, 10 nm (used in figure 2) and 15 nm, respectively.

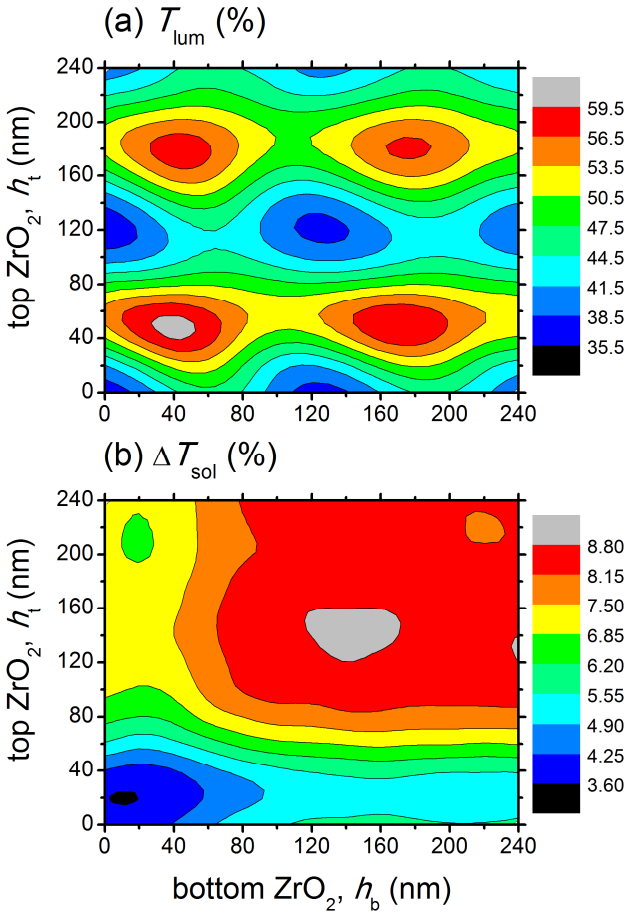

Figure 2. Calculated luminous transmittance (average of the similar T_{lum} values below (25 °C) and above (100 °C) T_{tr}; panel a) and modulation of the solar transmittance (difference of the T_{sol} values at below and above T_{tr}; panel b) for $h = 50$ nm as a function of h_b and h_t.

Figure 3, complementary to figure 2, shows the direct relationship between T_{lum} and ΔT_{sol}. It can be seen that for a given h_b, increasing h_t leads to a "lasso-like" dependence: the first-order maximum of $T_{lum}(h_t)$ is achieved close to the bottom end of the lasso, while the second order maximum of $T_{lum}(h_t)$ is achieved within its loop which is much higher in terms of ΔT_{sol}. In parallel, the maximum of $T_{lum}(h_b)$ (of any order) obviously moves the lasso to the right, while the transition from the first to the second-order maximum of $T_{lum}(h_b)$ moves the loop of the lasso up (to even higher ΔT_{sol}).

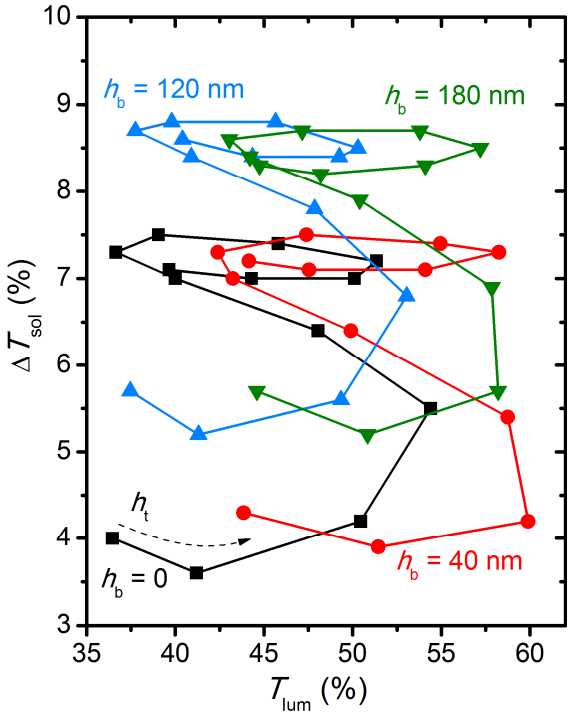

Figure 3. Calculated luminous transmittance (average of the similar T_{lum} values below (25 °C) and above (100 °C) T_{tr}) and modulation of the solar transmittance (difference of the T_{sol} values below and above T_{tr}). The data are shown for $h = 50$ nm, four representative h_b values (squares, balls, triangles up and triangles down for $h_b = 0$, 40, 120 and 180 nm, respectively) and 13 h_t values of 0 – 240 nm with a step of 20 nm (with $h_t = 0$ at the bottom left end of each dependence).

The spectroscopic dependencies which are behind T_{lum} and ΔT_{sol} are shown in figures 4a ($T(\lambda)$ below T_{tr}) and 4b ($T(\lambda)$ above T_{tr}). Even more importantly, the modulation of $T(\lambda)$ is shown in figure 4c. In the visible, figures 4a–b show that with increasing order of the interference maximum of T_{lum} the corresponding peak around $\lambda = 550$ nm is getting narrower. However, for the second-order maximum (with respect to both h_b and h_t) the peak is still wide compared to the peak of φ_{lum} which the transmittance is multiplied with (Eq. 1). In the infrared, figure 4 clearly shows that while the transition to the second-order interference maximum of T_{lum} improves the integral modulation ΔT_{sol}, it actually worsens ΔT_{2500} (the transition increases T_{2500} in itself, but more above than below T_{tr}). Thus, while it is certainly possible to use the dependence $T_{2500}(T_m)$ in order to identify T_{tr}, figure 4 shows how harmful it would be to follow a significant part of the literature and to use ΔT_{2500} instead of ΔT_{sol} as a criterion for the strength of the thermochromic effect.

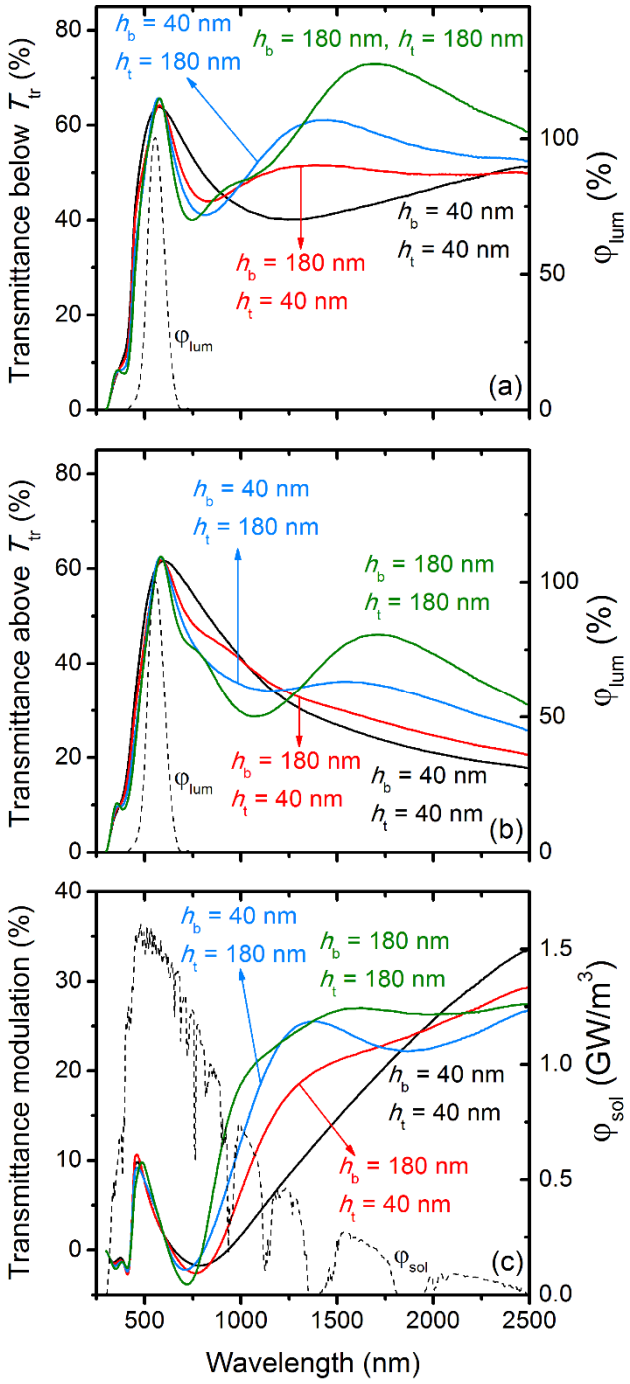

Figure 4. Calculated spectral transmittance $T(\lambda, T_m)$ for T_m below T_{tr} (25 °C; panel a) and above T_{tr} (100 °C; panel b) and its modulation (difference of the above values; panel c). The data are shown for h = 50 nm and four representative pairs of h_b and h_t values ($h_{b,t}$ = 40 or 180 nm). The luminous sensitivity of the human eye normalized to a maximum of 100% (φ_{lum}; panels a and b) and solar irradiance at the sea level for a Sun elevation of 41.81° above the horizon (φ_{sol}; panel c) are shown as well.

Figure 4c shows that the range of wavelengths which are indeed responsible for the ΔT_{sol} improvement resulting from the transition to the second-order interference maximum of T_{lum} is approximately 800 – 2000 nm. This can be understood by the fact that while thin (40 nm) AR-layers leading to first-order interference maxima in the visible have a limited effect on $T(\lambda)$ in the infrared, thick (180 nm) AR-layers

lead not only to second-order interference maxima in the visible but also, in parallel, to first-order interference maxima in the near infrared. The effect of the interference in the near infrared on $T(\lambda)$ below T_{tr} is stronger than that on $T(\lambda)$ above T_{tr}, because above T_{tr} (i) the $V_{1-x}W_xO_2$ absorption increases, reducing the effect of the bottom AR-layer, and (ii) the refractive index of $V_{1-x}W_xO_2$ in the near infrared decreases (much more than in the visible), i.e. moves towards that of ZrO_2, reducing the antireflection effect in itself. Note that in this wavelength range of 800 – 2000 nm the positive change of $\Delta T(\lambda)$ is multiplied by much higher φ_{sol} than the negative change of $\Delta T(\lambda)$ achieved at higher wavelengths such as 2500 nm.

3.2 Experimental verification

The experimental results in this section include two $ZrO_2/V_{1-x}W_xO_2/ZrO_2$ coatings (h = 76 or 49 nm). The round values of h_b and h_t provided throughout this section are those expected using the deposition rate of pure ZrO_2 and correspond to n_{550} = 2.15 used in the previous section. The h_b and h_t values obtained by ellipsometric characterization of multilayer coatings (thicknesses corresponding to measured n_{550} were converted to thicknesses corresponding to n_{550} = 2.15 by assuming a linear relationship between these quantities) were within the measurement error around the expected values (±6 nm; also within the dimensions of red areas in figure 2a).

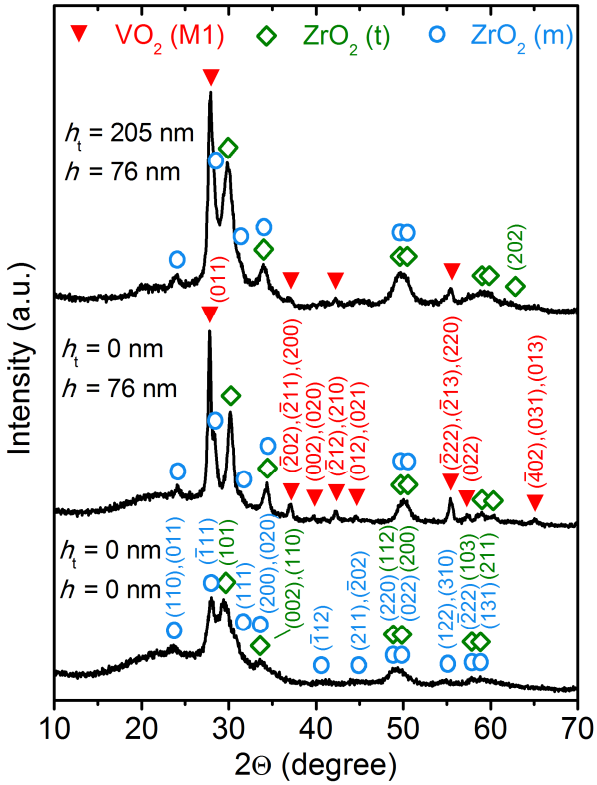

Figure 5. Spectra taken by glancing incidence XRD after the three stages of the coating preparation described in Sec. 2.1 and shown in figure 1: after the deposition of the bottom ZrO_2 layer (h_b = 180 nm; bottom line), after the deposition of the $V_{1-x}W_xO_2$ layer (h = 76 nm; middle line) and after the deposition of the thickest top ZrO_2 layer (h_t = 205 nm; top line). Miller indices corresponding to almost overlapping peaks are provided above each other.

Figure 5 confirms the expected crystallographic structure of one of the $ZrO_2/V_{1-x}W_xO_2/ZrO_2$ coatings prepared, including the structure evolution during the coating preparation.

- The bottom XRD pattern shows that the bottom ZrO_2 AR-layer consists of a mixture of m-ZrO_2 (PDF#04-013-6875 [42]; all peak positions and intensities obtained by the powder diffraction are referred to as theoretical ones throughout this section) and t-ZrO_2 (PDF#01-081-1544 valid for $ZrO_{1.95}$). For example, the strongest peaks around $2\Theta = 28.0°$ and 29.5° well correspond to the theoretically strongest peaks of m-ZrO_2 ((-111) planes diffracting at $2\Theta = 27.95°$) and t-ZrO_2 ((101) planes diffracting at $2\Theta = 29.81°$).

- The middle XRD pattern shows that the deposition of 76 nm thick $V_{1-x}W_xO_2$ led to a slight shift of the ZrO_2 peaks to higher angles (e.g. from 29.5° to 30.2° for the aforementioned strongest peak of t-ZrO_2), possibly due to a stress relaxation resulting from the effective annealing of ZrO_2 at the deposition temperature of $V_{1-x}W_xO_2$ (330 °C). In parallel, this pattern shows that the structure of $V_{1-x}W_xO_2$ indeed corresponds to the thermochromic $VO_2(M_1)$ phase (PDF#04-003-2035). For example, the strongest and sharp peak around $2\Theta = 27.8°$ exactly corresponds to the theoretically strongest peaks of $VO_2(M_1)$ ((011) planes diffracting at $2\Theta = 27.80°$). While the strongest peak of $VO_2(M_1)$ almost overlaps with that of m-ZrO_2, the relatively strongest non-overlapping peaks which newly appeared after the $V_{1-x}W_xO_2$ deposition around $2\Theta = 37.1°$, 42.3° and 55.4° well correspond to $VO_2(M_1)$ as well ((200), (210) and (220) planes diffracting at 37.10, 42.27 and 55.45°, respectively. The size of coherently diffracting domains, evaluated from the aforementioned strongest (011) peak, is 36 and 59 nm for $h = 49$ and 76 nm, respectively.

- The top XRD pattern confirms (i) that the structure of the top ZrO_2 AR-layer is similar to that of the bottom ZrO_2 AR-layer, and (ii) that the deposition of the top ZrO_2 AR-layer did not harm the structure of the $V_{1-x}W_xO_2$ layer.

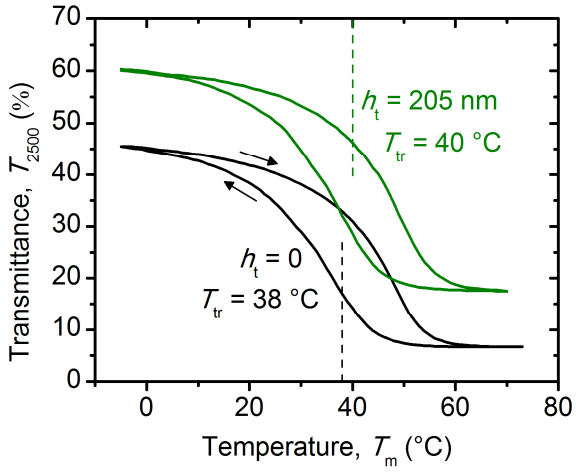

Figure 6. Temperature (T_m) dependence of the transmittance at $\lambda = 2500$ nm (T_{2500}). The data are shown for $h_b = 180$ nm, $h = 76$ nm and $h_t = 0$ or 205 nm. The transition temperatures (T_{tr}) corresponding to the middle of the hysteresis curves, both horizontally and vertically, are denoted as well.

Figure 6 examines the semiconductor-to-metal transition of 76 nm thick $V_{1-x}W_xO_2$ without a ZrO_2 AR-layer ($h_t = 0$; middle pattern in figure 5) and with the thickest considered ZrO_2 AR-layer ($h_t = 205$ nm; top pattern in figure 5). The purpose of this figure is twofold. First, the figure confirms the qualitative fact that the slight doping of VO_2 by W indeed allowed us to shift the transition temperature towards room temperature (the quantitative details concerning the relationship between the doping level and T_{tr} will be published separately). In particular, T_{tr} decreased from 68 °C (bulk VO_2 [2]) or 57 °C (VO_2 films prepared under the same conditions and reported in our previous works [6,7]) to 39 ± 1 °C, at high strength of the thermochromic transition (figure 7 below; contrary to previously reported harmful effect of W doping on ΔT_{sol} [21]). The gradient of (39-57)/1.2 = –15 K/at.% of W in the metal sublattice is consistent with e.g. Refs. [22] (–13 K/at.%) or [23] (–22 K/at.%). Second, the figure confirms that the deposition of the top ZrO_2 AR-layer did not harm the strength of the thermochromic transition or the T_{tr} value of 39 ± 1 °C.

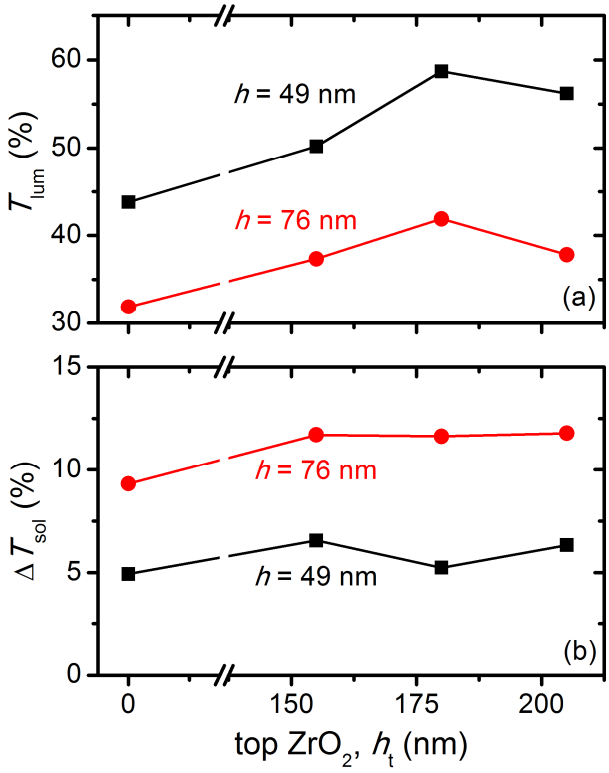

Figure 7. Experimental dependence of the luminous transmittance (T_{lum}, panel a) and modulation of the solar transmittance (ΔT_{sol}, panel b) of the $ZrO_2/V_{1-x}W_xO_2/ZrO_2$ coatings. The data are shown for $h_b = 180$ nm, $h = 49$ or 76 nm and $h_t = 0$, 155, 180 or 205 nm.

Figure 7 confirms that the second-order AR-layers indeed lead to a simultaneous improvement of experimental T_{lum} and ΔT_{sol} values. Two h values of 49 and 76 nm were used in order to demonstrate the application-dependent tradeoff between high T_{lum} (which requires low h) and high ΔT_{sol} (which requires high h). Let us emphasize that figure 7 shows results obtained using varied h_t at a fixed optimum $h_b = 180$ nm, i.e. it shows only that part of the overall improvement which the top AR-layer is responsible for. Qualitatively, figure 7a shows that $h_t = 180$ nm (middle of the red areas in figure 7a) indeed

leads to the highest T_{lum}, i.e. the figure confirms the correctness of the model used and prediction made in the previous section. In parallel, figure 7b shows that the top AR-layers indeed improved also ΔT_{sol} (let alone the slight drop for $h = 49$ nm and $h_t = 180$ nm which has to be ascribed to an experimental error). Quantitatively, the results achieved for the lower $h = 49$ nm include T_{lum} up to 59% (58.9% and 58.5% below and above T_{tr}, respectively) at ΔT_{sol} around 6%, while the results achieved for the higher $h = 76$ nm include T_{lum} up to 42% (43.9% and 40.0% below and above T_{tr}, respectively) at ΔT_{sol} around 12%. The fact that interference maxima of T_{lum} correspond to almost zero minimum values of the reflectance was cross-checked as well (for reflectance measured at the angle of incidence of 10°; not shown graphically). Let us recall that the presented T_{lum} and ΔT_{sol} values were achieved despite the W doping.

4 Conclusions

Thermochromic $ZrO_2/V_{1-x}W_xO_2/ZrO_2$ coatings with $x = 0.012$ were prepared by pulsed reactive magnetron sputtering on unbiased soda-lime glass substrates at low temperatures up to 330 °C. Coating design utilizing second-order interference layers in order to optimize both the luminous transmittance (T_{lum}) and the modulation of the solar transmittance (ΔT_{sol}) has been proposed. First examples of experimental results utilizing this design include T_{lum} up to 59% at ΔT_{sol} around 6% (for a $V_{1-x}W_xO_2$ thickness of 49 nm) or T_{lum} up to 42% at ΔT_{sol} around 12% ($V_{1-x}W_xO_2$ thickness of 76 nm). The possibility to simultaneously control the thermochromic transition temperature (39 °C in this work) by W doping has been demonstrated as well. The results show the potential of the aforementioned design of VO_2-based coatings for smart window applications, and confirm the possibility of their low-temperature fabrication.

Acknowledgment

This work was supported by the Czech Science Foundation under Project No. 17-08944S.

References

[1] Morin F J 1959 Oxides which show a metal-to-insulator transition at the neel temperature *Phys. Rev. Lett.* **3** 34–6

[2] Wriedt H A 1989 The O-V (Oxygen-Vanadium) System *Bull. Alloy Phase Diagrams* **10** 271–7

[3] Tomczak J M and Biermann S 2009 Optical properties of correlated materials – Or why intelligent windows may look dirty *Phys. Status Solidi B* **246** 1996–2005

[4] Hoffmann S, Lee E S and Clavero C 2014 Examination of the technical potential of near-infrared switching thermochromic windows for commercial building applications *Sol. Energy Mater. Sol. Cells* **123** 65–80

[5] Granqvist C G 2014 Oxide-based chromogenic coatings and devices for energy efficient fenestration: Brief survey and update on thermochromics and electrochromics *J. Vac. Sci. Technol. B* **32** 060801

[6] Vlček J, Kolenatý D, Houška J, Kozák T and Čerstvý R 2017 Controlled reactive HiPIMS-Effective technique for low-temperature (300 °C) synthesis of VO_2 films with semiconductor-to-metal transition *J. Phys. D. Appl. Phys.* **50** 38LT01

[7] Houska J, Kolenaty D, Vlcek J and Cerstvy R 2018 Properties of thermochromic VO_2 films prepared by HiPIMS onto unbiased amorphous glass substrates at a low temperature of 300 °C *Thin Solid Films* **660** 463–70

[8] Houska J, Kolenaty D, Rezek J and Vlcek J 2017 Characterization of thermochromic VO_2 (prepared at 250 °C) in a wide temperature range by spectroscopic ellipsometry *Appl. Surf. Sci.* **421** 529–34

[9] Vlček J, Kolenatý D, Kozák T, Houška J, Čapek J and Kos Š 2019 Ion-flux characteristics during low-temperature (300 °C) deposition of thermochromic VO_2 films using controlled reactive HiPIMS *J. Phys. D. Appl. Phys.* **52** 025205

[10] Choi Y, Jung Y and Kim H 2016 Low-temperature deposition of thermochromic VO_2 thin films on glass substrates *Thin Solid Films* **615** 437–45

[11] Fortier J-P, Baloukas B, Zabeida O, Klemberg-Sapieha J E and Martinu L 2014 Thermochromic VO_2 thin films deposited by HiPIMS *Sol. Energy Mater. Sol. Cells* **125** 291–6

[12] Mlyuka N R, Niklasson G A and Granqvist C G 2009 Thermochromic VO_2-based multilayer films with enhanced luminous transmittance and solar modulation *Phys. Status Solidi A* **206** 2155–60

[13] Aijaz A, Ji Y-X, Montero J, Niklasson G A, Granqvist C G and Kubart T 2016 Low-temperature synthesis of thermochromic vanadium dioxide thin films by reactive high power impulse magnetron sputtering *Sol. Energy Mater. Sol. Cells* **149** 137–44

[14] Azhan N H, Su K, Okimura K and Sakai J 2015 Radio frequency substrate biasing effects on the insulator-metal transition behavior of reactively sputtered VO_2 films on sapphire (001) *J. Appl. Phys.* **117** 185307

[15] Zhang D, Zhu M, Liu Y, Yang K, Liang G, Zheng Z, Cai X and Fan P 2016 High performance VO_2 thin films growth by DC magnetron sputtering at low temperature for smart energy efficient window application *J. Alloys Compd.* **659** 198–202

[16] Koo H, You H, Ko K E, Kwon O J, Chang S H and Park C 2013 Thermochromic properties of VO_2 thin film on SiN_x buffered glass substrate *Appl. Surf. Sci.* **277** 237–41

[17] Miller M J and Wang J 2015 Influence of grain size on transition temperature of thermochromic VO_2 *J. Appl. Phys.* **117** 034307

[18] Sun C, Yan L, Yue B, Liu H and Gao Y 2014 The modulation of metal-insulator transition temperature of vanadium dioxide: a density functional theory study *J. Mater. Chem. C* **2** 9283–93

[19] Li S-Y, Niklasson G a. and Granqvist C G 2012 Thermochromic fenestration with VO_2-based materials: Three challenges and how they can be met *Thin Solid Films* **520** 3823–8

[20] Shen N, Chen S, Chen Z, Liu X, Cao C, Dong B, Luo H, Liu J and Gao Y 2014 The synthesis and performance of Zr-doped and W–Zr-codoped VO_2 nanoparticles and derived flexible foils *J. Mater. Chem. A* **2** 15087–93

[21] Hu L, Tao H, Chen G, Pan R, Wan M, Xiong D and Zhao X 2016 Porous W-doped VO_2 films with simultaneously enhanced visible transparency and thermochromic properties *J. Sol-Gel Sci. Technol.* **77** 85–93

[22] Dietrich M K, Kuhl F, Polity A and Klar P J 2017 Optimizing thermochromic VO_2 by co-doping with W and Sr for smart window applications *Appl. Phys. Lett.* **110** 141907

[23] Romanyuk A, Steiner R, Marot L and Oelhafen P 2007 Temperature-induced metal-semiconductor transition in W-doped VO_2 films studied by photoelectron spectroscopy *Sol. Energy Mater. Sol. Cells* **91** 1831–5

[24] Kolenaty D, Houska J and Vlcek J 2018 Improved performance of thermochromic VO_2/SiO_2 coatings prepared by low-temperature pulsed reactive magnetron sputtering: Prediction and experimental verification *J. Alloys Compd.* **767** 46–51

[25] Lee M-H and Cho J-S 2000 Better thermochromic glazing of windows with anti-reflection coating *Thin Solid Films* **365** 5–6

[26] Chen X, Lv Q and Yi X 2012 Smart window coating based on nanostructured VO_2 thin film *Optik (Stuttg).* **123** 1187–9

[27] Li D, Shan Y, Huang F and Ding S 2014 Sol-gel preparation and characterization of SiO_2 coated VO_2 films with enhanced transmittance and high thermochromic performance *Appl. Surf. Sci.* **317** 160–6

[28] Chen Z, Gao Y, Kang L, Du J, Zhang Z, Luo H, Miao H and Tan G 2011 VO_2-based double-layered films for smart windows: Optical design, all-solution preparation and improved properties *Sol. Energy Mater. Sol. Cells* **95** 2677–84

[29] Kakiuchida H, Jin P and Tazawa M 2008 Control of thermochromic spectrum in vanadium dioxide by amorphous silicon suboxide layer *Sol. Energy Mater. Sol. Cells* **92** 1279–84

[30] Jin P, Xu G, Tazawa M and Yoshimura K 2003 Design, formation and characterization of a novel multifunctional window with VO_2 and TiO_2 coatings *Appl. Phys. A Mater. Sci. Process.* **77** 455-9

[31] Zhang Z, Gao Y, Luo H, Kang L, Chen Z, Du J, Kanehira M, Zhang Y and Wang Z L 2011 Solution-based fabrication of vanadium dioxide on F:SnO_2 substrates with largely enhanced thermochromism and low-emissivity for energy-saving applications *Energy Environ. Sci.* **4** 4290-7

[32] Wang H, He W, Yuan G, Wang X and Chen Q 2013 Large change of visible transmittance with VO_2 phase transition in VO_2/TiO_2 polycrystalline films *Thin Solid Films* **540** 168–72

[33] Xu G, Jin P, Tazawa M and Yoshimura K 2004 Optimization of antireflection coating for VO_2-based energy efficient window *Sol. Energy Mater. Sol. Cells* **83** 29–37

[34] Ji Y-X, Li S-Y, Niklasson G A and Granqvist C G 2014 Durability of thermochromic VO_2 thin films under heating and humidity: Effect of Al oxide top coatings *Thin Solid Films* **562** 568–73

[35] Loquai S, Baloukas B, Klemberg-Sapieha J E and Martinu L 2017 HiPIMS-deposited thermochromic VO_2 films with high environmental stability *Sol. Energy Mater. Sol. Cells* **160** 217–24

[36] Kakiuchida H, Jin P, Nakao S and Tazawa M 2007 Optical Properties of Vanadium Dioxide Film during Semiconductive-Metallic Phase Transition *Japanese J. Appl. Physics, Part 2 Lett.* **46** L113–L116

[37] Loquai S, Baloukas B, Zabeida O, Klemberg-Sapieha J E and Martinu L 2016 HiPIMS-deposited thermochromic VO_2 films on polymeric substrates *Sol. Energy Mater. Sol. Cells* **155** 60–9

[38] Chang T, Cao X, Li N, Long S, Gao X, Dedon L R, Sun G, Luo H and Jin P 2017 Facile and Low-Temperature Fabrication of Thermochromic Cr_2O_3/VO_2 Smart Coatings: Enhanced Solar Modulation Ability, High Luminous Transmittance and UV-Shielding Function *ACS Appl. Mater. Interfaces* **9** 26029–37

[39] Vlček J, Rezek J, Houška J, Čerstvý R and Bugyi R 2013 Process stabilization and a significant enhancement of the deposition rate in reactive high-power impulse magnetron sputtering of ZrO_2 and Ta_2O_5 films *Surf. Coatings Technol.* **236** 550–6

[40] Rezek J, Vlček J, Houška J, Čapek J and Baroch P 2018 Enhancement of the deposition rate in reactive mid-frequency ac magnetron sputtering of hard and optically transparent ZrO_2 films *Surf. Coatings Technol.* **336** 54–60

[41] available e.g. at http://rredc.nrel.gov/solar/spectra/am1.5/, http://hyperphysics.phy-astr.gsu.edu/hbase/vision/efficacy.html

[42] JCPDS-ICDD, PDF-4+ Database, International Centre for Diffraction Data, Newton Square, PA, USA, 2015

G High-performance thermochromic VO_2-based coatings prepared on glass by a low-temperature pulsed reactive magnetron sputter deposition

D. Kolenatý, J. Vlček, T. Bárta, J. Rezek, J. Houška, S. Haviar

(in preparation)

Abstract

The paper deals with thermochromic VO_2-based coatings prepared on soda-lime glass by pulsed reactive magnetron sputtering. We combine five ways how to improve the coating performance and to increase its application potential. First, reactive high-power impulse magnetron sputtering with a pulsed O_2 flow control was used to prepare crystalline VO_2 layers of the correct stoichiometry under highly industry-friendly deposition conditions: without any substrate bias at a low substrate temperature of 330 °C. Second, simultaneous doping of VO_2 by W (resulting in a $V_{1-x}W_xO_2$ composition with x = 0.018 in this work) was performed using a pulsed dc reactive magnetron sputtering to reduce the semiconductor-to-metal transition temperature to 20 °C without concessions in terms of coating properties. Third, ZrO_2 antireflection layers both below and above the thermochromic $V_{0.982}W_{0.018}O_2$ layers were deposited at a low substrate temperature (< 100 °C) by a dual reactive mid-frequency ac magnetron sputtering. A coating design utilizing a second-order interference on the ZrO_2 layers was proposed to optimize both the luminous transmittance, T_{lum}, and the modulation of the solar transmittance, ΔT_{sol}. Fourth, the crystalline structure of the bottom ZrO_2 layer further improved the VO_2 crystallinity and the process reproducibility. Fifth, the top ZrO_2 layer provided the mechanical and chemical (prevented contact with atmosphere) protection of the $V_{0.982}W_{0.018}O_2$ layers. We give the basic characteristics of the applied deposition technique and the proposed three-layer coatings with T_{lum} up to 60% at ΔT_{sol} close to 6% for a $V_{0.982}W_{0.018}O_2$ thickness of 45 nm, and with T_{lum} up to 50% at ΔT_{sol} above 10% for a $V_{0.982}W_{0.018}O_2$ thickness of 69 nm.

Main results (draft)

Figure 1:

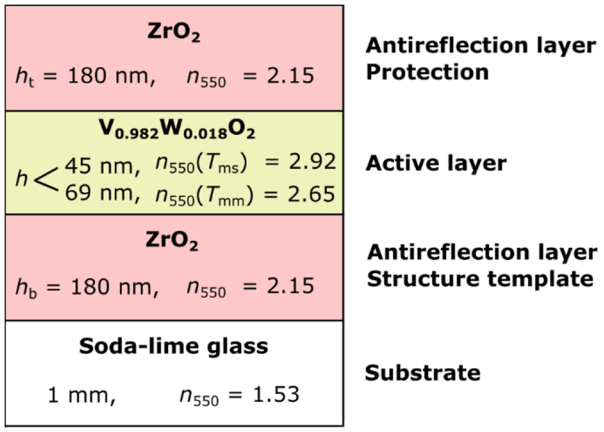

Figure 1. The three-layer thermochromic VO_2-based coating on a soda-lime glass substrate investigated in this paper. Here, h_b, h, and h_t represent the thickness of the bottom ZrO_2 layer, the thickness of the active $V_{0.982}W_{0.018}O_2$ layer, and the thickness of the top ZrO_2 layer, respectively. The refractive index at the wavelength of 550 nm, n_{550}, of all layers is also given. T_{ms} and T_{mm} denote the temperatures when the $V_{0.982}W_{0.018}O_2$ layer is in the semiconductive (below T_{tr}) and metallic (above T_{tr}) state, respectively.

Method:

Three-layer structure utilizing a second-order interference on the ZrO_2 layers was proposed (Part F) to optimize both the luminous transmittance, T_{lum}, and the modulation of the solar transmittance, ΔT_{sol}. The crystalline structure of the bottom ZrO_2 layer further improves the VO_2 crystallinity and the process reproducibility. The top ZrO_2 layer provides the mechanical and chemical (prevented contact with atmosphere) protection of the active $V_{0.982}W_{0.018}O_2$ layer. Figure 2 shows the discharge characteristics of the controlled reactive HiPIMS discharge which is combined with a simultaneous pulsed dc magnetron sputtering discharge to produce the $V_{0.982}W_{0.018}O_2$ layers. Both the bottom and top ZrO_2 antireflection layers were prepared without an ohmic heating ($T_s < 100$ °C) by dual reactive sine-wave mid-frequency ac magnetron sputtering in Ar+O_2: the Ar partial pressure was 1 Pa and the O_2 partial pressure was 0.35 Pa (oxide mode). The depositions were performed using two strongly unbalanced magnetrons with Zr targets (diameter of 100 mm and thickness of 6 mm) driven by a mid-frequency ac power supply (TruPlasma MF 3010, TRUMPF Huettinger). The oscillation frequency was close to 85 kHz and the deposition-averaged target power density was 15.5 Wcm^{-2}. See Ref. [1] for further details.

Figure 2:

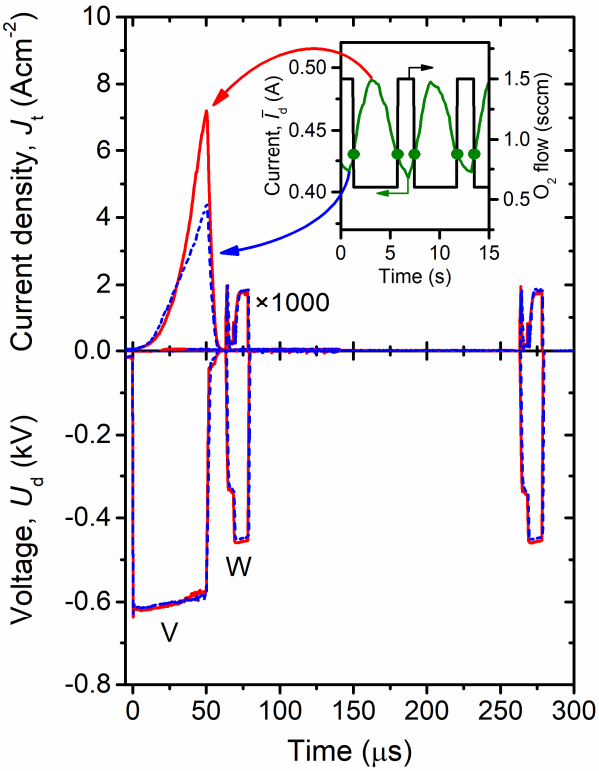

Figure 2. Waveforms of the magnetron voltage, U_d, and the target current density, J_t, for a preset deposition-averaged target power densities $<S_d>$ = 12.9 Wcm^{-2} and $<S_d>$ = 33 mWcm^{-2} for V and W target, respectively, during a deposition of the $V_{0.982}W_{0.018}O_2$ films (waveforms for W target are magnified 1000 times). Time evolution of the average discharge current in a period of the power supply, $\bar{I}_d$, during the deposition is shown in the inset. A pre-selected critical value $(\bar{I}_d)_{cr}$ = 0.43 A determining the switch between the oxygen flow rates Φ_{ox} = 0.6 sccm and Φ_{ox} = 1.5 sccm is marked by dots.

Method:

The $V_{0.982}W_{0.018}O_2$ layers were deposited without any substrate bias at a low substrate surface temperature of 330 °C by reactive HiPIMS, combined with a simultaneous standard pulsed magnetron sputtering, in Ar+O_2, utilizing a feedback pulsed O_2 flow control: the Ar flow rate was 60 sccm corresponding to a partial pressure of 1 Pa, while the O_2 flow rate, Φ_{ox}, was not fixed but pulsing between 0.6 and 1.5 sccm, and the duration of the Φ_{ox} pulses was decided during the deposition by a programmable logic controller using a pre-selected critical value of the discharge current in a period of the power supply, $\bar{I}_d$, (see figure 2). The depositions were performed in an ultra-high vacuum multi-magnetron sputter device (ATC 2200-V AJA International Inc.) using two unbalanced magnetrons with planar targets of V and W (99.9% purity, diameter of 50 mm and thickness of 6 mm in both cases). The magnetron with a V target was driven by a high-power pulsed dc power supply (TruPlasma Highpulse 4002 TRUMPF Huettinger). The voltage pulse duration was 50 μs at the repetition frequency of 200 Hz (duty cycle of 1%) and the deposition-averaged target power density (spatially averaged over the total target area) was 12.9 Wcm^{-2}.

The magnetron with a W target was driven by a pulsed dc power supply (IAP-1010 EN Technologies Inc.). The voltage pulse duration was 16 µs at the repetition frequency of 5 kHz (duty cycle of 8%) and the deposition-averaged target power density was 33 mWcm^{-2}. A great potential of the controlled reactive HiPIMS for a low-temperature compatible fabrication of high-performance durable thermochromic VO_2-based coatings for smart-window applications is presented in Part E.

Result:

Under these conditions, the W content in the metal sublattice of $V_{1-x}W_xO_2$ (as measured on a dedicated 285 nm thick film in a scanning electron microscope (SU-70, Hitachi) using wave-dispersive spectroscopy (Magnaray, Thermo Scientific)) was 1.8 ± 0.6 at. % (i.e., $x = 0.018$).

Figure 3:

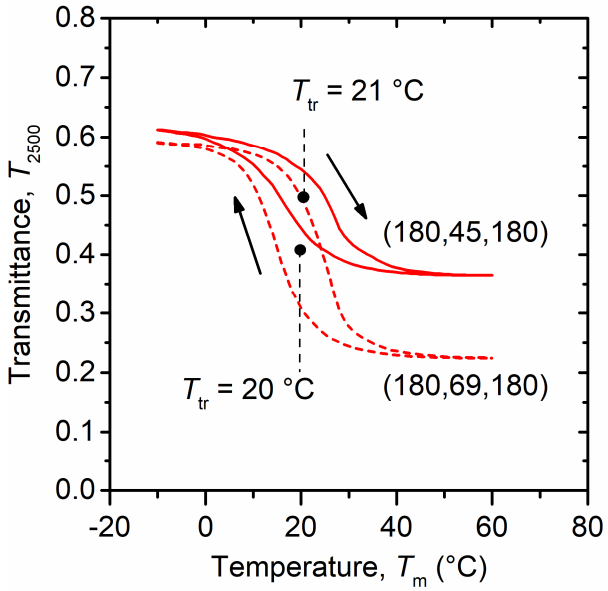

Figure 3. Temperature (T_m) dependence of the transmittance at 2500 nm for the $ZrO_2/V_{0.982}W_{0.018}O_2/ZrO_2$ coatings with $h_b = 180$ nm, $h = 45$ nm or 69 nm, and $h_t = 180$ nm deposited onto 1 mm thick glass substrates (figure 1). The transition temperatures, T_{tr}, are also given.

Method:

The temperature dependence of the normal-incidence optical transmittance for the wavelength of 2500 nm, T_{2500}, was measured in the range of the sample temperatures, T_m, from $T_{ms} = -10$ °C to $T_{mm} = 60$ °C using a spectrophotometer (Agilent Cary 7000) with an in-house made heat/cool cell.

Result:

Figure 3 shows the temperature (T_m) dependence of the transmittance at $\lambda = 2500$ nm, T_{2500}. The evaluated transition temperatures of the $ZrO_2/V_{0.982}W_{0.018}O_2/ZrO_2$ coatings were reduced by the aforementioned admixture of W to $T_{tr} = 20 - 21$ °C. This is in agreement with the requirement of the comfort temperature range 20 – 25 °C [2] for smart-window applications.

Figure 4:

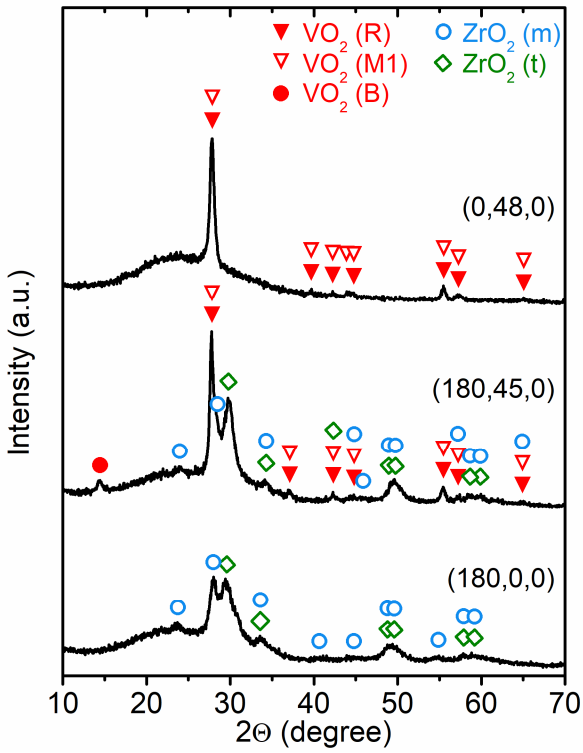

Figure 4. X-ray diffraction patterns taken at $T_m = 25$ °C from the $V_{0.982}W_{0.018}O_2$ layers with the thickness $h = 48$ nm deposited onto glass (denoted as (0,48,0)) and with the thickness $h = 45$ nm deposited onto the ZrO_2 layer with the thickness $h_b = 180$ nm on glass (denoted as (180,45,0)). For comparison, the x-ray diffraction pattern from the ZrO_2 layer with the thickness $h_b = 180$ nm on glass (denoted as (180,0,0)) is given. The main diffraction peaks of VO_2(R), VO_2(M1), VO_2(B), ZrO_2(m) and ZrO_2(t) are marked.

Method:

For structural investigation of the films, x-ray diffraction (XRD) measurements were carried out using a PANalytical X´Pert PRO diffractometer working with a CuKα (40kV, 40 mA) radiation at a glancing incidence of 1°. The average size of coherently diffracting regions of the VO_2(R)/VO_2(M1) phase was estimated from the full width at half maximum of the main VO_2(R)/VO_2(M1) diffraction peak, corrected for instrumental broadening, using the Scherrer's equation.

Result:

As is seen in figure 4, the bottom ZrO_2 antireflection layer (denoted as (180,0,0)) consists of a mixture of m-ZrO_2 (PDF#04-013-6875 [3]; all peak positions and intensities obtained by the powder diffraction are referred to as theoretical ones throughout this section) and t-ZrO_2 (PDF#01-081-1544 valid for $ZrO_{1.95}$). For example, the strongest peaks around $2\Theta = 28.0°$ and 29.5° well correspond to the theoretically strongest peaks of m-ZrO_2 ((–111) planes diffracting at $2\Theta = 27.95°$) and t-ZrO_2 ((101) planes diffracting at $2\Theta = 29.81°$). The $V_{0.982}W_{0.018}O_2$ layer with T_{tr} = 23 °C (table 1) deposited onto glass (denoted as (0,48,0)) and the $V_{0.982}W_{0.018}O_2$ layer with T_{tr} = 20 °C deposited onto the crystalline ZrO_2 layer (denoted as (180,45,0)) consist of a mixture of the thermochromic VO_2(R) (PDF#01-073-2362) and $VO_2(M_1)$ (PDF#04-003-2035) phases, which are hard to distinguish. For example, the strongest and sharp peak around $2\Theta = 27.8°$ well corresponds to the theoretically strongest peaks of the VO_2(R), (110) planes diffracting at $2\Theta = 27.91°$, and the $VO_2(M_1)$, (011) planes diffracting at $2\Theta = 27.80°$. In spite of a small content of the non-thermochromic VO_2(B) phase (PDF#01-084-3056), the $V_{0.982}W_{0.018}O_2$ layer on the crystalline ZrO_2 layer exhibited a better crystallinity of the thermochromic VO_2(R)/VO_2(M1) phase. This was demonstrated by a larger size of the coherently diffracting regions of 47 nm compared with 23 nm for the $V_{0.982}W_{0.018}O_2$ layer on glass.

Figure 5:

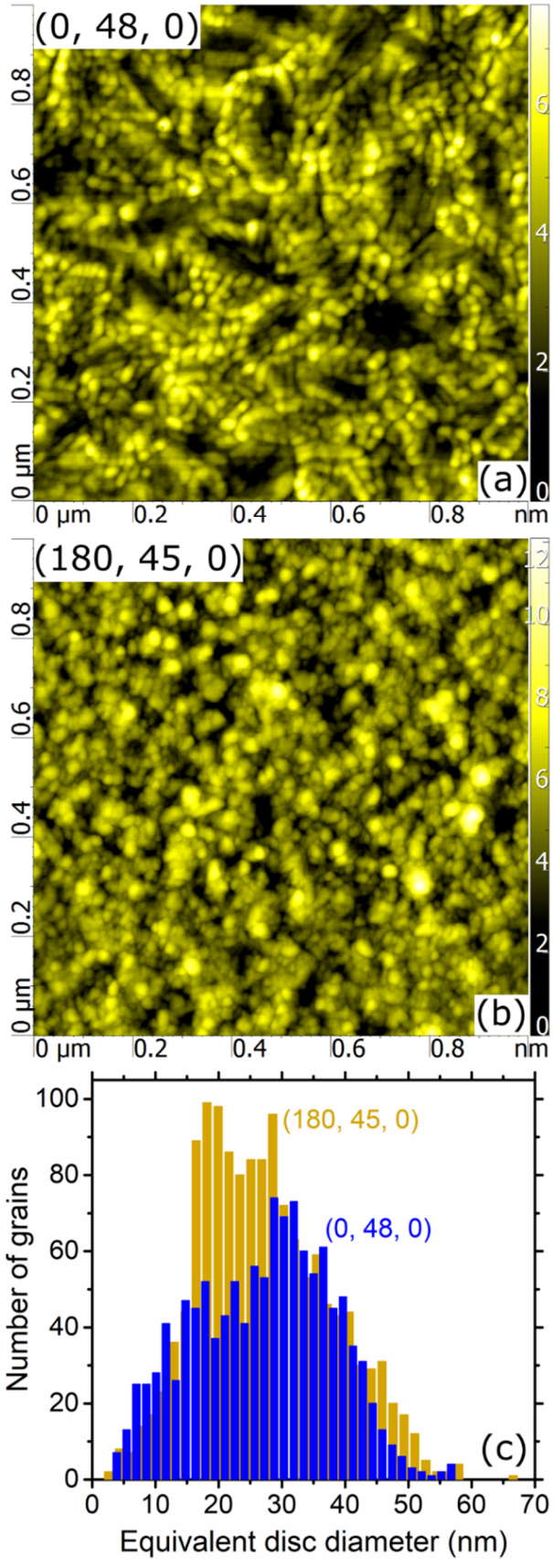

Figure 5. Surface morphology of the $V_{0.982}W_{0.018}O_2$ layers with the thickness h = 48 nm deposited onto glass (denoted as (0,48,0); panel a) and with the thickness h = 45 nm deposited onto the ZrO_2 layer with the thickness h_b = 180 nm on glass (denoted as (180,45,0); paned b), together with the corresponding grain-size (approximated by an equivalent disc diameter) distributions on the area of 1 × 1 µm^2; panel c.

Method:

The surface morphology of the films was determined by atomic force microscopy (AFM) using a SmartSPM Microscope (AIST-NT) with a diamond tip (nominal radius below 10 nm) in a semicontact mode. The root-mean-square roughness of the surface, R_{rms}, was computed from a randomly selected square area of 1×1 μm^2. The AFM images were processed by Gwyddion 2.41 software [4], and implemented "watershed" method was used for grain analysis. The grains identified were approximated by an equivalent disc diameter with the same projected area as the grain.

Result:

The surface morphology of the $V_{0.982}W_{0.018}O_2$ layers is shown in figure 5. One can see that the grains identified by the "watershed" method make up 94% of the projected surface area for the $V_{0.982}W_{0.018}O_2$ layer ($R_{rms} = 1.2$ nm) deposited onto the crystalline ZrO_2 layer (figure 4) whereas they make up 80% for the $V_{0.982}W_{0.018}O_2$ layer ($R_{rms} = 1.1$ nm) deposited onto the bare soda-lime glass. Also the distribution of the grain size is narrower for the former layer than for the latter layer. Both of these results of the morphology analysis are related to the crystallinity of the substrate.

Figures 6 – 7 and Table 1:

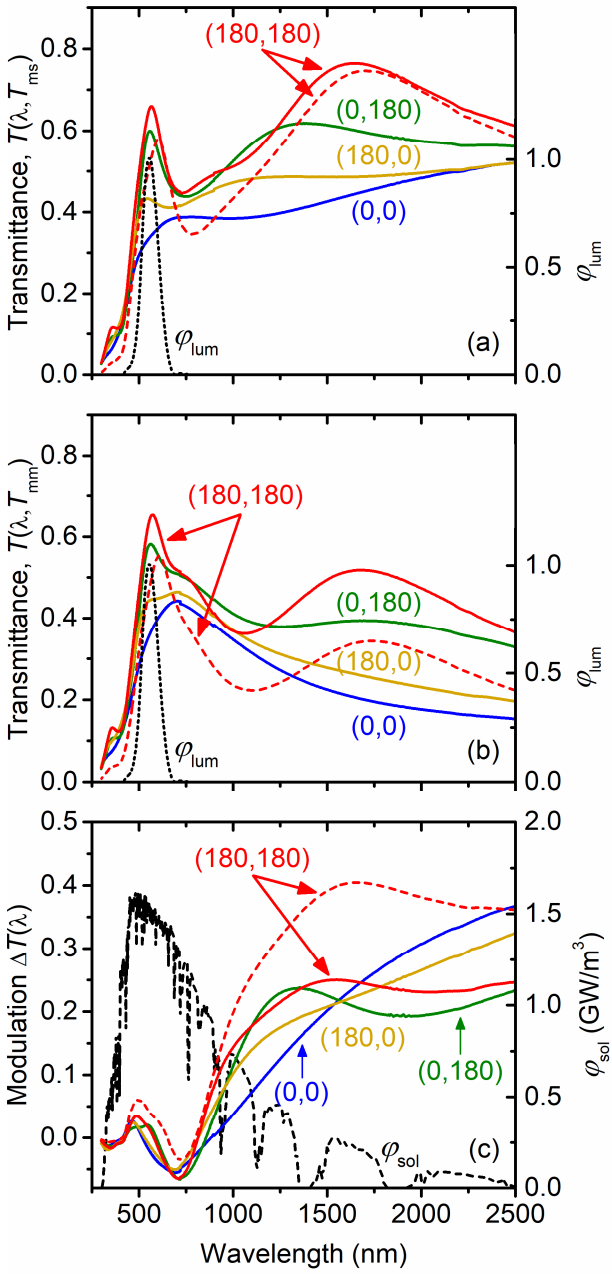

Figure 6. Spectral transmittance $T(\lambda, T_m)$ of different configurations (table 1) of the thermochromic VO_2-based coatings on 1 mm thick glass substrates measured at $T_{ms} = -5$ °C (panel a) and $T_{mm} = 60$ °C (panel b), together with the corresponding modulation of the transmittance $\Delta T(\lambda)$; panel c. The coatings are denoted as (h_b, h_t), where h_b and h_t are the thicknesses of the bottom and top ZrO_2 layers, respectively. The thickness of the $V_{0.982}W_{0.018}O_2$ layer is $h = 45 - 48$ nm (solid lines) or $h = 69$ nm (dashed lines). The luminous sensitivity of the human eye, φ_{lum}, normalized to 1, and the sea-level solar irradiance spectrum, φ_{sol}, are also given.

Table 1. Thermochromic properties of different configurations of the VO_2-based coatings on 1 mm thick glass substrates. Here, h is the thickness of the $V_{0.982}W_{0.018}O_2$ layer, and h_b and h_t are thicknesses of the bottom and top ZrO_2 layers, respectively.

h (nm)	h_b (nm)	h_t (nm)	T_{tr} (°C)	$T_{lum}(T_{ms})$ (%)	$T_{lum}(T_{mm})$ (%)	ΔT_{lum} (%)	$T_{sol}(T_{ms})$ (%)	$T_{sol}(T_{mm})$ (%)	ΔT_{sol} (%)
48	0	0	23	33.5	35.5	–2.0	34.6	31.7	2.9
45	180	0	20	41.8	43.1	–1.3	40.4	36.1	4.3
48	0	180	25	54.3	53.5	0.8	46.3	41.8	4.5
45	180	180	21	59.7	59.1	0.6	49.9	44.4	5.5
69	180	180	20	49.9	46.0	3.9	42.4	32.0	10.4

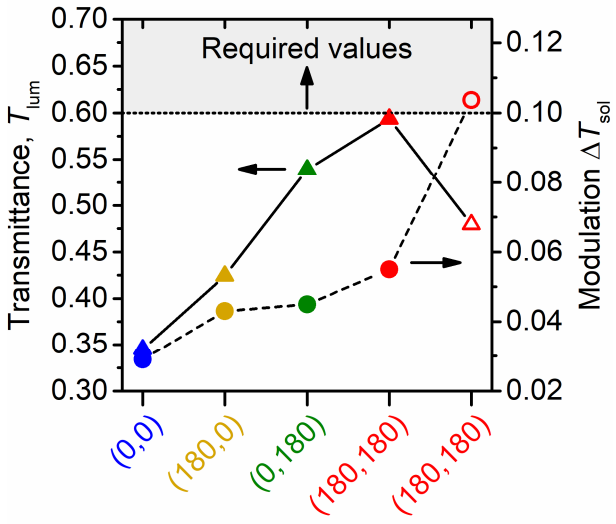

Figure 7. The average luminous transmittance, T_{lum}, and the modulation of the solar transmittance, ΔT_{sol}, of different configurations (table 1) of the thermochromic VO_2-based coatings on 1 mm thick glass substrates. The coatings are denoted as (h_b, h_t), where h_b and h_t are thicknesses of the bottom and top ZrO_2 layers, respectively. The thickness of the $V_{0.982}W_{0.018}O_2$ layer is $h = 45 - 48$ nm (full symbols) or $h = 69$ nm (empty symbols). The grey region represents the required values for smart-window applications.

Method:

The coating transmittance was measured by spectrophotometry using the Agilent CARY 7000 instrument equipped with an in-house made heat/cool cell. The measurements were performed in the wavelength range from 300 to 2500 nm for the normal angle of incidence at the temperatures $T_{ms} = -5$ °C (below T_{tr}) and $T_{mm} = 60$ °C (above T_{tr}). The luminous transmittance, T_{lum}, and the solar transmittance, T_{sol}, are defined as follows

$$T_{\mathrm{lum}}(T_{\mathrm{m}}) = \int_{380}^{780} \varphi_{\mathrm{lum}}(\lambda)\varphi_{\mathrm{sol}}(\lambda)T(\lambda, T_{\mathrm{m}})d\lambda \,/\, \int_{380}^{780} \varphi_{\mathrm{lum}}(\lambda)\varphi_{\mathrm{sol}}(\lambda)d\lambda\,, \tag{1}$$

$$T_{\mathrm{sol}}(T_{\mathrm{m}}) = \int_{300}^{2500} \varphi_{\mathrm{sol}}(\lambda)T(\lambda, T_{\mathrm{m}})d\lambda \,/\, \int_{300}^{2500} \varphi_{\mathrm{sol}}(\lambda)d\lambda\,, \tag{2}$$

where φ_{lum} is the luminous sensitivity of the human eye and φ_{sol} is the sea-level solar irradiance spectrum at an air mass of 1.5 [5]. The modulation of the luminous transmittance, ΔT_{lum}, and of the solar transmittance, ΔT_{sol}, are defined as

$$\Delta T_{\mathrm{lum}} = T_{\mathrm{lum}}(T_{\mathrm{ms}}) - T_{\mathrm{lum}}(T_{\mathrm{mm}}) \quad \text{and} \tag{3}$$

$$\Delta T_{\mathrm{sol}} = T_{\mathrm{sol}}(T_{\mathrm{ms}}) - T_{\mathrm{sol}}(T_{\mathrm{mm}})\,. \tag{4}$$

Using relation (4) it can be written

$$\Delta T_{\mathrm{sol}} = \int_{300}^{2500} \varphi_{\mathrm{sol}}(\lambda)\Delta T(\lambda)d\lambda \,/\, \int_{300}^{2500} \varphi_{\mathrm{sol}}(\lambda)d\lambda\,, \tag{5}$$

where $\Delta T(\lambda) = T(\lambda,\ T_{\mathrm{ms}}) - T(\lambda,\ T_{\mathrm{mm}})$ is the modulation of the transmittance at the wavelength λ. The average luminous transmittance, T_{lum}, is defined as $T_{\mathrm{lum}} = [\,T_{\mathrm{lum}}(T_{\mathrm{ms}}) + T_{\mathrm{lum}}(T_{\mathrm{mm}})]/2$.

Result:

Figure 7 and table 1 show a gradual improvement of the optical performance (average T_{lum} and ΔT_{sol}) of the VO_2-based coatings with introducing the bottom and top ZrO_2 antireflection layers at almost the same thickness (45 – 48 nm) of the $V_{0.982}W_{0.018}O_2$ layer (full symbols). The three-layer configuration with $h = 45$ nm, and $h_{\mathrm{b}} = h_{\mathrm{t}} = 180$ nm led to the best result: $T_{\mathrm{lum}} = 59.4\%$ and $\Delta T_{\mathrm{sol}} = 5.5\%$. The increase in the thickness of the $V_{0.982}W_{0.018}O_2$ layer up to $h = 69$ nm (empty symbols) resulted in $T_{\mathrm{lum}} = 48.0\%$ and $\Delta T_{\mathrm{sol}} = 10.4\%$. It is possible to state that our results are close to the requirements for smart-window applications (see figure 7).

Table 2:

Table 2. Comparison between this work and previously reported studies on T_{lum} and ΔT_{sol} of VO_2-based coatings with $T_{tr} \leq 40$ °C prepared on glass substrates. $(T_s)_{max}$ is the maximum substrate (glass) temperature during the preparation of the coatings and h is the thickness of the active VO_2-based layer. Here, ACMS, RFMS and DCMS denote the ac, rf and dc magnetron sputtering, respectively.

$(T_s)_{max}$ (°C)	T_{tr} (°C)	$T_{lum}(T_{ms})$ (%)	$T_{lum}(T_{mm})$ (%)	ΔT_{sol} (%)	h (nm)	Preparation Method	Ref.
330	20	49.9	46.0	10.4	69	HiPIMS + ACMS	This Work
330	21	59.7	59.1	5.5	45	HiPIMS + ACMS	This Work
330	40	43.9	40.0	11.6	76	HiPIMS + ACMS	[6]
400	32	60.9	65.0	3.6	Nanop.	Hydroth. + Anneal.	[7]
450	29	61.8	61.0	5.2	100	RFMS	[8]
450	34	36.2	32.3	14.6	145	DCMS + Anneal.	[9]
450	38	45.2	39.0	12.8	150	DCMS + Anneal.	[10]
500*	28	44.6	45.7	6.9	100	Sol-Gel + Anneal.	[11]
600$^+$	35	71.6	70.1	8.6	392	Sol-Gel + Anneal.	[12]

*: silica substrate, $^+$: fused-quartz substrate

Result:

Based on the comparison of our results obtained for the thermochromic VO_2-based coatings prepared on glass with the newest (best) results in the literature, it can be stated that we achieved an excellent combination of the required characteristics: the lowest maximum substrate (glass) temperature during the preparation of the coatings $(T_s)_{max} = 330$°C, an appropriate transition temperature $T_{tr} = 20 – 25$ °C, and T_{lum} up to 60% at ΔT_{sol} close to 6% or T_{lum} up to 50% at ΔT_{sol} above 10%.

4 Conclusions

High-performance thermochromic $ZrO_2/V_{0.982}W_{0.018}O_2/ZrO_2$ coatings were prepared by pulsed reactive magnetron sputtering on soda-lime glass under highly industry-friendly deposition conditions: without any substrate bias and at a low substrate temperature of 330 °C. Reactive high-power impulse magnetron sputtering with a pulsed O_2 flow control was used to prepare crystalline VO_2 layers of the correct stoichiometry. Simultaneous doping of VO_2 by W was performed using a pulsed dc reactive magnetron sputtering to reduce the transition temperature to 20 °C without concessions in terms of coating properties. A coating design utilizing a second-order interference on the ZrO_2 layers optimized the luminous transmittance, T_{lum}, up to 60% at the modulation of the solar transmittance, ΔT_{sol}, close to 6% for a $V_{0.982}W_{0.018}O_2$ thickness of 45 nm, and up to 50% at ΔT_{sol} above 10% for a $V_{0.982}W_{0.018}O_2$ thickness of 69 nm. Moreover, the crystalline structure of the bottom ZrO_2 layer further improved the VO_2 crystallinity and the process reproducibility, and the top ZrO_2 layer provided the mechanical and chemical (prevented contact with atmosphere) protection of the $V_{0.982}W_{0.018}O_2$ layers. Based on the comparison of our results obtained for the thermochromic VO_2-based coatings prepared on glass with the newest results in the literature, it can be stated that we achieved an excellent combination of the required characteristics: the lowest maximum substrate (glass) temperature during the preparation of the coatings $(T_s)_{max}$ = 330°C, an appropriate transition temperature T_{tr} = 20 – 25 °C, and T_{lum} up to 60% at ΔT_{sol} close to 6% or T_{lum} up to 50% at ΔT_{sol} above 10%.

References

[1] Vlček J, Rezek J, Houška J, Čerstvý R and Bugyi R 2013 Process stabilization and a significant enhancement of the deposition rate in reactive high-power impulse magnetron sputtering of ZrO_2 and Ta_2O_5 films *Surf. Coatings Technol.* **236** 550–6

[2] Saeli M, Piccirllo C, Warwick M and Binions R 2013 Thermochromic Thin Films: Synthesis, Properties and Energy Consumption Modelling *Mater. Process. energy Commun. Curr. Res. Technol. Dev.* 736–46

[3] JCPDS-ICDD, PDF-4+ Database, International Centre for Diffraction Data, Newton Square, PA, USA, 2015

[4] Nečas D and Klapetek P 2012 Gwyddion: An open-source software for SPM data analysis *Cent. Eur. J. Phys.* **10** 181–8

[5] available e.g. at http://rredc.nrel.gov/solar/spectra/am1.5/, http://hyperphysics.phy-astr.gsu.edu/hbase/vision/efficacy.html

[6] Houska J, Kolenaty D, Vlcek J, Barta T, Rezek J and Cerstvy R Significant improvement of the performance of $ZrO_2/V_{1-x}W_xO_2/ZrO_2$ thermochromic coatings by utilizing a second-order interference *Sol. Energy Mater. Sol. Cells* (submitted)

[7] Wang N, Goh Q S, Lee P L, Magdassi S and Long Y 2017 One-step hydrothermal synthesis of rare earth/W-codoped VO_2 nanoparticles: Reduced phase transition temperature and improved thermochromic properties *J. Alloys Compd.* **711** 222–8

[8] Dietrich M K, Kuhl F, Polity A and Klar P J 2017 Optimizing thermochromic VO_2 by co-doping with W and Sr for smart window applications *Appl. Phys. Lett.* **110** 141907

[9] Lu L, Wu Z, Ji C, Song M, Feng H, Ma X and Jiang Y 2018 Effect of Fe doping on thermochromic properties of VO_2 films *J. Mater. Sci. Mater. Electron.* **29** 5501–8

[10] Ji C, Wu Z, Lu L, Wu X, Wang J, Liu X, Zhou H, Huang Z, Gou J and Jiang Y 2018 High thermochromic performance of Fe/Mg co-doped VO_2 thin films for smart window applications *J. Mater. Chem. C* **00** 1–3

[11] Hu L, Tao H, Chen G, Pan R, Wan M, Xiong D and Zhao X 2016 Porous W-doped VO_2 films with simultaneously enhanced visible transparency and thermochromic properties *J. Sol-Gel Sci. Technol.* **77** 85–93

[12] Liang Z, Zhao L, Meng W, Zhong C, Wei S, Dong B, Xu Z, Wan L and Wang S 2017 Tungsten-doped vanadium dioxide thin films as smart windows with self-cleaning and energy-saving functions *J. Alloys Compd.* **694** 124–31

IV Conclusions of the thesis

This Ph.D. thesis deals with preparation and characterization of thermochromic VO_2-based coatings. They were deposited using a pulsed reactive magnetron sputtering onto floating substrates at low substrate temperatures (less than 330 °C). The results presented in chapter III fulfil all the aims formulated. The results are summarized as follows:

1. The first aim was fulfilled in the part A. Thermochromic VO_2 films were prepared on crystalline Si (100) substrates by a controlled reactive high-power impulse magnetron sputtering with the to-substrate O_2 injection into the high-density plasma in front of the sputtered V target at a very low deposition temperature 250 °C and without any substrate bias voltage, i.e. under conditions which maximize their application potential. The film properties were studied in a wide temperature range (–30 °C to 100 °C) by spectroscopic ellipsometry. The most important properties are: the room temperature extinction coefficient of 0.10 at 550 nm, and the transmittance at 2000 nm (calculated for a 100 nm thick film on glass) of 39% at –30°C, 30% at room temperature and 3.4% above the transition temperature. The transition temperature during the cooling part of the cycle for the quantities $\boldsymbol{\Psi}$, k and calculated T is 41 °C, < 50 °C and < 40 °C, respectively (half of the total change) or 50 °C, 50 °C and 45 °C, respectively (inflection point of the temperature dependence). The hysteresis curve width at the transition temperature is 6 – 8 °C.

2. The second aim was fulfilled in the parts B, C and E. The VO_2 films with a pronounced semiconductor-to-metal transition were prepared on conventional soda-lime glass substrates using the controlled reactive HiPIMS with the to-substrate O_2 injection into the high-density plasma in front of the sputtered V target under exceptionally industry-friendly conditions: at low substrate surface temperature $T_s = 300$ °C, without any substrate bias voltage and without any interlayer. It was shown that the phase composition of the films correlates with the $(V^+ + V^{2+})$ ion fraction and the $(V^+ + V^{2+}):(2O_2^+ + O^+)$ ion ratio in the total ion flux onto the substrate, which are given by a voltage pulse duration and by a pre-selected $(p_{ox})_{cr}$ determining the range of the p_{ox} oscillating during the deposition. The VO_2 films (88 nm thick) with the pronounced semiconductor-to-metal transition characterized by a high modulation of the transmittance at 2500 nm (between 51% and 8%) and of the electrical resistivity (changed 350 times) were synthesized at the controlled p_{ox} oscillations around $(p_{ox})_{cr} = 15$ mPa with the maximum target power density $(S_d)_{max}$ of up to 5kWcm^{-2} during 50 μs voltage pulses at the duty cycle of 1% (repetition frequency of 200 Hz and deposition-averaged target power density close to 13 Wcm^{-2}). Under these conditions, an appropriate composition of the total ion flux and high ion energies (up to 50 eV relative to ground potential) support the crystallization of the thermochromic phase (VO_2(R) during the deposition and VO_2(M1) at room temperature) in the VO_2 films deposited at $T_s = 300$ °C onto

conventional soda-lime glass substrates without any substrate bias voltage and without any interlayer. We have thus demonstrated a great potential of the controlled reactive HiPIMS for a low-temperature compatible fabrication of high-performance durable thermochromic VO_2-based coatings for smart-window applications.

3. The third aim was fulfilled in the part D. Thermochromic VO_2 layers of two different thicknesses were deposited on soda-lime glass substrates by reactive HiPIMS with a pulsed O_2 flow control at a low temperature of 300 °C without any substrate bias and without any interlayer, and antireflection SiO_2 layers of various thicknesses were deposited on the top of them using reactive mid-frequency (repetition frequency of 50 kHz) bipolar dual magnetron sputtering (oxide regime) with unbalanced magnetrons in a commonly used closed magnetic field configuration. The results show that the SiO_2 overlayers improved the luminous transmittance, T_{lum}, by up to 16% (from 40.3% to 56.3% for 30 nm thick VO_2) and the modulation of the solar transmittance, ΔT_{sol}, by up to 2.6% (from 7.7% to 10.3% for 88 nm thick VO_2). The results also quantify the tradeoff between (i) T_{lum} and its improvement by the SiO_2 overlayer (these quantities are higher for thinner VO_2) and (ii) ΔT_{sol} and its improvement by the SiO_2 overlayer (these quantities are higher for thicker VO_2). There is an excellent qualitative and a good quantitative agreement of the experimental data and the predictions based on the properties of pure VO_2 and SiO_2. The success of the industry-friendly preparation technique used can be also extrapolated to multilayer coatings which include more than two layers, and the qualitative conclusions concerning the design of the SiO_2 overlayer can be also extrapolated to antireflection layers of other materials.

4. The fourth aim was fulfilled in the parts F and G. The $V_{1-x}W_xO_2$ layers were deposited both directly on soda-lime glass substrates and on soda-lime glass substrates coated by ZrO_2 layers with a crystalline structure by reactive HiPIMS with a pulsed O_2 flow control combined with a simultaneous pulsed magnetron sputtering of W target. The substrates were at a floating potential. The substrate surface temperature was 330 °C. The magnetron with a V target was driven by a high-power pulsed dc power supply at the repetition frequency of 200 Hz and the deposition-averaged target power density close to 13 Wcm^{-2}. The magnetron with a W target was driven by a pulsed dc power supply at the repetition frequency of 5 kHz and the deposition-averaged target power density of 24 $mWcm^{-2}$ or 33 $mWcm^{-2}$. Under these conditions, the W contents in the $V_{1-x}W_xO_2$ metal sublattice of 1.2 ± 0.1 at. % (i.e., $x = 0.012$) and 1.8 ± 0.6 at. % (i.e., $x = 0.018$) resulted in the reduction of the transition temperature to 39 °C and 20 °C, respectively.

5. The fifth aim was fulfilled in the parts F and G. High-performance thermochromic $ZrO_2/V_{1-x}W_xO_2/ZrO_2$ coatings were prepared on soda-lime glass by pulsed reactive magnetron sputtering under highly industry-friendly deposition conditions: without any substrate bias and at a low substrate temperature of 330 °C. Reactive high-power impulse magnetron sputtering

with a pulsed O_2 flow control was used to prepare crystalline VO_2 layers of the correct stoichiometry. Simultaneous doping of VO_2 by W (resulting in a $V_{1-x}W_xO_2$ composition with $x = 0.018$) was performed using a pulsed dc reactive magnetron sputtering to reduce the semiconductor-to-metal transition temperature to 20 °C without concessions in terms of coating properties. A coating design utilizing a second-order interference on the ZrO_2 layers optimized the luminous transmittance, T_{lum}, up to 60% at the modulation of the solar transmittance, ΔT_{sol}, close to 6% for a $V_{0.982}W_{0.018}O_2$ thickness of 45 nm, and up to 50% at ΔT_{sol} above 10% for a $V_{0.982}W_{0.018}O_2$ thickness of 69 nm. Moreover, the crystalline structure of the bottom ZrO_2 layer further improved the VO_2 crystallinity and the process reproducibility, and the top ZrO_2 layer provided the mechanical and chemical (prevented contact with atmosphere) protection of the $V_{0.982}W_{0.018}O_2$ layers. Based on the comparison of our results obtained for the thermochromic VO_2-based coatings prepared on glass with the newest results in the literature, it can be stated that we achieved an excellent combination of the required characteristics: the lowest maximum substrate (glass) temperature during the preparation of the coatings (T_s)$_{max}$ = 330 °C, an appropriate transition temperature T_{tr} = 20 – 25 °C, and T_{lum} up to 60% at ΔT_{sol} close to 6% or T_{lum} up to 50% at ΔT_{sol} above 10%.

V Further publications of the candidate

1 Oral presentations at international conferences

[1] J. Houška, **D. Kolenatý**, T. Bárta, J. Rezek, J. Vlček
"Design of high-performance VO_2-based thermochromic coatings, and pathway for their low-temperature preparation" 4th E-MRS & MRS-J Bilateral Symposium, 14. – 19. 10. 2018, Chania, Greece

[2] J. Vlček, **D. Kolenatý,** J. Houška
"Controlled reactive HiPIMS – effective technique for low-temperature deposition of functional oxide films" 16th International Conference on Plasma Surface Engineering (PSE 2018), 17. – 21. 9. 2018, Garmisch-Partenkirchen, Germany

[3] **D. Kolenatý,** J. Vlček, J. Houška, T. Kozák
"Low-temperature (300°C) HiPIMS deposition of thermochromic VO_2 films with antireflection SiO_2 overlayers" 9th International Conference on Fundamentals and Industrial Applications of HiPIMS 2018, 25. – 28. 6. 2018, Sheffield, UK

[4] J. Vlček, **D. Kolenatý,** J. Houška
"Controlled reactive HiPIMS – effective technique for low-temperature deposition of functional oxide films" Conference on Coatings on Glass and Plastics (ICCG 12), 11. – 15. 6. 2018, Würzburg, Germany

[5] J. Vlček, **D. Kolenatý,** J. Houška
"Controlled reactive HiPIMS – effective technique for low-temperature deposition of functional oxide films" 9th Power Electronics for Plasma Engineering Conference, 14. – 16. 5. 2018, Freiburg, Germany

[6] **D. Kolenatý**, J. Vlček, T. Kozák, J. Houška, R. Čerstvý
"Controlled reactive HiPIMS – Effective technique for low-temperature (300 °C) synthesis of VO_2 films with semiconductor-to-metal transition" 16th International Conference on Reactive Sputter Deposition (RSD 2017), 4. – 6. 12. 2017, Plzeň, Czech Republic

[7] **D. Kolenatý**, J. Vlček, T. Kozák, J. Houška, R. Čerstvý
"Controlled reactive HiPIMS of thermochromic VO_2 films at a low deposition temperature (300 °C)" European Congress and Exhibition on Advanced Materials and Processes (EUROMAT2017), 17. – 22. 9. 2017, Thessaloniki, Greece

[8] **D. Kolenatý**, J. Vlček, T. Kozák, J. Houška, R. Čerstvý
"Controlled reactive HiPIMS – effective technique for low-temperature (300°C) synthesis of VO_2 films with semiconductor-to-metal transition" 44th International Conference on Metallurgical Coatings and Thin Films (ICMCTF 2017), 24. – 28. 4. 2017, San Diego, USA

[9] **D. Kolenatý**, J. Houška, J. Rezek, R. Čerstvý, J. Vlček
"Reactive High-Power Impulse Magnetron Sputtering of Thermochromic VO_2 Films at Low Deposition Temperatures" 4th International Workshop and the 3rd International Mini Workshop on Solution Plasma and Molecular Technologies (SPM-4 and Mini SPM-3), 7. – 11. 6. 2016, Plzeň, Czech Republic

[10] J. Houška, J. Rezek, **D. Kolenatý**, J. Vlček
"Characterization of thermochromic VO_2 thin films in a wide temperature range by spectroscopic ellipsometry" 7th International Conference on Spectroscopic Ellipsometry (ICSE-7), 6. – 10. 6. 2016, Berlin, Germany

2 Poster presentations at international conferences

[1] J. Houška, **D. Kolenatý**, J. Rezek, J. Vlček
"Pathway for a low-temperature (250 °C) deposition of thermochromic VO_2 without substrate bias voltage" 2017 MRS Fall Meeting, 26. – 30. 11. 2017, Boston, USA

[2] **D. Kolenatý**, J. Vlček, T. Kozák, J. Houška, R. Čerstvý
"Controlled reactive HiPIMS of thermochromic VO_2 films at a low deposition temperature (300 °C)" 15th International Conference on Reactive Sputter Deposition 2016 (RSD2016), 1. – 2. 12. 2016, Ghent, Belgium

[3] **D. Kolenatý**, J. Houška, J. Rezek, R. Čerstvý, J. Vlček
"Reactive High-Power Impulse Magnetron Sputtering of Thermochromic VO_2 Films at Low Deposition Temperatures" 15th International Conference on Plasma Surface Engineering (PSE 2016), 12. – 16. 9. 2016, Garmisch-Partenkirchen, Germany

[4] **D. Kolenatý**, J. Houška, J. Rezek, R. Čerstvý, J. Vlček
"Reactive high-power impulse magnetron sputtering of thermochromic VO_2 films at low substrate temperatures" 27th Symposium on Plasma Physics and Technology (SPPT 2016), 20. – 23. 6. 2016, Prague, Czech Republic

[5] **D. Kolenatý**, J. Houška, J.Rezek, R.Čerstvý, J. Vlček
"Reactive high-power impulse magnetron sputtering of thermochromic VO_2 films at low deposition temperatures" 4th Magnetron, Ion processing and Arc Technologies European Conference and 14th International Symposium on Reactive Sputter Deposition (MIATEC and RSD), 8. – 11. 12. 2015, Paris, France

Abstract

Vanadium dioxide is a technologically important thin-film material with a great application potential (e.g. smart windows) due to its reversible first-order semiconductor-to-metal transition. This Ph.D. thesis deals with preparation and characterization of thermochromic VO_2-based coatings. The thesis is divided into five chapters.

Chapter I is devoted to a general introduction and to the problem statement. In Chapter II, the aims are defined. Chapter III is the most extensive and is devoted to the results achieved. This chapter is divided into seven parts presented in a form of six papers in prestigious international journals (A–F) and one draft of the paper intended for submission into a prestigious international journal (G).

A. The paper deals with thermochromic VO_2 prepared by reactive high-power impulse magnetron sputtering and characterized by spectroscopic ellipsometry. We focus on the dispersion of optical constants in a wide temperature range and on the transmittance predicted using the optical constants. While the thermochromic behavior of VO_2 in itself has been reported previously (particularly above the room temperature, RT), in this paper we present (i) properties achieved at a low deposition temperature of 250 °C and without any substrate bias voltage (which dramatically increases the application potential of the coating) and (ii) changes of these properties not only above but also below RT (down to –30 °C). The properties include very low (for VO_2) extinction coefficient at RT (0.10 at 550 nm), low transition temperature of around 50 °C (compared to the frequently cited 68 °C) and high modulation of the predicted transmittance in the infrared region (e.g. 39% at –30 °C, 30% at RT and 3.4% above the transition temperature at 2000 nm for a 100 nm thick coating on glass). The results are important for the design of thermochromic coatings, and pathways for their preparation under industry-friendly conditions, for various technological applications.

B. Reactive high-power impulse magnetron sputtering (HiPIMS) with a pulsed O_2 flow control and to-substrate O_2 injection into a high-density plasma in front of the sputtered vanadium target was used for low-temperature (300 °C) deposition of VO_2 films with a pronounced semiconductor-to-metal transition onto conventional soda-lime glass substrates without any substrate bias voltage and without any interlayer. The depositions were performed using an unbalanced magnetron with a planar target of 50.8 mm diameter in argon-oxygen gas mixtures at the argon pressure of 1 Pa. The deposition-averaged target power density was close to 13 Wcm^{-2} at a fixed duty cycle of 1% with a peak target power density up to 5 $kWcm^{-2}$ during voltage pulses ranged from 40 µs to 100 µs. A high modulation of the transmittance at 2500 nm (between 51% and 8% at the film thickness of 88 nm) and the electrical resistivity (changed 350 times) at the transition temperature of 56 – 57 °C was achieved for the VO_2 films synthesized using 50 µs voltage pulses when the crystallization of the thermochromic VO_2(M1) phase was supported by the high-energy (up

to 50 eV relative to ground potential) ions. Principles of this effective low-temperature deposition technique with a high application potential are presented.

C. The paper deals with thermochromic VO_2 films deposited by reactive high-power impulse magnetron sputtering with a pulsed reactive gas flow control under exceptionally industry-friendly conditions: onto amorphous glass substrates without any interlayer, without any substrate bias voltage and at low temperatures (T_{dep}) down to 300 °C. We show that (and how) strongly thermochromic VO_2 films can be prepared even under these unfavorable conditions, and compare their properties with those achieved under more favorable but less industry-friendly conditions. We focus on the film structure studied by X-ray diffraction and Raman spectroscopy, electrical resistivity, and especially optical properties studied by spectroscopic ellipsometry and spectrophotometry. The properties achieved at T_{dep} = 300 °C include e.g. transition temperature (T_{tr}) below 60 °C, extinction coefficient at 550 nm of around 0.50, modulation of the extinction coefficient at 2000 nm between 0.35 (room temperature) and 3.77 (above T_{tr}) or modulation of the resistivity between 5.3×10^{-3} **Ω**m (room temperature) and 1.5×10^{-5} **Ω**m (above T_{tr}). The results are important for the design of pathways for the preparation of thermochromic coatings under industry-friendly conditions, and, in turn, significantly increase the application potential of these coatings.

D. The paper deals with thermochromic VO_2/SiO_2 coatings prepared by low-temperature pulsed reactive magnetron sputtering on conventional soda-lime glass substrates without any substrate bias and without any interlayer. Thermochromic VO_2 layers were deposited using reactive high-power impulse magnetron sputtering with a pulsed O_2 flow control at a substrate surface temperature of 300 °C. Antireflection SiO_2 layers were deposited using mid-frequency bipolar dual magnetron sputtering onto the top of VO_2 layers at a surface temperature below 35 °C in order to improve the optical and mechanical performance. We focus on the dependence of the luminous transmittance (T_{lum}) and the modulation of the solar transmittance (ΔT_{sol}) on the SiO_2 layer thickness. The measured dependencies are in good agreement with those predicted using properties of pure VO_2 layers measured by spectroscopic ellipsometry. Two different VO_2 layer thicknesses (30 and 88 nm) have been used to demonstrate the tradeoff between T_{lum} and ΔT_{sol}. We show an improvement due to the SiO_2 overlayer of up to 16% (from 40.3% to 56.3%) for T_{lum} measured at 25 °C and up to 2.6% (from 7.7% to 10.3%) for ΔT_{sol}. The results are important for the design and low-temperature fabrication of high-performance durable thermochromic VO_2-based coatings for smart window applications.

E. The ion-flux characteristics at a substrate position and the corresponding discharge characteristics were investigated during controlled low-temperature (300 °C) reactive HiPIMS depositions of thermochromic VO_2 films onto conventional soda-lime glass substrates without any substrate bias voltage and without any interlayer. It was shown that the phase composition of the films correlates with the $(V^+ + V^{2+})$ ion fraction and the $(V^+ + V^{2+}):(2O_2^+ + O^+)$ ion ratio in the total ion flux onto the substrate. Setting the amount of oxygen in the gas mixture allowed us to control not only the phase composition of the films but also their crystallinity. It was found that an appropriate composition of the total ion flux and high ion energies (up to 50 eV relative to ground potential) support the crystallization of the thermochromic phase in the VO_2 films. We achieved a high modulation of the transmittance at 2500 nm (between 51% and 8%) and of the electrical resistivity (changed 350 times) for a 88 nm thick VO_2 film.

F. The paper deals with VO_2-based thermochromic coatings prepared by reactive magnetron sputtering. We combine four ways how to improve the coating performance and to increase its application potential. First, reactive high-power impulse magnetron sputtering with a pulsed O_2 flow control allowed us to prepare crystalline VO_2 of the correct stoichiometry under highly industry-friendly deposition conditions: without any substrate bias at a low deposition temperature of 330 °C. Second, doping of VO_2 by W (leading to $V_{1-x}W_xO_2$, with $x = 0.012$ in this work) allowed us to shift the thermochromic transition temperature towards the room temperature (39 °C in this work), without concessions in terms of coating properties. Third, we employ ZrO_2 antireflection layers both below and above the thermochromic $V_{1-x}W_xO_2$ layer, and present an optimum design of the resulting $ZrO_2/V_{1-x}W_xO_2/ZrO_2$ coatings. Most importantly, we show that while utilizing a first-order interference on ZrO_2 leads one to a tradeoff between the luminous transmittance (T_{lum}) and the modulation of the solar transmittance (ΔT_{sol}), utilizing a second-order interference allows one to optimize both T_{lum} and ΔT_{sol} in parallel. Fourth, the crystalline structure of the bottom ZrO_2 layer further improves the VO_2 crystallinity and the process reproducibility. The optimum experimental values of ZrO_2 thickness are in agreement with those predicted during the coating design. The results are important for the design and low-temperature fabrication of high-performance durable thermochromic VO_2-based coatings for smart window applications.

G. The paper deals with thermochromic VO_2-based coatings prepared on soda-lime glass by pulsed reactive magnetron sputtering. We combine five ways how to improve the coating performance and to increase its application potential. First, reactive high-power impulse magnetron sputtering with a pulsed O_2 flow control was used to prepare crystalline VO_2 layers of the correct stoichiometry under highly industry-friendly deposition conditions: without any substrate bias at a low substrate temperature of 330 °C. Second, simultaneous doping of VO_2 by W (resulting in a $V_{1-x}W_xO_2$ composition with $x = 0.018$ in this work) was performed using a pulsed dc reactive magnetron sputtering to reduce the semiconductor-to-metal transition temperature to 20 °C

without concessions in terms of coating properties. Third, ZrO_2 antireflection layers both below and above the thermochromic $V_{0.982}W_{0.018}O_2$ layers were deposited at a low substrate temperature (< 100 °C) by a dual reactive mid-frequency ac magnetron sputtering. A coating design utilizing a second-order interference on the ZrO_2 layers was proposed to optimize both the luminous transmittance, T_{lum}, and the modulation of the solar transmittance, ΔT_{sol}. Fourth, the crystalline structure of the bottom ZrO_2 layer further improved the VO_2 crystallinity and the process reproducibility. Fifth, the top ZrO_2 layer provided the mechanical and chemical (prevented contact with atmosphere) protection of the $V_{0.982}W_{0.018}O_2$ layers. We give the basic characteristics of the applied deposition technique and the proposed three-layer coatings with T_{lum} up to 60% at ΔT_{sol} close to 6% for a $V_{0.982}W_{0.018}O_2$ thickness of 45 nm, and with T_{lum} up to 50% at ΔT_{sol} above 10% for a $V_{0.982}W_{0.018}O_2$ thickness of 69 nm.

Chapter IV is devoted to the conclusions of the Ph.D. thesis. In Chapter V, further publications of the candidate are given.

Resumé česky

Oxid vanadičitý je díky svému reverzibilnímu fázovému přechodu prvního řádu z polovodičového do kovového stavu technologicky důležitý tenkovrstvý materiál s velkým aplikačním potenciálem (např. chytrá okna). Tato disertační práce se zabývá přípravou a charakterizací termochromických povlaků na bázi VO_2. Práce je rozdělena do pěti kapitol.

Kapitola I je věnována obecnému úvodu a seznámení s problematikou. V kapitole II jsou definovány cíle disertační práce. Kapitola III je nejrozsáhlejší a obsahuje popis dosažených výsledků. Tato kapitola je rozdělena do sedmi částí ve formě šesti vědeckých článků publikovaných v prestižních mezinárodních časopisech (A–F) a jednoho konceptu vědeckého článku připravovaného pro publikaci v prestižním mezinárodním časopise (G).

A. Článek se zabývá termochromickým VO_2 připraveným pomocí reaktivního vysokovýkonového pulzního magnetronového naprašování a charakterizovaným pomocí spektroskopické elipsometrie. Zaměřujeme se na disperzi optických konstant v širokém rozsahu teplot a na z nich vypočítanou transmitanci. Zatímco termochromické chování VO_2 jako takové je známo (zejména nad pokojovou teplotou, RT), v tomto článku prezentujeme (i) optické vlastnosti dosažené při nízké depoziční teplotě 250 °C a bez předpětí na substrátu (což dramaticky zvyšuje aplikační potenciál těchto vrstev) a (ii) změny těchto vlastností nejen nad, ale také pod RT (až k –30 °C). Nejlepší vlastnosti zahrnují velmi nízký (pro VO_2) extinkční koeficient při pokojové teplotě (0,10 pro vlnovou délku 550 nm), nízkou teplotu přechodu kolem 50 °C (v porovnání s často citovanou hodnotou 68 °C) a vysokou modulaci vypočítané transmitance v infračerveném spektru (např. 39 % při –30 °C, 30 % při pokojové teplotě a 3,4 % nad přechodovou teplotou pro vlnovou délku 2000 nm a pro 100 nm tlustou vrstvu na skleněném substrátu). Výsledky jsou důležité pro design termochromických povlaků, a pro jejich přípravu za podmínek vhodných pro průmysl, pro nejrůznější technologické aplikace.

B. Reaktivní vysokovýkonové pulzní magnetronové naprašování (HiPIMS) s pulzním řízením toku O_2 a vstřikováním O_2 do vysokohustotního plazmatu před rozprašovaným vanadiovým terčem bylo použito pro nízkoteplotní (300 °C) depozici vrstev VO_2 s výrazným přechodem mezi polovodivým a kovovým stavem na konvenční sodnovápenaté sklo bez jakékoliv mezivrstvy. Pro depozici byl použit nevyvážený magnetron s planárním terčem o průměru 50,8 mm a plynová směs argonu a kyslíku při tlaku argonu 1 Pa. Průměrná hustota výkonu během depozice byla kolem 13 Wcm^{-2} při fixní střídě 1 % a výkonu během pulzů až 5 $kWcm^{-2}$. Délka pulzů se pohybovala mezi 40 µs a 100 µs. U vrstev VO_2 připravených pomocí 50µs pulzů, kdy byla krystalizace termochromické fáze VO_2(M1) podpořena vysokoenergiovými (až 50 eV vůči zemi) ionty, byla dosažena vysoká modulace transmitance pro vlnovou délku 2500 nm (mezi 51 % a 8 % pro tloušťku VO_2 vrstvy 88 nm) a elektrické rezistivity (změna 350×) při přechodové teplotě

56 – 57 °C. Prezentovány jsou také principy této efektivní nízkoteplotní depoziční techniky s vysokým aplikačním potenciálem.

C. Tématem článku jsou termochromické vrstvy VO_2 připravené vysokovýkonovým pulzním magnetronovým naprašováním s pulzním řízením napouštění reaktivního plynu, za podmínek výjimečně příznivých pro průmysl: na amorfní skleněné substráty bez jakékoliv mezivrstvy a při nízkých teplotách (T_{dep}) až k 300 °C. Ukazujeme, že (a jak) mohou být kvalitní termochromické vrstvy VO_2 připraveny dokonce i za těchto nepříznivých podmínek, a srovnáváme jejich vlastnosti s vlastnostmi vrstev připravených za podmínek příznivějších, ale méně vhodných pro průmysl. Zaměřujeme se na strukturu vrstev vyšetřovanou pomocí XRD a Ramanovy spektroskopie, elektrickou rezistivitu, a zejména optické vlastnosti změřené pomocí spektroskopické elipsometrie a spektrofotometrie. Vlastnosti dosažené při $T_{dep} = 300$ °C zahrnují například přechodovou teplotu (T_{tr}) pod 60 °C, extinkční koeficient pro vlnovou délku 550 nm přibližně 0,50, modulaci extinkčního koeficientu při 2000 nm mezi 0,35 (pokojová teplota) a 3,77 (nad T_{tr}) nebo modulaci rezistivity mezi $5{,}3\times10^{-3}$ Ωm (pokojová teplota) a $1{,}5\times10^{-5}$ Ωm (nad T_{tr}). Výsledky jsou důležité pro návrh přípravy termochromických povlaků za podmínek příznivých pro průmysl, a tím zvyšují aplikační potenciál těchto povlaků.

D. Tato práce se zabývá termochromickými VO_2/SiO_2 povlaky připravenými nízkoteplotním pulzním reaktivním magnetronovým naprašováním na konvenčních sodnovápenatých skleněných substrátech bez přivedeného předpětí na substrát a bez jakékoliv mezivrstvy. Termochromické VO_2 vrstvy byly připraveny použitím reaktivního vysokovýkonového pulzního magnetronového naprašování s pulzním řízením O_2 průtoku při povrchové teplotě substrátu 300 °C. Antireflexní SiO_2 vrstvy byly deponovány použitím mid-frequency bipolárního duálního magnetronového naprašování na VO_2 vrstvy při povrchové teplotě nižší než 35 °C za účelem zlepšení optických a mechanických vlastností. Zaměřujeme se na závislost integrální transmitance ve viditelné oblasti (T_{lum}) a modulace solární transmitance (ΔT_{sol}) na tloušťce SiO_2 vrstvy. Naměřené závislosti jsou v dobré shodě s předpovězenými pomocí naměřených vlastností čistých VO_2 vrstev spektroskopickou elipsometrií. Dvě různé tloušťky VO_2 vrstev (30 a 88 nm) byly vybrány ke znázornění kompromisu mezi T_{lum} and ΔT_{sol}. Ukazujeme zlepšení T_{lum} při teplotě 25 °C díky SiO_2 vrstvě až o 16 % (z 40,3 % na 56,3 %) a zlepšení T_{sol} díky SiO_2 vrstvě až o 2,6 % (z 7,7 % na 10,3 %). Výsledky jsou důležité pro návrh nízkoteplotní výroby vysoce funkčních durabilních vrstev na bázi VO_2 pro chytrá okna.

E. Charakteristiky iontových toků na pozici substrátu a odpovídající výbojové charakteristiky byly vyšetřovány pro řízené nízkoteplotní (300 °C) reaktivní HiPIMS depozice termochromických VO_2 vrstev na konvenčních sodnovápenatých skleněných substrátech bez přivedeného předpětí na substrát a bez jakékoliv mezivrstvy. Bylo ukázáno, že fázové složení vrstev korelovalo s iontovou frakcí ($V^+ + V^{2+}$) a s poměrem iontů ($V^+ + V^{2+}$):($2O_2^+ + O^+$) v celkovém iontovém toku na substrát. Nastavení množství kyslíku v plynné směsi umožnilo řídit nejen fázové složení vrstev, ale také jejich krystalinitu. Bylo zjištěno, že vhodné složení celkového iontového toku a vysoké energie iontů (až 50 eV vůči zemi) podpořily krystalizaci termochromické fáze ve VO_2 vrstvách. Dosáhli jsme vysoké modulace transmitance pro vlnovou délku 2500 nm (mezi 51 % a 8 %) a elektrické rezistivity (změna 350×) VO_2 vrstvev o tloušťce 88 nm.

F. Tato práce se zabývá termochromickými povlaky na bázi VO_2 připravenými reaktivním magnetronovým naprašováním. Kombinujeme čtyři způsoby, jak zlepšit funkčnost povlaků, a tak zvýšit jejich aplikační potenciál. Za prvé, reaktivní vysokovýkonové pulzní magnetronové naprašování s pulzním řízením toku O_2 nám umožnilo připravit krystalické VO_2 se správnou stechiometrií za podmínek výjimečně příznivých pro průmysl: bez předpětí na substrátu a při nízkých depozičních teplotách (T_{dep}) až k 300 °C. Za druhé, dopování VO_2 wolframem ($V_{1-x}W_xO_2$, v této práci $x = 0.012$) nám umožnilo posunout teplotu přechodu směrem k pokojové teplotě (v této práci 39 °C) bez zhoršení vlastností povlaku. Za třetí, byly použity ZrO_2 antireflexní vrstvy jak pod, tak nad termochromickou vrstvou $V_{1-x}W_xO_2$ a v práci je také prezentován optimální design výsledných $ZrO_2/V_{1-x}W_xO_2/ZrO_2$ povlaků. Především ukazujeme, že zatímco využití interference prvního řádu na vrstvě ZrO_2 vede ke kompromisu mezi integrální transmitancí ve viditelné oblasti (T_{lum}) a modulací solární transmitance (ΔT_{sol}), využití interference druhého řádu umožňuje optimalizovat jak T_{lum}, tak ΔT_{sol} současně. Za čtvrté, krystalická struktura spodní ZrO_2 vrstvy dále zlepšuje krystalinitu VO_2 vrstvy a reprodukovatelnost procesu. Optimální tloušťky ZrO_2 vrstev nalezené experimentem jsou v souladu s navrženými v rámci designu povlaku. Výsledky jsou důležité pro design a nízkoteplotní výrobu vysoce funkčních durabilních termochromických povlaků na bázi VO_2 pro aplikaci „chytrá okna“.

G. Tato práce se zabývá termochromickými povlaky na bázi VO_2 připravenými reaktivním magnetronovým naprašováním. Kombinujeme čtyři způsoby, jak zlepšit funkčnost povlaků, a tak zvýšit jejich aplikační potenciál. Za prvé, reaktivní vysokovýkonové pulzní magnetronové naprašování s pulzním řízením toku O_2 bylo použito pro přípravu krystalických VO_2 vrstev se správnou stechiometrií za podmínek výjimečně příznivých pro průmysl: bez předpětí na substrátu a při nízkých depozičních teplotách 300 °C. Za druhé, dopování VO_2 wolframem ($V_{1-x}W_xO_2$, v této práci $x = 0.018$) pomocí pulzního dc reaktivního magnetronového naprašování umožnilo snížit teplotu fázového přechodu z polovodičového do kovového stavu na 20 °C bez zhoršení vlastností povlaku. Za třetí, antireflexní ZrO_2 vrstvy jak pod, tak nad termochromickou vrstvou $V_{0.982}W_{0.018}O_2$ byly deponovány při nízkých teplotách substrátu (< 100 °C) pomocí duálního

reaktivního mid-frequency ac magnetronového naprašování. Byl navržen optimální design povlaku využívající interferenci druhého řádu ZrO_2 vrstev pro optimalizaci jak integrální transmitance ve viditelné oblasti, T_{lum}, tak modulace solární transmitance, ΔT_{sol}. Za čtvrté, krystalická struktura spodní ZrO_2 vrstvy dále zlepšuje krystalinitu VO_2 vrstvy a reprodukovatelnost procesu. Za páté, horní ZrO_2 vrstva poskytuje mechanickou a chemickou (zabránění kontaktu s atmosférou) ochranu $V_{0.982}W_{0.018}O_2$ vrstev. Ukazujeme základní charakteristiky aplikované depoziční techniky a navrhovaného třívrstvého povlaku s hodnotami T_{lum} až 60 % a ΔT_{sol} blízko 6 % pro povlaky s tloušťkou $V_{0.982}W_{0.018}O_2$ vrstvy 45 nm a s hodnotami T_{lum} až 50 % a ΔT_{sol} nad 10 % pro povlaky s tloušťkou $V_{0.982}W_{0.018}O_2$ vrstvy 69 nm.

Kapitola IV je věnována závěrům disertační práce. V kapitole V jsou uvedeny další publikace kandidáta.